THÈSE

Pour obtenir le grade de

DOCTEUR DE L'UNIVERSITÉ GRENOBLE ALPES

École doctorale : CSV- Chimie et Sciences du Vivant
Spécialité : Chimie Physique Moléculaire et Structurale
Unité de recherche : Institut LAUE LANGEVIN

# Comprendre comment la séparation de phase de deux protéines virales entraîne la formation de compartiments sans membrane

# Understanding how coacervation of two viral proteins drives the formation of membrane-less compartments

Présentée par :

**FELLA BOUCHAMA**

Direction de thèse :

| | |
|---|---|
| **Marc JAMIN**<br>Université Grenoble Alpes | Directeur de thèse |
| **Gabriel CUELLO**<br>ILL, | Co-directeur de thèse |
| **Sylvain PREVOST** | Co-encadrant de thèse |

Rapporteurs :

**Sonia LONGHI**
DIRECTEUR DE RECHERCHE, cnrs
**Elisar BARBAR**
PROFESSEUR, Oregan state university

Thèse soutenue publiquement le **29 mars 2023**, devant le jury composé de :

| | |
|---|---|
| **Marc JAMIN**<br>PROFESSEUR DES UNIVERSITES, Université Grenoble Alpes | Directeur de thèse |
| **Maité PATERNOSTRE**<br>DIRECTEUR DE RECHERCHE, CNRS | Examinatrice |
| **Judith PETERS**<br>PROFESSEUR DES UNIVERSITES, Université grenobles alpes | Examinatrice |
| **Martin WEIK**<br>DIRECTEUR DE RECHERCHE, CEA | Examinateur |
| **Sonia LONGHI**<br>DIRECTEUR DE RECHERCHE, cnrs | Rapporteure |
| **Elisar BARBAR**<br>PROFESSEUR, Oregan state university | Rapporteure |

Invités :

**Sylvain Prevost**
DOCTEUR EN SCIENCES, Institut Laue-Langevin

# *Remerciements :*

Je voudrais remercier tant de personnes, des personnes sans qui je ne serais pas ici aujourd'hui.

Une immense gratitude et un grand merci à **Marc Jamin et Sylvain Prévost** pour m'avoir appris et formé à faire tant de choses, des choses qui semblaient impossibles à accomplir il y’a seulement quelques mois.

Merci à **Caroline Mas** pour son temps, son aide précieuse dans la réalisation de nombreuses expériences, et pour avoir été là, quand j'avais besoin de soutien.

Merci à **Christine Ebel** et **Thomas Zemb** d'avoir trouvé le temps de m’enseigner et conseiller, de m'avoir forcé à me plonger dans des livres de physique que je ne croyais même pas pouvoir comprendre, et surtout de m'avoir fait comprendre la valeur d’un KRATKY plot.

Merci à **Giuseppe Zaccai** de m’avoir éclairé avec ses proverbes égyptiens, à **Jean-Marie Bourhis** pour m'avoir initié à la paillasse.

Merci à tous **mes collègues**, dont certains sont devenus plus que des collègues, mes expériences à l'ESRF n'auraient pas été aussi facile d’accès si **Dihia Moussaoui** n’avait pas été là.

Comment aurais-je pu arriver là aujourd’hui sans l'aide et la présence de **ma maman** et de **mon papa** qui m’ont sans cesse répété “L'effort fini toujours par payer", et de **Silia** qui envoyait des Tacos à l'institut quand j'avais faim, sur le scooter de **Badrou**.
Je n’oublie ma belle-famille, particulièrement mes beaux-parents qui m’ont tant encouragé.

A mes amies, celles qui m'ont écouté me plaindre pendant des heures, **Nari** au téléphone (Avec mon planning de ministre), **Lyna**, **Melissa**, **Ebru** et **Carla** à l'heure du déjeuner ou autour d’un brunch le samedi.

Pour finir, à celui sans qui mes journées et mon parcours n'auraient jamais pu être les mêmes, celui qui savait parfaitement comment me redonner le sourire après une dure journée, et celui qui m'a épousée en sachant dans quoi il s'embarquait : **Tim.**

" من طلب العلا سهر الليالي "

*Rachid Bouchama*

# Table of Contents

**Abbreviations** ........ **5**

**Abstract** ........ **7**

**Résumé** ........ **8**

**I. Introduction** ........ **9**

1. Foreword ........ 9
2. Viruses ........ 10
   - (a) Definition ........ 10
   - (b) Classification of viruses ........ 12
   - (c) Baltimore’s class V includes all negative-sense RNA viruses ........ 14
   - (d) Negative-sense RNA viruses of the order *Mononegavirales* ........ 15
   - (e) The rabies virus is a prototypic member of the Mononegavirales ........ 17
     - i. History ........ 17
     - ii. Pathogenesis ........ 17
     - iii. RABV genome ........ 19
     - iv. RABV virion ........ 19
     - v. RABV infectious cycle ........ 21
     - vi. Structure and functions of the RABV proteins involved in RNA synthesis ........ 22
3. Rabies virus Negri’s bodies (NBs) ........ 27
4. Negri bodies in other Mononegavirales ........ 29
5. Liquid-liquid phase separation (LLPS) ........ 30
   - (a) Phase diagrams ........ 31
   - (b) Forces that control LLPS ........ 32
   - (c) Lower critical solution temperature (LCST) phase diagram ........ 33
   - (d) Coacervation and LLPS ........ 34
   - (e) Intrinsically disordered proteins: the perfect molecular building blocks for inducing LLPS ........ 37
6. Neutrons and X-ray scattering studies of LLPS ........ 38
   - (a) Structural parameters determination from the scattering curve ........ 39
   - (b) Choosing X-ray or neutrons: ........ 44
   - (c) Examples of the use of neutrons and X-rays scattering for studying LLPS ........ 47

II. Objectives ....................................................................................50

III. Results............................................................................................51

1. Establishment of the system ....................................................51
   - (a) Protein production and quality control: ............................51
   - (b) RABV liquid-liquid phase separation enabling ................63
     - i. Phosphoprotein assembles into soluble complexes and induce LLPS ........63
     - ii. Complementary results........................................................91
2. Nucleoprotein and Phosphoprotein LLPS assays ........................99
   - (a) P and N interact but do not form LLPS in vitro ...................99
   - (b) Deuterated RABV P and effect of $D_2O$ in LLPS ....................102
   - (c) Preliminary data of P+N with SANS: ....................................102

IV. Discussion........................................................................................104

V. Materiel and methods ......................................................................108

1. Expression and purification of proteins.......................................108
2. Protein characterization methods:.................................................112
   - (a) Electrophoresis gel under denaturing conditions:..................112
   - (b) Absorbance spectroscopy .......................................................112
   - (c) Size exclusion chromatography (SEC)....................................113
   - (d) Size exclusion chromatography coupled with multi-angle laser light scattering and refractometry 114
   - (e) Mass spectrometry ..................................................................116
   - (f) Small angle X-RAY/neutrons scattering ..................................116
   - (g) Flow-induced dispersion analysis (FIDA) ...............................122
   - (h) Dynamic light scattering (DLS):..............................................124
   - (i) Analytic ultra-centrifugation (AUC): .......................................126

References: ..........................................................................................131

# Abbreviations

2D: 2 dimensional
3D: 3 dimensional
AA: amino acids
AIDS: Acquired immunodeficiency syndrome
ARNm: ARN messager
AUC: Analytical UltraCentrifugation
Cys: Cystein
$D_2O$: Deuterium Oxide (heavy water)
Da / kDa: Dalton / kiloDalton
DLS: dynamic light scattering
DNA: Deoxyribonucleic acid
DS: Double stranded
*E. coli*: *Escherichia coli*
EDTA: Ethylene Diamine Tetraacetic Acid
EM: Electron microscopy
ESRF: European Synchroton Radiation Facility
*FIDA:* Flow-induced dispersion analysis
G : Glycoprotein
HIV : Human immunodeficiency virus
$I_0$ : Intensity at 0 angle
IDP: Instrinsically disordred protein
IDR : Instrinsically disordered region
kb : kilobases
L: Polymerase
LCST: Low critical system temperature
LLPS: Liquid-liquid phase separation
M : Matrix protein
MALLS : Multi Angle Laser Light Scattering
MLOs: membraneless compartments
MM: Molecular mass
N : Nucleoprotein
$N^0$-$P^{68:}$ RNA-free unassembled nucleoprotein ($N^0$) complexed with a peptide of 68 AA derived from phosphoprotein.
NBs: Negri bodies
NCs: Nucleocapsids
nm : nanometer
NMR: Nuclear Magnetic Resonance
nt : nucleotide
P : phosphoprotein

PΔ91-131 : phosphoprotein without aa from 91 to 131
Ni-Nta : Nickel-Nitriloacetic acid
PAGE : PolyAcrylamide Gel Electrophoresis
PBS : Phosphate Buffered Saline
PCR: Polymerase Chain Reaction
PDB : Protein Data Bank
PEG : Polyethylene Glycol
P-FAM : Labeled phosphoprotein
PFL : Full length phosphoprotein
RABV: Rabies virus
$R_g$ : Radius of gyration
RNA : ribonucleic acid
RNP: Ribonucleoprotein particles
RSV : Respiratory Syncytial Virus
SANS: Small Angle Neutron Scattering
SAXS: Small Angle X-ray Scattering
SDS: Sodium Dodecyl Sulphate
SEC: Size Exclusion Chromatography
Sf21: Spodoptera frugiperda
SS : Single stranded
SV : Sedimentation velocity
TBE : Tris/Borate/EDTA
TEV : Tobacco Etch Virus protease
USAXS: Ultra small Angle X-ray Scattering
VSV: Vesicular stomatitis virus

# Abstract

Transcription and replication of the genome of non-segmented RNA viruses of negative polarity, including rabies virus (RABV), take place in membrane-less organelles that form in the cytoplasm of the host cell by liquid-liquid phase separation (called Negri bodies in the case of RABV)(Nikolic et al., 2017a). This physical process, usually induced by protein-protein or protein-nucleic acid interactions, results in the coexistence of two liquid phases, in the form of droplets of a protein-dense phase (molecular condensate) suspended in a dilute phase (Alberti, 2017). Recently, the discovery that many normal or pathological cell organelles are formed by a similar process of liquid-liquid phase separation has aroused great interest in biology (Nozawa et al., 2020)(Du & Chen, 2018). However, the underlying molecular mechanisms and forces involved in these processes remain poorly understood.

The objectives of my work were (1) to reconstitute in vitro, from purified recombinant proteins, the liquid-liquid phase separation process induced by the RABV phosphoprotein and nucleoprotein and (2) to study this system by different biophysical methods including neutron and small angle X-ray scattering to characterize the interaction mechanism and to characterize the dimensions and shape of the proteins in the condensate.

We produced, purified and characterized the RABV phosphoprotein and the soluble, monomeric form of the RABV nucleoprotein in complex with a phosphoprotein peptide. We have shown that RABV phosphoprotein alone was able to induce a reversible liquid-liquid phase separation at concentrations of the order of some mg.mL-1. We established a phase diagram as a function of temperature, salt concentration (NaCl) and protein concentration that is characterized by a lower critical solution temperature (LCST) and showed that the process is more complex than expected for a simple binary system. In dilute solution at high salt concentration (NaCl > 200 mM) and low temperature (< 10°C), the RABV phosphoprotein forms dimers, but at higher protein concentration or by varying the temperature or salt concentration, it forms soluble multimolecular assemblies that precede phase separation. We obtained small angle scattering profiles after centrifugation of the protein in the dilute solution and in the molecular condensate. Our data suggest that the liquid-liquid phase separation is induced by the self-coacervation of the phosphoprotein, involving intra- and inter-molecular interactions.

.

# Résumé

La transcription et la réplication du génome des virus à ARN nonsegmenté de polarité négative, dont le virus de la rage (RABV), se déroulent dans des organelles sans-membrane qui se forment dans le cytoplasme la cellule hôte par séparation de phase liquide liquide (appelés corps de Negri dans le cas du RABV)(Nikolic et al., 2017a), Ce processus physique, généralement induit par des interactions protéine-protéine ou protéine-acide nucléique, résulte dans la coexistence de deux phases liquides, sous la forme de gouttelettes d'une phase dense en protéine (condensat moléculaire) en suspension dans une phase diluée(Alberti, 2017). Récemment, la découverte que de nombreux organelles cellulaires normales ou pathologiques sont formées par un processus similaire de séparation de phase liquide-liquide a suscité un grand intérêt en biologie (Nozawa et al., 2020)(Du & Chen, 2018). Les mécanismes moléculaires sous-jacents et les forces impliquées dans ces processus restent néanmoins méconnus.

Les objectifs de mon travail étaient (1) de reconstituer *in vitro*, à partir de protéines recombinantes purifiées, le processus de séparation de phase liquide-liquide induit par la phosphoprotéine et la nucléoprotéine du RABV et (2) d'étudier ce système par différentes méthodes biophysiques dont la diffusion de neutrons et de rayons X aux petits angles pour caractériser le mécanisme d'interaction et pour caractériser les dimensions et la forme des protéines dans le condensat.

Nous avons produit, purifié et caractérisé la phosphoprotéine du RABV et la forme soluble, monomérique de la nucléoprotéine du RABV en complexe avec un peptide de la phosphoprotéine. Nous avons montré que la phosphoprotéine du RABV seule était capable à des concentration de l'ordre de quelque mg.mL$^{-1}$ d'induire une séparation de phase liquide-liquide réversible. Nous avons établi un diagramme de phase en fonction de la température, de la concentration de sel (NaCl) et de la concentration de protéine qui est caractérisé par une température de solution critique inférieur (LCST) et montré que le processus est plus complexe qu'attendu pour un simple système binaire. Dans une solution diluée à haute concentration de sel (NaCl > 200 mM) et basse température (< 10°C), la phosphoprotéine du RABV forme des dimères, mais à plus haute concentration de protéine ou en variant la température ou la concentration de sel, elle forme des assemblages multimoléculaires solubles qui précèdent la séparation de phase. Nous avons obtenu des profils de diffusion aux petits angles après centrifugation de la protéine dans la solution diluée et dans le condensat moléculaire. Nos données suggèrent que la séparation de phase liquide-liquide est induite par l'auto-coacervation de la phosphoprotéine, impliquant des interactions intra- et inter-moleculaires.

# I. Introduction

## 1. Foreword

The cell is the basic unit of life and each cell is surrounded by a lipidic membrane that acts as a selective barrier that allow concentrating some ions or molecules inside and excluding some others. The inside of biological cells is a highly heterogeneous environment that houses a large number of molecules of diverse nature and is the center of a large number of biochemical reactions. The normal functioning of these complex systems requires the coordination of thousands of reactions in time and space, and cellular organization appears to be an important component of this regulation.

Historically, the intracellular organization has been associated with compartments that are limited by lipidic membranes, referred as cellular organelles, such as the nucleus, the mitochondria, the chloroplasts, the endoplasmic reticulum… The lipidic membranes are impermeable to polar molecules and therefore physically limit the exchanges between the interior and the exterior. The membranes are the support of proteins that control this transport and determine the composition of the compartments by controlling the partitioning of ions or molecules between the interior and the exterior. The presence of these membrane-bound compartments is seen as a hallmark of eukaryotic cells (Ohki, 1991)(Redondo-Morata et al., 2020)(Leabu, 2006).

In addition, over the years, cell biology uncovered that intracellular organization also occurs through the self-organization of biomolecular condensates, also known as membrane-less organelles (MLOs)(Rabouille, 2019), of specific composition such as the nucleoles that are the sites of ribosome biogenesis, the P bodies that store the degraded RNAs in the cell, the centrosomes that organize the microtubule network in the cell or the Cajal bodies and the stress granules (Biamonti & Vourc'h, 2010; Riggs et al., 2020). In addition, some abnormal condensates have been associated with different diseases including neurodegenerative diseases (Huntington's disease, amyotrophic lateral sclerosis,…)(Ryan & Fawzi, 2019), several types of cancer (Boija et al., 2021) and infectious diseases (rabies virus).

Recently, it has been shown that some of these normal and pathological MLOs are liquid compartments and that they form by liquid-liquid phase separation or liquid-solid phase separation (Ranganathan & Shakhnovich, 2019). The driving forces for their formation are multivalent weak interactions between macromolecules that lead to the separation of the condensate from the solution. The liquid nature of these compartments allows direct exchanges of small and large compounds between the interior and the exterior. These are controlled by diffusion, which is by the existence of concentration gradients (or more accurately of chemical potential gradients). There are exceptions for the compounds that control the phase separation, for which the chemical potential is equal inside and outside the MLO.

Of particular interest for our research project, compartmentalization is also important for viruses and different viruses use different ways to isolate their replication center within the infected cells. For example the endoplasmic reticulum (ER) (Inoue & Tsai, 2013) is used by some viruses, and both hepatitis C virus (HCV) and influenza virus modify the ER into a membranous organelles (de Castro Martin et al., 2017) . Some viruses, such as the HIV (Neil et al., 2006) and the adenovirus, create their own viral assembly compartment, by hijacking a piece of membrane from the host cell plasma membrane, and some viruses create MLOs. A typical example is that of rabies virus, which induces the formation of cytoplasmic inclusions in the infected cells, known as NEGRI’s bodies(Nikolic et al., 2019), where transcription and replication and encapsidation of the viral genome take place. Interestingly, similar inclusions have also been observed in cells infected by other related viruses (Zhou et al., 2019)(Rincheval et al., 2017).

In the initial part of my thesis report, I will first introduce viruses and describe in more details those belonging to the order *Mononegavirales* and in particular the rabies virus, which is the main topic of my project. Then, I will briefly describe the phenomenon of liquid-liquid phase separation and summarize the state of knowledge about the formation of virally induced liquid compartments in rabies virus infected cells and in cells infected by related viruses. Finally, I will give an overview of the use of SAXS and SANS for characterizing this type of system.

## 2. Viruses

### (a) Definition

Viruses are molecular parasites or symbiotes that co-evolved with and infect nearly all forms of cellular life: bacteria, archaea and eukaryotes. In humans, they are able to infect cells in various organs and tissues, and can cause a wide range of illnesses, from the common cold and flu to more serious diseases such as AIDS, measles, and COVID-19. Antiviral drugs and vaccines are used to combat viral infections, but vaccines are still lacking against many medically relevant viruses and few antivirals have been developed into drugs approved for human use.

Viruses have genetic material, which can be of different nature, but they can replicate and express this genomic material only inside a suitable host cell. Their infectious replication cycle thus always includes an intracellular phase, involving (1) the introduction by one way or another of their genetic material into a suitable host cell, (2) the hijacking of the resources and molecular machines of this cell, in particular the ribosomes, leading to the transformation of the original cell into a “viral factory” that generates viral proteins and replicates the viral genome, and (3) the assembly of viral particles and their release from the cell (Pellett et al., 2014).

The replication cycle also involves (4) an extracellular phase, which allows the propagation of the virus to other cells or other individuals. The phase of viral propagation can take different routes depending on the virus. At that stage, the virus takes the form of a viral particle or virion, i.e. genetic material (DNA or RNA) enclosed in a protein capsid and in some cases in a lipidic envelop. The viral particle thus corresponds to the form of the virus, which according to the famous quote of Peter Medawar, is: “A piece of bad news wrapped up in a protein coat”.

The origin of viruses remains a controversial issue. Three different scenarios have been considered and revisited over the years. The "primitive viral world" hypothesis posits that viruses directly descent from the first replicons that appeared in the precellular stages of life. According to the hypothesis of 'reverting viral origin’, viruses are the products of progenitor cell degeneration after they have lost their autonomy and have developed obligatory intracellular parasitism. Finally, according to the "escape gene" scenario, viruses evolve independently multiple times in different cellular organisms from host genes that acquired (quasi) autonomous replication and infectivity capabilities (Koonin et al., 2006).

The symbiotic interactions between viruses and host cells and organisms are of diverse nature, leading to different types of symbiosis ranging from symbiogenic, to commensal and antagonistic (Roossinck & Bazán, 2017). Cellular organisms have evolved multiple systems to protect themselves against microbial infections and in particular against viral infections. Viral infections can be asymptomatic or cause various symptoms and even death. The advert effects of infections are sometimes caused by the direct consequences of the viral infection (malfunctioning or death of cells) but very often result of the normal (e.g. fever,…) or abnormal (e.g. cytokine storm) reactions of our own defenses systems. Viruses excel in the art of hijacking cellular machines, in particular cellular ribosomes, and of evading and counteracting immune responses (Thaker et al., 2019).

## (b) Classification of viruses

All current cellular forms of life use double strand DNA as their genetic material, but viruses use a great diversity of genetic materials. Their genome can be made of DNA or RNA, and can be single-stranded or double-stranded. Their genome can be linear or circular, and in some cases, the genome is segmented, meaning that it is divided into multiple segments.

This diversity of material is associated with a great diversity of mechanisms used for the replication and expression of the genetic information. Thus, some viruses encode their own polymerase, while some others hijack cellular polymerases. The genome of some viruses can be directly translated by the cellular ribosomes (positive-sense RNA viruses such as hepatitis C virus or SARS-CoV2), while that of others must first be transcribed (negative-sense RNA viruses such as influenza virus or rabies virus). The convergence of all mechanisms is the need to generate, at some point in their infectious cycle, one or more messenger RNAs that can be adopted for translation by cellular ribosomes. Other features of viruses are their large number of progeny and their high mutation or variation rate, which explain their capacity to rapidly adapt to different environments, to evade the host defense systems of their host and to develop resistance against antiviral drugs.

Several classification systems have been proposed over the years, and in 1971, David BALTIMORE proposed to classify the viruses according to both the nature of their material and the mechanisms used for their replication and expression (**Figure, 1**)(Baltimore, 1971)(Koonin et al., 2021). According to this classification, viruses are divided into seven groups:

1. Group I: dsDNA viruses: double-stranded DNA viruses, such as herpesviruses and adenoviruses
2. Group II: ssDNA viruses: single-stranded DNA viruses, such as parvoviruses
3. Group III: dsRNA viruses: double-stranded RNA viruses, such as reoviruses
4. Group IV: (+)ssRNA viruses: positive-sense single-stranded RNA viruses, such as coronaviruses and influenza viruses
5. Group V: (-)ssRNA viruses: negative-sense single-stranded RNA viruses, such as paramyxoviruses and rhabdoviruses
6. Group VI: ssRNA-RT viruses: single-stranded RNA viruses that use reverse transcriptase, such as retroviruses (HIV)
7. Group VII: dsDNA-RT viruses: double-stranded DNA viruses that use reverse transcriptase, such as hepadnaviruses

In this work, we were interested in negative-sense RNA viruses belonging to BALTIMORE’s class V.

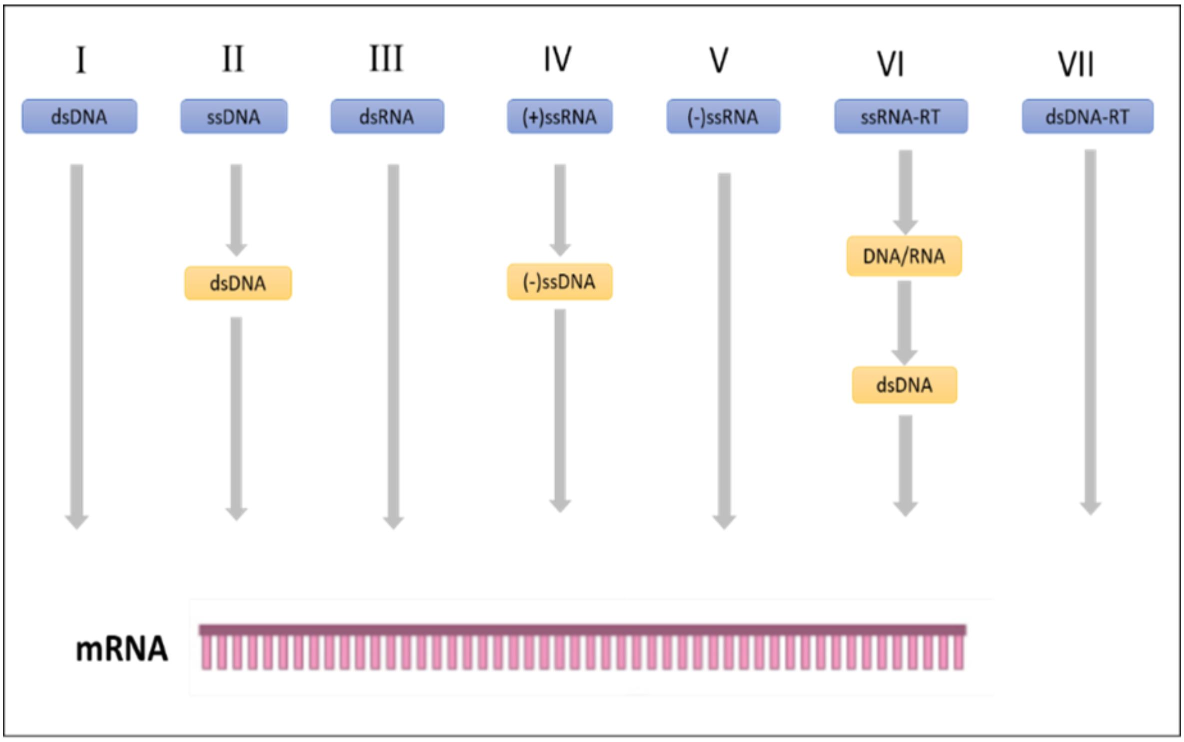

*Figure 1 Baltimore classification of viruses*

## (c) Baltimore's class V includes all negative-sense RNA viruses

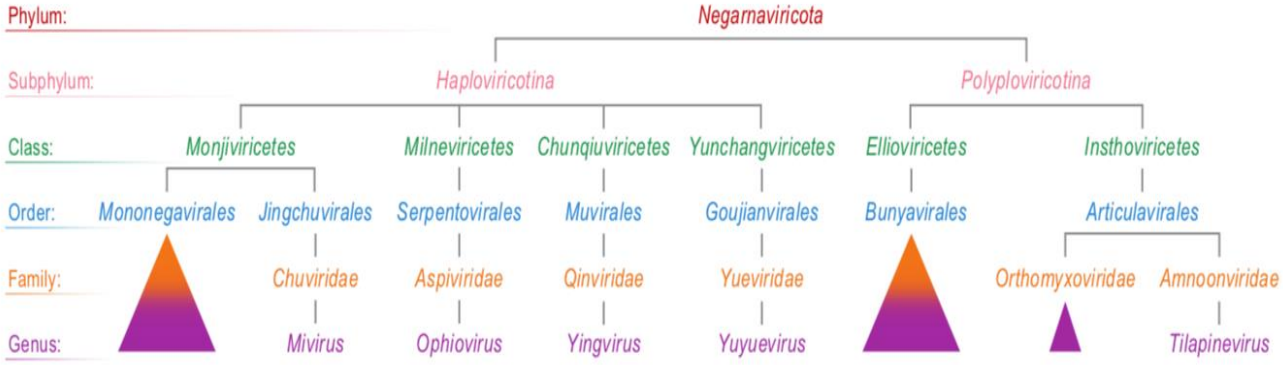

*Figure 2 Negative sense RNA viruses classification.* (Khun, 2019)

Historically, viruses were discovered mainly as the etiological agents of diseases affecting humans, domestic animals, livestock and crop plants. Viruses belonging to BALTIMORE's class V include the etiological agents of different human diseases, such as measles and mumps viruses, which cause children diseases, the respiratory syncytial virus, the metapneumovirus and various parainfluenza viruses, which cause mild to severe respiratory diseases. They also include different zoonotic viruses that cause deadly epidemics, such as rabies virus, Ebola virus and Nipah virus and various viruses infecting domestic animals and livestock, such as the Newcastle disease virus, the canine distemper virus or the vesicular stomatitis virus.

This way of discovering viruses had only allowed uncovering a limited part of the virosphere, but the accessibility to new generation sequencing methods from 2005 opened the door to metagenomics (Greninger, 2018) studies of clinical or environmental samples. These studies led to the discovery of many more viruses, even if most of them are only known from the sequence of genome fragments and have not been isolated. Until recently, most the taxonomy of negative-sense RNA viruses was rather limited, and all known viruses belonged to two orders (*Mononegavirales* and B*unyavirales*) and to a few independent families (*Orthomyxoviridae*). The explosion of sequence information from metagenomics studies led to the establishment of a complete taxonomic organization, and today, all negative-sense RNA viruses are classified in the phylum *Negarnaviricota* (Kuhn et al., 2020) (**Figure, 2**). The latter is divided in two subphyla: viruses with a non-segmented genome constitute the subphylum *Haploviricotina* and those with segmented genomes constitute the subphylum *Polyploviricotina*.

Overalll the phylum *Negarnaviricota* contains six classes, and multiple orders and families but the orders *Mononegavirales* for non-segmented viruses (e.g rabies virus), and *Bunyavirales* for segmented viruses (e.g Hantavirus), remain those with the largest number of known and studied members.

Negative sense RNA viruses have a helical nucleocapsids (NCs) and an envelope. They can take various shapes and sizes. Unlike positive-sense RNA viruses, whose genome can be directly translated by host cell ribosomes, negative-sense RNA viruses require the presence in the virion of a viral enzyme called RNA-dependent RNA polymerase (RdRp) to transcribe the viral RNA into positive-sense RNA (te Velthuis et al., 2021), and to replicate genome.

### (d) **Negative-sense RNA viruses of the order *Mononegavirales***

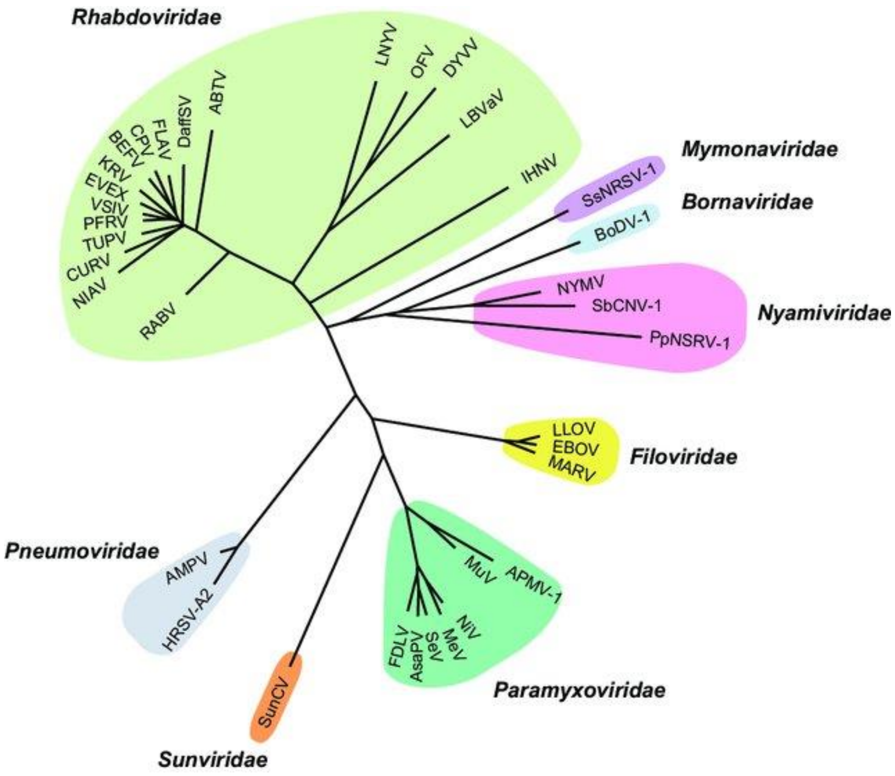

*Figure 3 Mononegavirales classification, adapted from Hector C Aguilar*

Numerous enveloped viruses with a non-segmented negative-sense RNA genome belong to the order *Mononegavirales* and are classified in different families (Amarasinghe et al., 2019) (**Figure, 3**), in particular the *Filoviridae* (Ebola virus), *Paramyxoviridae* (measles, virus, Nipah virus), *Pneumoviridae* (respiratory syncytial virus) and *Rhabdoviridae* (Rabies virus). This classification of different families in the same order relies on a number of shared features, including the nature of the genome (negative-sense RNA), the presence of a set of five common genes organized in the same order along the genomic RNA and that encode proteins sharing similar architectures and carrying out similar functions in the viral cycle, the presence of an RNA-dependent RNA polymerase (RdRp) (Liang, 2020) in the virion, the presence of helical NCs both in the virion and in infected cells.

Various members of the order *Mononegavirales* are known to cause human or animal diseases, including the highly contagious human measles virus, which triggers severe immunodepression and affects airways of children, the Ebola virus, which causes hemorrhagic fever, killing more than 14,000 people in West Africa in 2015, or the deadly rabies virus, which has a death rate of 100%. Efficient vaccines are available against some of them, but unfortunately, are still lacking against many medically relevant ones, and no specific and efficient antiviral drug has been approved for human use.

In the world of viruses, zoonotic viruses (HEENEY, 2006) that emerge from wildlife and domesticated animals are serious threats to human health and economy (Weber et al., 2015). Over the past century, humanity has witnessed the emergence of infections that have resulted in varying numbers of human fatalities. Influenza viruses that originate from birds account for an important proportion of these outbreaks, but recently many new zoonotic viruses that originate in bats, such as Ebola virus, Marburg virus, Hendra virus and Nipah virus have caused outbreaks with high mortality rates (**Figure, 4**).

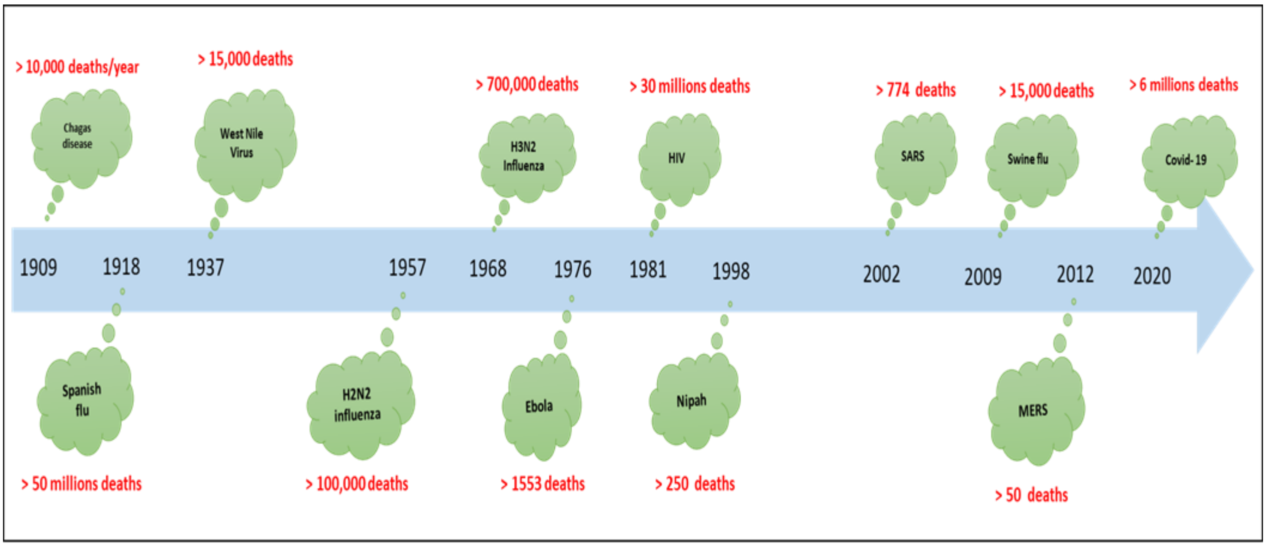

Figure 4. *Emergence of zoonoses over the past century.* Numbers from Nature reviews l Immunology

## (e) The rabies virus is a prototypic member of the Mononegavirales

### i. History

Rabies is terrible and deadly disease in humans that is known since around 2000 BC. Its infectious origin was proposed at the beginning of the 19th century (Georg Gottfried Zinke, 1804) (Pearce, 2002) and Paul REMLINGER demonstrated that the disease was caused by a filtrable virus. Pierre-Victor GALTIER initiated the development of a vaccine against rabies virus and suggested that because of the length of the incubation period of this disease, a vaccine could be used as a curative treatment. Louis PASTEUR continued the development of the vaccine, and in July 1885, he succeeded in immunizing a young boy named Joseph MEISTER, who had been bitten several times by a rabid dog, by repeatedly inoculating him with a preparation of attenuated virus from rabbit spinal cord.

The rabies virus (RABV) is a nonsegmented negative-sense RNA virus that is classified in the order *Mononegavirales*, in the family *Rhabdoviridae* and in the genus Lyssavirus. It is named after the characteristic rod- or bullet-shaped virion observed by electron microscopy (from the Greek "rhabdos" meaning a stick) and the genus from *Lyssa*, the personification of madness in Greek mythology.

### ii. Pathogenesis

RABV is a neurotropic virus, which causes fatal encephalomyelitis. Despite the existence of an efficient vaccine for more than a century, RABV continues to kill more than 55,000 people every year, essentially in rural area in Asia and Africa according to WHO. This number of deaths is likely underestimated and is explained by the lack of the implementation of control measures for young children in these countries and by the difficulties to access to post-exposure prophylaxis because of economical cost and by the poor stability of the vaccine (Davis et al., 2015a).

The natural reservoirs of RABV are insectivorous bats (*Microchiroptera*), wild *carnivorans* (foxes, raccoons,…) and domesticated dogs. Most human RABV cases result from dog bites, which expose muscle tissue to the animal saliva containing RABV particles. In the current model of RABV neuro-invasion, the virus starts to replicate in the wounded muscle and enters the central nervous system by budding from muscle cells into the synaptic space of neuromuscular junctions. The virus travels through the nerves to the spinal cord and the brain (retrograde transport) (**Figure, 5A**). This process can last approximately 3 to 12 weeks. When it reaches the brain, the virus multiplies rapidly. Then, clinical signs of the disease appear and death occurs in about 7 days after terrible sufferings. In the last stages of the infection, the virus moves then by an anteretrograde transport to the salivary glands. In combination with the observed modification of behavior (increased aggressivity), the shedding of viral particles in these glands provides a gateway to escape from the body and invade new hosts. (Dietzschold et al., 2008).

The clinical signs of rabies develop in three stages.

- Prodromal stage: This stage can last for several days and is characterized by mild, unspecific symptoms such as fever, headache, muscle weakness, and malaise.
- Excitative stage: During this stage, the infected person experiences symptoms such as anxiety, agitation, confusion, and delirium. They may also experience hydrophobia ("fear of water") resulting from spasms in the trachea.
- Paralytic stage: In this stage, the virus interferes with muscles, causing paralysis and leading to respiratory failure. The infected person may also experience drooling and difficulty swallowing.

Other symptoms of rabies include seizures, muscle spasms, and hallucinations.

If infected individuals are vaccinated soon after infection and eventually received post-infection treatments, they will not develop symptoms and will be safe. If symptoms appear, indicating that the virus reached the brain, then the issue is always fatal (Dietzschold et al., n.d.).

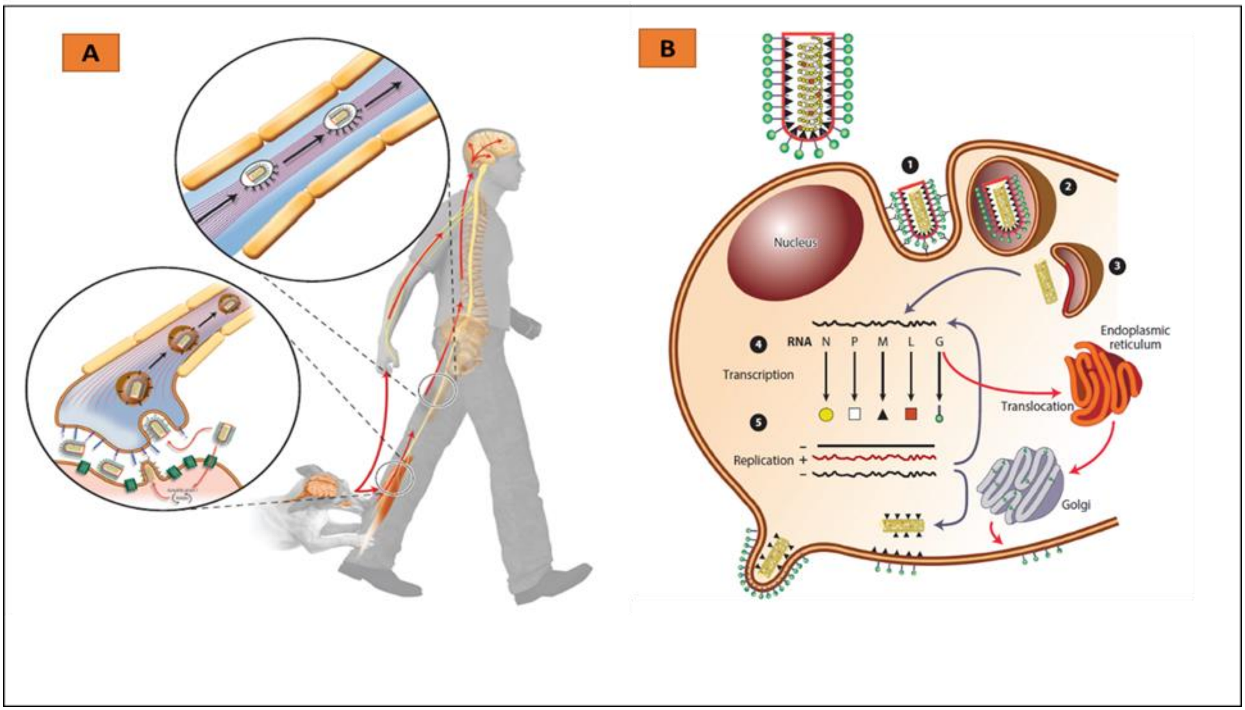

*Figure 5* ***A**: Rabies virus infection through the host* ***B**: Viral infectious cycle of RABV* (Davis et al., 2015b)

### iii. RABV genome

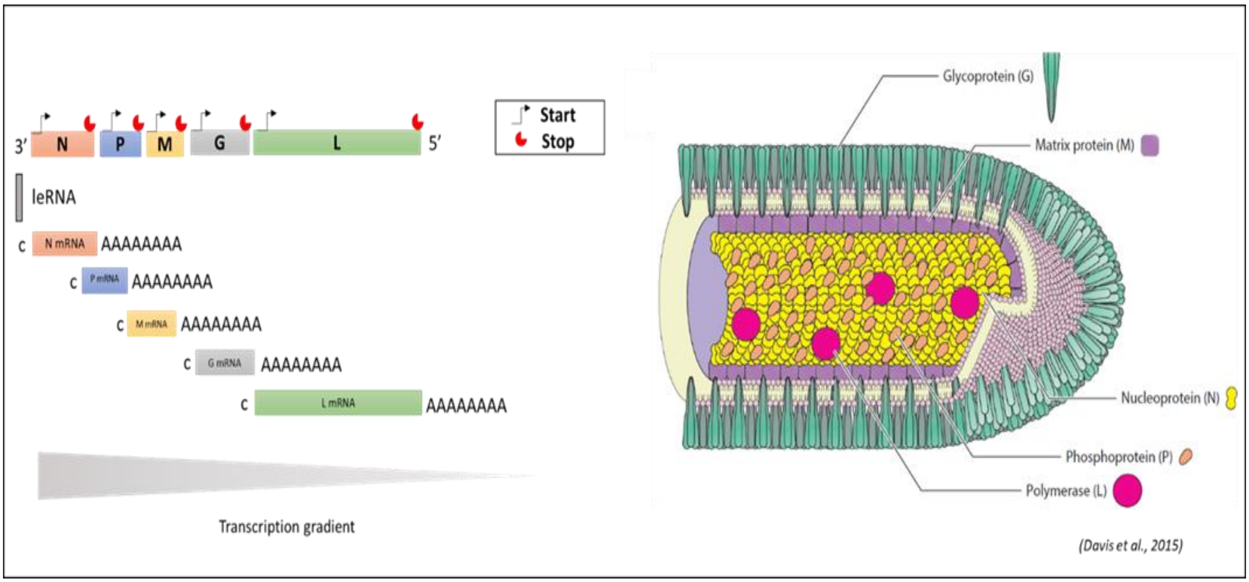

*Figure 6. Viral protein and genome expression of rabies virus* (Davis et al., 2015b)

The genome of the *Rhabdoviridae* is of 9–18kb in length and comprises up to ten genes flanked by untranslated leader (le) trailer (tr) RNA regions (Hidaka et al., 2018). The RABV genome of the CVS strain is composed of 11,927 nt and contains only five genes that are common to all members of the order *Mononegavirales*. They encode successively from the 3′ terminus, the nucleoprotein (N), the phosphoprotein (P), the matrix protein (M), the glycoprotein (G) and the large subunit of the RNA-dependent RNA polymerase (L) (**Figure, 6**). The G and M proteins are involved in the penetration of the virus in its host cell and in the assembly and budding of new viral particles. The ribonucleoprotein complex containing the genomic RNA together with the N, P and L proteins, constitutes the active machinery that carries out both transcription and replication of the genome.

### iv. RABV virion

Rhabdovirus virions, like other negative-stranded RNA viruses, are composed of a highly stable and organized complex of genomic RNA and nucleoprotein, typically called NCs (Iseni et al., 1998), contained in a lipid envelope derived from the host cell membrane. They are known for their distinctive bullet-shaped or rod-shaped appearance when viewed under an electron microscope.

The density map of the vesicular stomatitis virus (VSV) virion obtained from cryo-electron microscopy recontructions shows different concentric layers (Ge et al., 2010). The internal layer is a combination of RNA and N to form a (NC ribbon. The ribbon is then shaped into a compact ring, which then folds into larger rings that finally form the helical trunk (Brown et al., 2010) (**Figure, 7**). The intermediate layer formed by M subunits, is attached to the exterior of the NC, and provide a triangularly packed base for attaching G trimers and envelope membrane. The outer layer is the lipid envelope (Brown et al., 2010), which surrounds the matrix and includes the G protein.

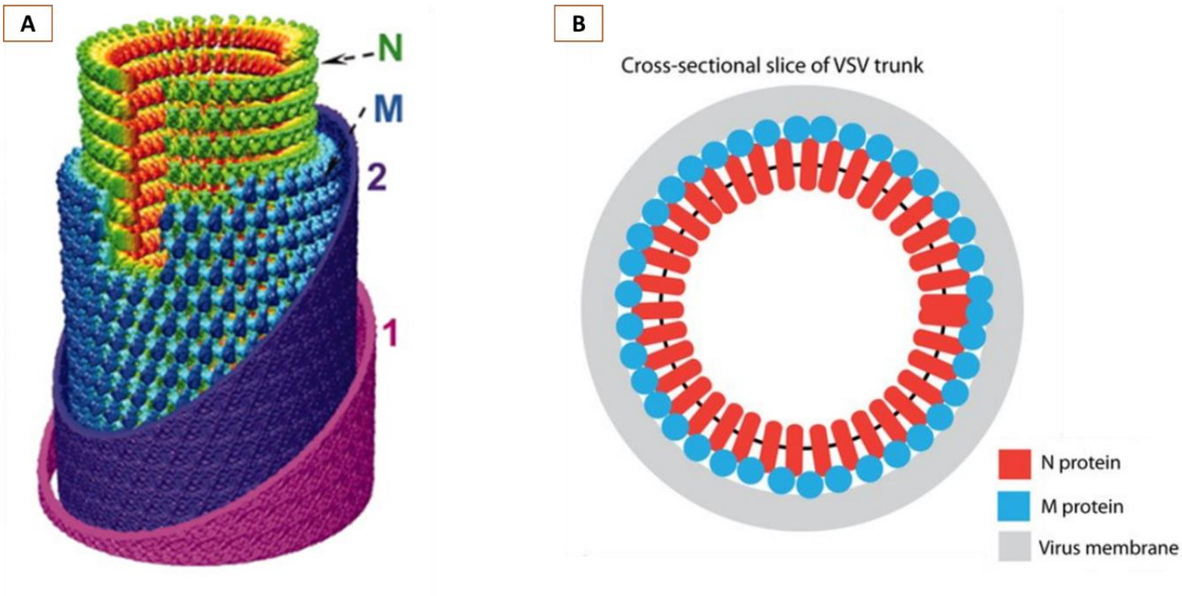

Figure 7. **(A)** Representative 2D averages of conical tip, trunk, and base of VSV and a montage model of the tip and the cryo-EM map of the trunk. N is green, M is blue, and the inner (2) and outer (1) leaflets of the membrane are purple and pink, respectively (Ge et al., 2010). **(B)** Representation of the external view of the N (red) and M (blue) helices as they are found in the trunk region of the mature virion (Brown et al., 2010).

## v. RABV infectious cycle

RABV replicates exclusively in the cytoplasm of its host cells (Follett et al., 1974). Its infectious cycle includes the stages of cell entry (cell adhesion, endocytosis and membrane fusion), biosynthesis (transcription, translation and replication), and exit (virion assembly and budding) (**Figure, 5B**).

The process begins with the virus attaching to the cell plasma membrane through interaction of the G protein with host cellular receptors, leading to the endocytosis of the virion. The lower pH inside the endosome induces the conformational change of the G protein and the fusion between the viral envelope with the endosomal membrane (Gaudin, et al., 1999) This leads to the release of the NCs together with the polymerase complex (L and P proteins) into the host cell cytoplasm.

The biosynthesis phase that follows can be divided into different successive steps (Albertini et al., 2011) (1) The viral polymerase complex, made up of L and P proteins, initiates the primary transcription of the genome into monocistronic messenger RNAs for the five viral proteins. The polymerase must always initiate at the 3' end of the genome and proceeds by a START/STOP mechanism, in which the polymerase pauses at the end of each gene and either dissociates from the template or scans to find the next GENE START signal. Because of this, viral mRNAs follow a gradient of production going from 3' to 5'. The viral polymerase adds and methylates a cap at the 5' end and a polyA tail at the 3' end of each mRNA. These viral mRNAs are then translated by the host cell ribosomes into viral proteins. (2) The accumulation of new viral proteins in the cell, in particular of the nucleoprotein in complex with its phosphoprotein chaperone ($N^0$-P complex), triggers the viral replication. In this step, the polymerase synthesizes full-length positive copies of the genome, named antigenomes, which are concomitantly encapsidated by multiple copies of the nucleoprotein. This generates NCs containing the antigenome (Ruigrok et al., 2011), which can then be used as template by the polymerase to produce new negative-sense copies of the genome. (3) The new genomic copies can then also be used for transcription and a step a secondary transcription starts, which leads to an amplification of the production of viral material in the cell. Along these processes, the G protein is directed to the endoplasmic reticulum and Golgi apparatus where it becomes glycosylated by cellular enzymes and is finally delivered to the plasma membrane.

The last stage of the intracellular part of the cycle consists in the assembly of the virions at the plasma membrane. The sequence of the M protein contains a motif of interaction with the host cell machinery involved in multi-vesicular body (MVB) formation (ESCRT machinery) and the M protein mediates the release of viral particles by redirecting this machinery to the cytoplasmic membrane (Harty et al., 1999; Irie et al., 2004). The M protein spontaneously associates with the cytoplasmic membrane, where it recruits newly assembled ribonucleoprotein complexes (Solon et al., 2005) and interacts with

G proteins that have accumulated in patches (rafts) in the cell plasma membrane. The ribonucleoprotein complexes are made of a NC that adopts a bullet shape, and multiple copies of the polymerase and phosphoprotein. The last step is the budding of the viral particle that leaves the cell with a piece of membrane encompassing the G proteins.

### vi. Structure and functions of the RABV proteins involved in RNA synthesis

The **Nucleoprotein (N)** is the most abundant protein in the virus particle. It has a high affinity for RNA and its primary function is to encapsidate the genomic and antigenomic RNA to form polymeric NCs.

The role of this encapsidation is difficult to assess, but in *in vitro* assays, the nucleoprotein protects the viral RNA against nucleases (RNases), and partially hides the RNA from chemical reagents (Baudin et al., 1994). We can thus hypothesize that the encapsidation protects the RNA against cellular enzymes but also against intracellular receptors of the host immune responses. In particular, encapsidation prevents the formation of double-stranded RNA, which are known to be important pathogen associated molecular patterns (PAMPs). In addition, encapsidation prevents the formation of secondary structures, which could hamper the motions of the polymerase or could facilitate the production of defective copies (defective interfering (DI) particles).

When expressed in insect cells or bacteria, the RABV N encapsidates non-specific RNAs, forming long helical NCs structures (**Figure, 8**), as well as circular structures called rings with a variable number of subunits. These recombinant forms of NCs have been very useful for structural studies, and a crystal structure of a circular N-RNA complex with 11 N subunits has been solved (Albertini et al., 2006).

The structure of N protein is composed of two globular domains that are connected by a hinge, thus creating a groove for binding the RNA. It also includes two subdomains, an N-terminal extension called the $N_{NT\text{-}ARM}$ and an internal loop in the C-terminal domain known as the $N_{CT\text{-}ARM}$. These subdomains dock to neighboring subunits in the polymeric form and help to stabilize the assembled NCs.

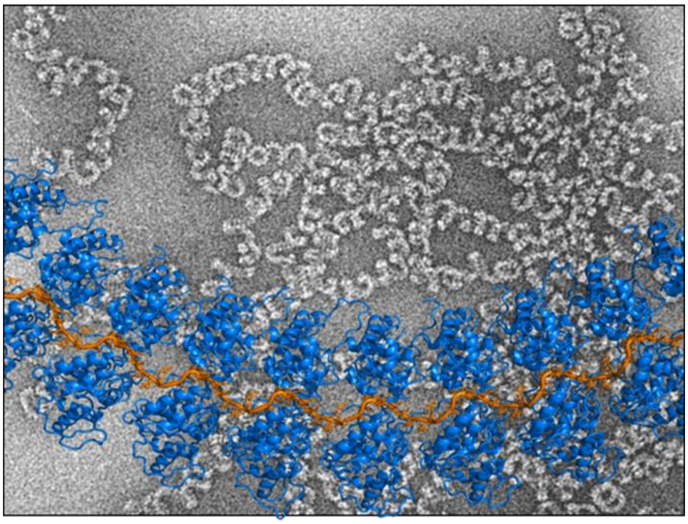

*Figure, 8. Electron microscopy picture of rabies virus NCs prepared in negative staining, and below: the structure of RNA (orange) encapsidated by nucleoproteins (blue). Photo credit : Rob Ruigrok*

**The phosphoprotein (P) is** a multifunctional protein, which performs multiple functions in the replication of the virus (**Figure, 9**): (1) it acts as a chaperon of the nucleoprotein, in order to prevent the latter to assemble and bind cellular RNAs. This function is performed by a small linear motif (SLiM) at the N-terminal end of the protein. (2) It connects the polymerase to its nucleoprotein template and acts as a processivity factor. The polymerase itself is unable to bind to N, but P binds to both the polymerase (through another SLiM in the N-terminal part of the protein) and the NC (by binding on two adjacent N proteins). (3) P is a dimeric protein and this dimerization associated to its capacity to interact with different forms of N (monomeric $N^0$ and multimeric N-RNA complex) is essential for the formation of NEGRI's bodies (Nikolic et al., 2017b). (4) Finally, P also interacts using different modules or motifs with multiple host cell proteins, the dynein LC8 (Blondel et al., 2015), the focal adhesion kinase (Fouquet et al., 2015), the protein L9 (Li et al., 2016), the mitochondrial complex I (Kammouni et al., 2015), IRF-3 (Chelbi-Alix et al., 2006), STAT1 (Vidy et al., 2005), PML (Chelbi-Alix et al., 2006)(Blondel et al., 2002), nuclear import and export factors (Oksayan et al., 2012), BECN1 (Liu et al., 2017), and Cdc37/Hsp90 complex (Xu et al., 2016) (**Figure, 10**).

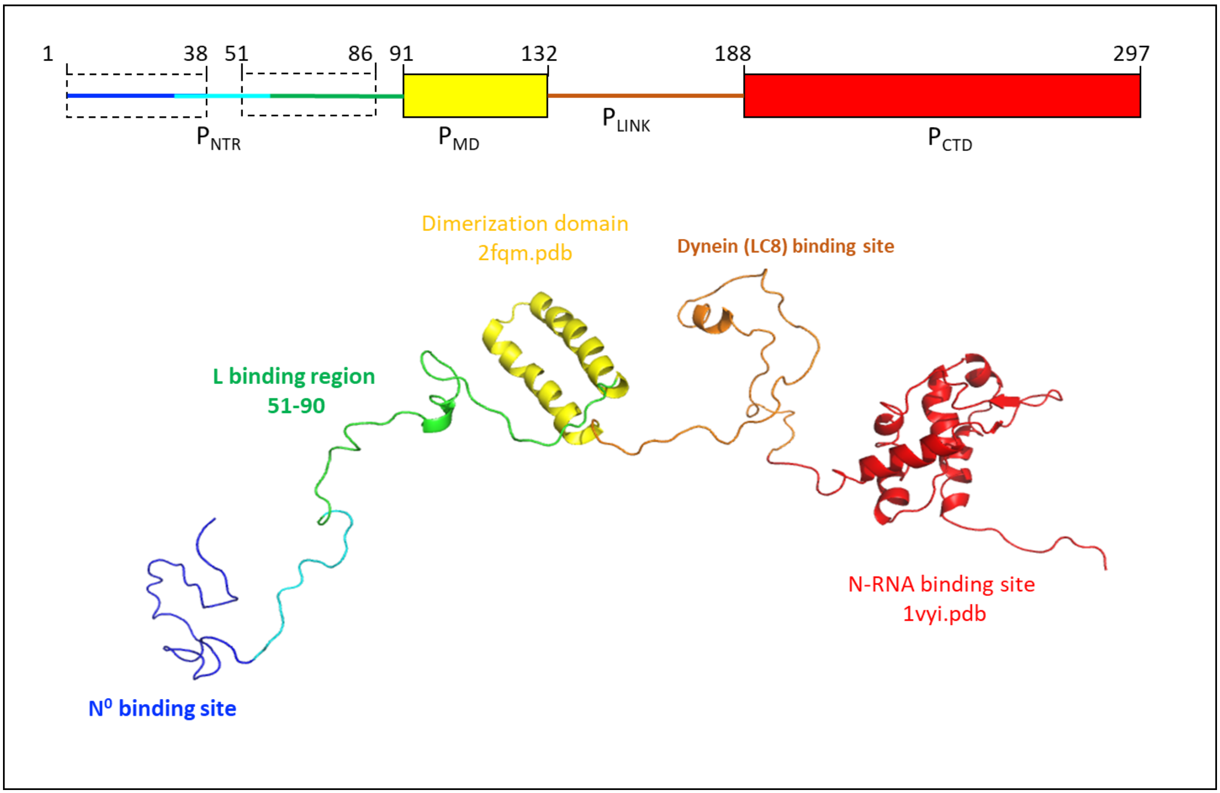

*Figure 9.* ***Overall organization of rabies virus phosphoprotein with different binding regions.*** *The known 3D structures of* $P_{MD}$ *and* $P_{CTD}$ *are shown as cartoon models and the disordered regions are shown as dotted lines.*

**RNA-dependent RNA polymerase (L)** is the most conserved protein within the family *Rhabdoviridae* but also within the order *Mononegavirales*. The RNA-dependent RNA polymerase (L) or Large protein is the major subunit of the viral polymerase enzyme complex. Together with its cofactor, phosphoprotein (P), it performs both transcription and replication activities of the viral genome (Emerson & Yu, 1975). Although the polymerase of the *Mononegavirales* have some sequence similarity with the viral polymerases of positive RNA viruses of which several structures are known (Poch et al., 1989), structural information of rabies virus polymerase L complexed with P was elucidated only recently (Horwitz et al., 2020) (**Figure, 11**).

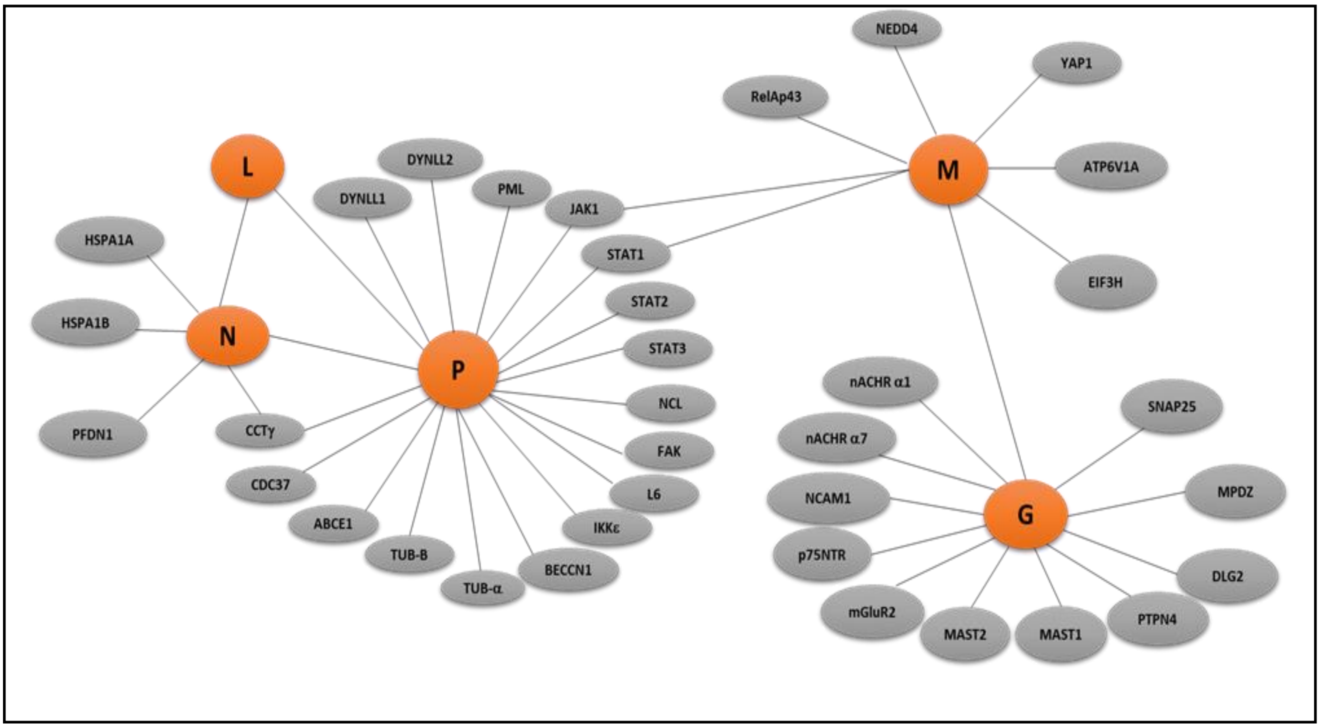

*Figure 10. Interaction network of RABV N, P, L, M, G (in orange) with cellular proteins. Adapted from* (Dhulipala & Uversky, 2022).

*Figure 11. PBD structure (6UEB) of Rabies L-P complex from cryo-EM. (Horwitz et al., 2020)*

The RABV RNA transcription and replication machinery is shown in the following figure **(Figure, 11).**

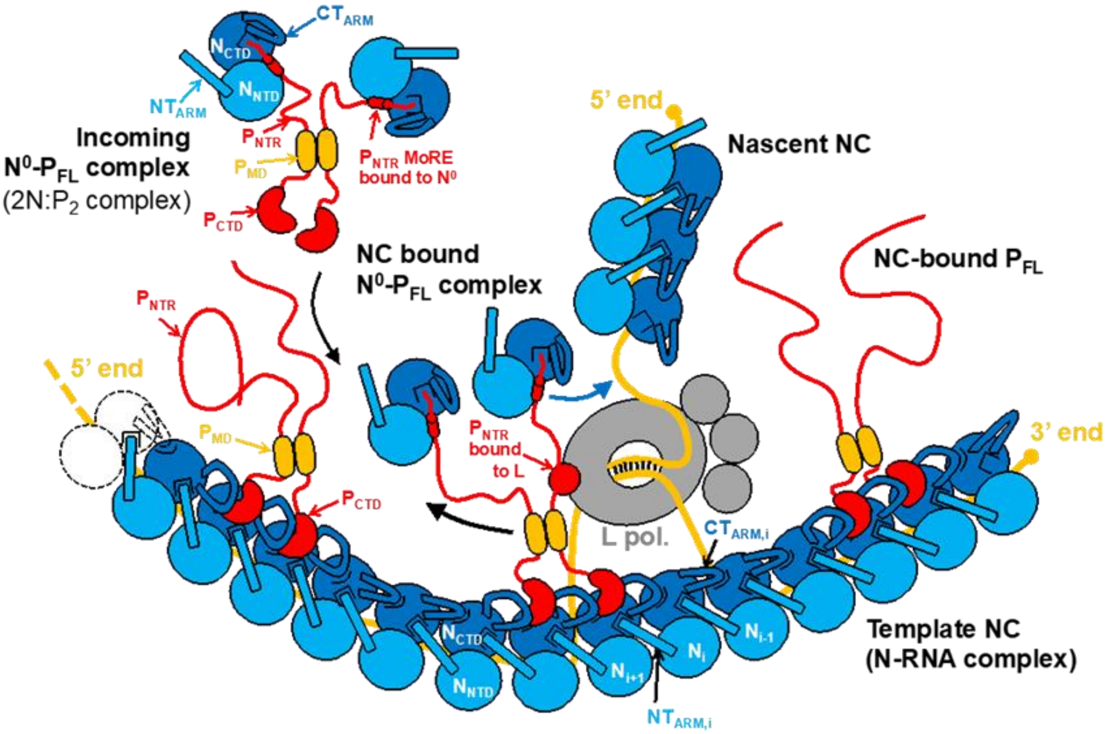

Figure 12. **Schematic representation of the RABV RNA transcription and replication machine**. The nucleoprotein (NNTD and NTARM in light blue and NCTD and CTARM in dark blue) coats the RNA (in orange), forming a long N–RNA complex that serves as template for the polymerase L is shown in gray and dimeric P is shown in red. P is attached to NC through its C-terminal domain ($P_{CTD}$, red bean-shaped domain) and the $CT_{ARM}$ of two adjacent N promoters (dark blue loops). P is also attached to L through PNTR (red ellipse). The simultaneous attachment of the $N^0$–P complex to NC and L could position the $N^0$ cargo near the site of RNA synthesis and would thus facilitate the incorporation of $N^0$ into the growing NC.

## 3. Rabies virus Negri's bodies (NBs)

Membrane-less compartments have been found to play a major role in the replication of different viruses including RABV. Early 1900's, both Adelchi NEGRI, an Italian pathologist and assistant of Camilio GOLGI, and Anna Wessels WILLIAMS, an American pathologist who had previously worked at the Pasteur Institute in Paris and contributed to develop the production of anti-rabies vaccine in the USA, independently discovered the presence of dense cytoplasmic, eosinophilic (stained in pink or red by eosin) inclusions in neuronal cells in brain sections of patients who died from rabies. NEGRI was the first to report his findings in 1904 in the *Bollettino della Società Medico-chirurgica di Pavia,* and these inclusions are now known as NEGRI's bodies (NBs). However, WILLIAMS improved the preparation and staining protocol turning it into an efficient, although *post-mortem*, diagnosis of rabies infections. This diagnosis is still in use today although in a somehow improved protocol. She never published her results, but in 1907, she was named chair of the American Public Health Association committee for the diagnosis of rabies in recognition of her accomplishments.

More recently, NBs were shown to be the viral factories, where the viral genetic material and viral proteins involved in RNA synthesis, namely the N, P and L proteins, accumulate and where active RNA synthesis (transcription and replication) occurred (Lahaye et al., 2009). We can hypothesize that by segregating the viral material from the cytoplasm, the formation of these inclusions increases the local concentrations of the different constituents of the viral polymerase machine and thus favors the transcription and replication and encapsidation of the viral genome. Additionally, these inclusions create a cellular compartment isolated from the rest of the cytoplasm, including from enzymes involved in antiviral functions and from host innate immune receptors.

Even more recently, NBs were shown to be membrane-less liquid compartments, formed by liquid-liquid phase separation. They had the typical features of liquid droplets, being spherical, fusing to form larger droplets or splitting into smaller droplets, reacting to hypotonic shock (Nikolic et al., 2017a) and Fast fluorescence recovery after photobleaching (FRAP). It was also shown by immunofluorescence that infection of cultured cells by the RABV induced the formation of spherical structures (in green) containing both N and P proteins (**Figure, 13A**). The inclusions grew in size around the nucleus ( in blue ) over the course of the virus cycle, while many smaller inclusions appeared at a later stage of the infection (Lahaye et al., 2009)

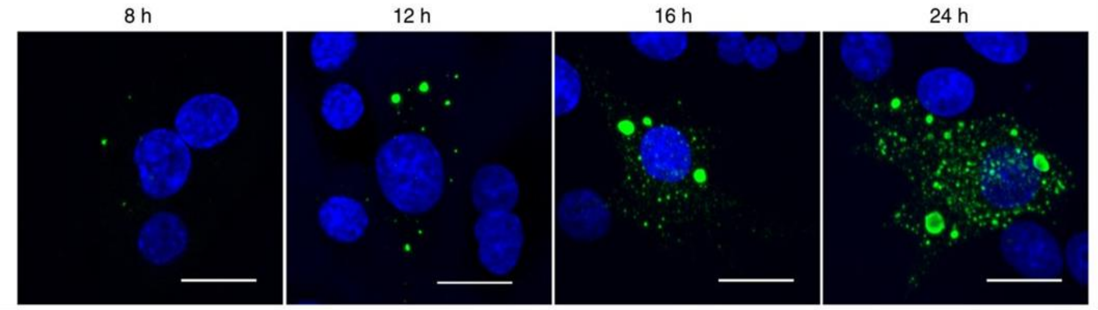

*Figure, 13A. Characterization of cytoplasmic inclusions in cell infected by RABV (Nikolic, 2017)*

In these studies, it was also demonstrated that similar inclusions could be reproduced in cultured cells by only expressing the recombinant RABV N and P proteins (**Figure, 13B**), and that liquid-liquid phase separation could be induced in solution by the RABV P protein alone in the presence of 5% PEG 8000 (Nevers et al., 2022).

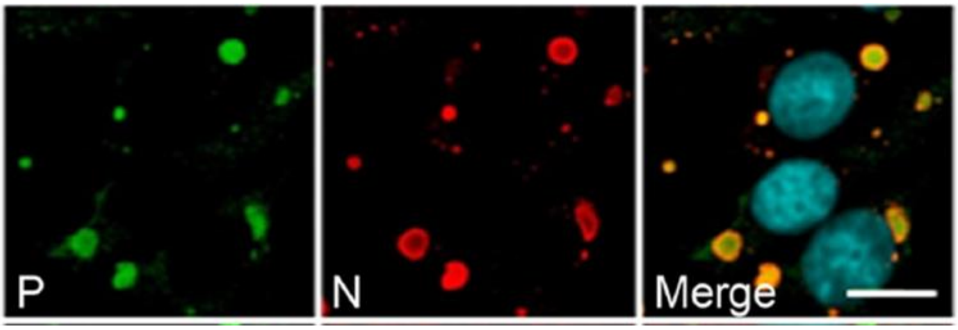

*Figure 13B. The Figure, shows the nucleus stained with DAPI (in blue) while N and P can be followed using anti-N antibody (in red) and anti-P antibody (green) respectively. Both proteins co-exist in liquid organelles around the nucleus (Nikolic et al., 2017)*

NEGRI's bodies seem to have several strategies to spread rapidly through the cell, including using viral NC. Ribonucleoprotein particles (RNPs) (complexes between RNA and macromolecules), can be ejected from NBs and transported along microtubules to form either new virions or secondary viral factories (Nikolic et al., 2017a).

Such factories are widespread in the viral world and have been identified for a variety of related viruses.

## 4. Liquid-like replication compartments in other Mononegavirales

Similar inclusions bodies of similar liquid nature have been found in cells infected by other negative-sense RNA viruses.

Paramyxoviruses including measles (Zhou et al., 2019), and pneumoviruses like metapneumovirus (Derdowski et al., 2008) use N and P to form liquid inclusion during infection.

Unlike rabies virus, in the case of Filovirus like Ebola virus, inclusions are first small, then they fuse together to form larger inclusions later in infection, as well as in the nucleus of cells infected with Borna disease virus (Charlier et al., 2013).

In the case of the Vesicular stomatitis virus VSV infection, stress granules are produced, co-localize with the viral factories, but cannot go inside (Dinh et al., 2013), as it was seen for other viruses.

For respiratory syncytial virus (RSV), viral RNA have been found in inclusion bodies of cell infected by the virus, and dynamic functional sub compartment were detected, in which newly synthesized mRNA was found , while N, P and L were excluded. The formation of these sub compartments of viral factories are completely related to the activity of RNA-dependent RNA polymerase (Rincheval et al., 2017).

Whereas, for Bunyaviruses, genomes segments are found ‘aggregated’ in spherical structures (Wichgers Schreur & Kortekaas, 2016), which resembles inclusion bodies.

The presence of similar structures in different families of non-segmented RNA viruses suggests that the formation of phase-separated compartments is a common feature of their replication, and this type of liquid phase transition may be more widely conserved across different types of viruses throughout evolution.

# 5. Liquid-liquid phase separation (LLPS)

The phenomenon of liquid-liquid phase separation is well-known and applied in colloid and polymer chemistry, in food science and in the separation of biomolecules (ATPS systems). These properties are not restricted to molecules in non-living systems, in biological macromolecules, such as proteins or nucleic acids, can also undergo this type of physical change and many living organisms have been found to use such process to drive cellular organization (Hyman et al., 2014).

In thermodynamics, a phase or a state of matter describes a system of uniform composition and physical state, where all intensive parameters (e.g. temperature) are uniform throughout the system. The typical states of matter are the solid, liquid and gas states. A phase transition is then a process in which a system change its state to a new one, e.g. from solid to liquid or from liquid to gas. Liquid-liquid phase separation (LLPS) is a physical process in which an initially homogenous liquid solution separates into two distinct coexisting phases with different solute concentration. In biological systems, two phases are formed, typically as liquid droplets in suspension into the aqueous solution, but also eventually as two overlaid liquid phases. One phase is enriched in concentrated biomolecules and the other is diluted, depleted of those components (**Figure, 14**).

LLPS has been extensively investigated in many different fields of research. Thus, binary or ternary mixtures of liquids unmix depending on composition (fractional ratio of the different components) and on external conditions (T, p, ionic strength,…). This is the case for example for the "ouzo effect" observed with several drinks. Ouzo is an alcoholic preparation that immediately becomes turbid when mixed with water, forming an emulsion, whereas limoncello is stable in the turbid state in about similar conditions. Both drinks are made of water, ethanol and of an additional organic molecule: anethole (ouzo) extracted from anise and limonene (limoncello) extracted from citrus zest. Anethole and limonene are highly soluble in ethanol but poorly soluble in water, and the ternary mixture undergoes phase separation forming liquid droplets in suspension in the remaining part of the liquid in some well-defined conditions and proportions(Vitale & Katz, 2003)(Sitnikova et al., 2005). These suspensions are either stable (limoncello) or metastable and completely decant into two transparent overlaying phases (ouzo).

LLPS is also very well-known in systems containing one or multiple polymers (Bates, 1991). Of particular interest as models for biological LLPS are aqueous solutions of polymers (Wall, 1954), which undergo:

(a) Segregative phase separation (e.g. poly-ethylene glycol/dextran mixtures).

(b) Lower critical solution temperature (LCST) transition or upper critical solution temperature

(UCST) transition.

(c) Complex coacervation as a form of associative phase separation of multiple species.

(d) Self-coacervation of polyampholytes (polyelectrolytes bearing both cationic and ionic groups).

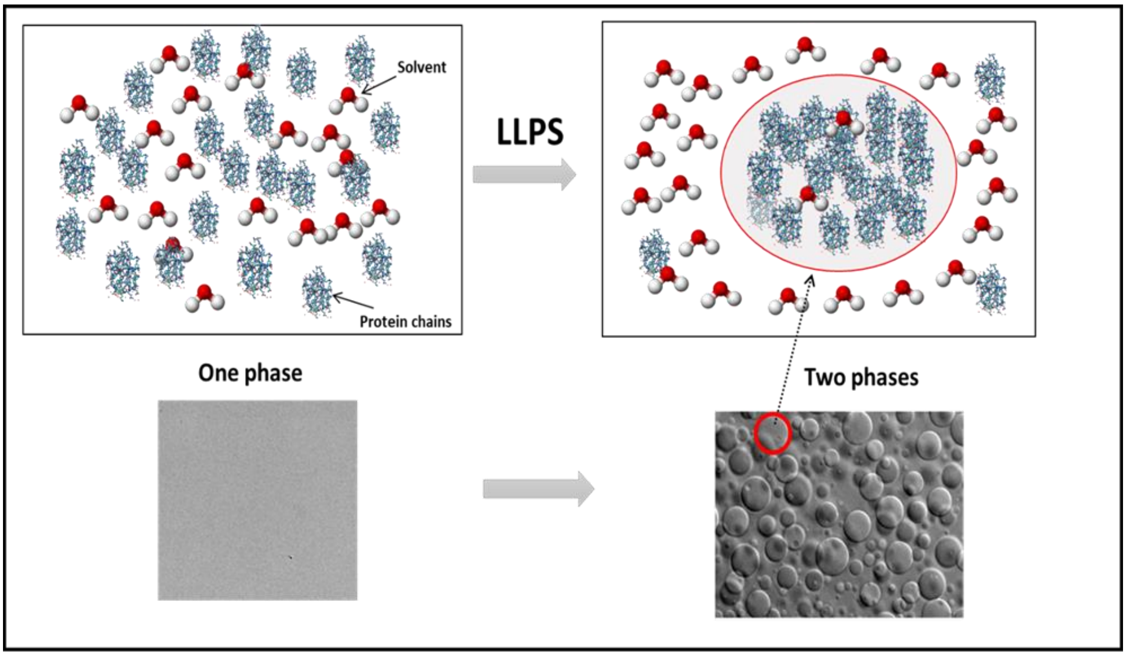

*Figure 14.* ***Schematic description of liquid-liquid phase separation****. When LLPS occurs, homogenous solution demixes.*

## (a) Phase diagrams

Phase diagrams are plots in 2D or 3D describing the regions of various physical (temperature, pressure…) or solution (concentration, pH, ionic strength,) parameters at which various phases are thermodynamically stable. The phase boundaries, which are the limits between two regions, show the values of the parameters at which two phases coexist in equilibrium.

Phase diagram can be established for pure substances or for mixtures. For example, in the phase diagram of water at different temperatures and pressures, the boundary between the solid and liquid phases is the plot of the freezing temperature as a function of pressure. For mixtures, a phase diagram defines conditions in which two or more different substances are miscible. In the case of liquid mixtures or solutions, liquid-liquid phase separation can occur in regions of varying parameters, leading to the existence of a single phase or to the coexistence of two or more phases.

Phase diagrams can describe a system with a lower critical system temperature (LCST) above which a phase separation occur, an upper critical system temperature, or both coexisting temperatures in one system (**Figure, 15**).

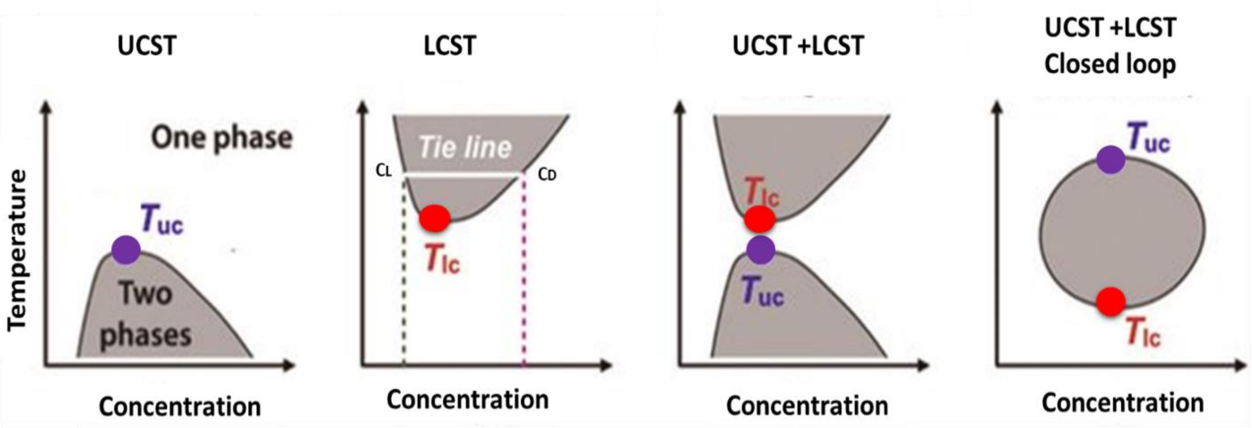

*Figure 15. Different types of phase diagrams. Adapted from (Ruff et al., 2018)*

## (b) Forces that control LLPS

Thermodynamics tells us that any molecular system evolved spontaneously towards its most stable state, meaning the state at the lowest Gibbs free energy. In addition, the second law of thermodynamics states that isolated molecular systems spontaneously evolve towards the state with the largest multiplicity (disorder), and thus, when multiple compounds are mixed together, mixing entropy should lead to homogeneous solutions. LLPS must thus be driven by interactions between the components of the solution. As solution conditions are changed either a single component must interact more with itself than with the other components and therefore forms a dense phase where it is more concentrated, or two components must interact by associating (forming a dense phase and a dilute phase) or segregating, each one in a separate phase.

A basic description of such process was reached in the 1940's independently by Paul FLORY (Flory, 1942)and Maurice HUGGINS (Huggins, 1942). For an incompressible mixture of two polymers, named A and B, they proposed that the change in free energy be given by:

$$\frac{\Delta Gm}{k_B T} = \frac{\phi}{N_A} ln(\phi) + \frac{(1-\phi)}{N_B} ln(1-\phi) + \chi \phi (1-\phi)$$

Where $\Delta G_m$ is the change in free energy for mixing, $N_A$ and $N_B$ are the number of segments in the polymer chains (approximated by the degree of polymerization), $\phi$ is the molar fraction of compound A and $\chi$ is the interaction parameter given by:

$$\chi = \frac{1}{k_B T}\left[\epsilon_{AB} - \frac{1}{2}\left(\epsilon_{AA} + \epsilon_{BB}\right)\right]$$

Where $\epsilon_{ij}$ are the contact energies between I and j segments. The FLORY-HUGGINS theory is a mean-field theory, meaning that all interactions to any one body are replaced by an average or effective interaction, sometimes called a molecular field.

According to these equations, if the interactions between A and B are favorable relative to the interactions between A and A and between B and B, then $\chi$ takes a negative value, and the interaction term adds up to the entropy of mixing and the mixing is spontaneous ($\Delta G_m < 0$). If the interaction between A and B is unfavorable, it opposes the mixing entropy and if larger than the entropy of mixing, the components A and B remain separated.

In some cases, the interaction parameter can be represented by an empirical function of temperature:

$$\chi = \alpha \frac{1}{T} + \beta$$

where $\alpha$ and $\beta$ are experimentally determined parameters. In these cases, the temperature-dependence of the interaction parameter can explain LLPS with an UCST or an LCST. More complex dependence of the interaction parameter can also explain the presence of both UCST and LCST in the same system.

### (c) Lower critical solution temperature (LCST) phase diagram

Phase separation is described by a phase diagram in a phase plane of two variables, such as concentration and temperature. In a binary or pseudo-binary system, one expects that in any given condition within the two-phase regime, two coexisting phases are present, *i.e.*, a dense phase of high protein concentration (C **dense**) and light phase of low protein concentration (C **light**).

A protein forms liquid droplets above the critical concentration (C **critical**) and a cloud temperature (T **cloud**) for phase separation; the liquid droplets are stable as long as the total concentration is above this critical point. Once the total protein concentration drops below the critical concentration, the compartments dissolve and the system comes back to a one-phase state where the molecules are uniformly distributed, and cannot undergo liquid-liquid phase transition (**Figure, 16**). In well-defined conditions of temperature and solution conditions, one would expect that the concentrations of the light and dense phases are constants but that their fraction volumes vary with protein concentration.

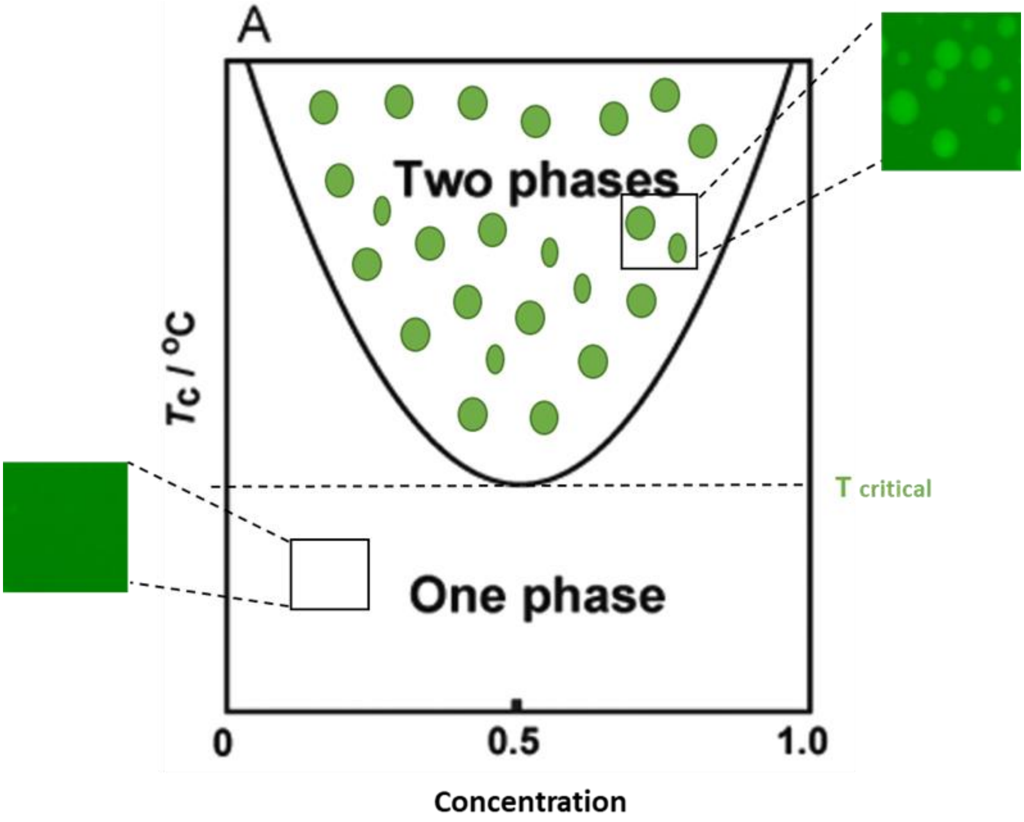

*Figure 16. Binary protein phase separation diagram with LCST*

## (d) Coacervation and LLPS

Polymers can also induce LLPS by coacervation; the term of coacervation is used in the literature to describe different processes. Historically, coacervation was used to describe LLPS induced by the association of two polymers of opposite charge, but its use has been extended to other types of interactions (de Jong Bungenberg,1930).

This process, by which a homogeneous solution of charged macromolecules undergoes liquid–liquid phase separation, was described in the early part of 20th century. In 1929, the coacervate was described as a drop or a layer, in which the particles gathered as "bees in a swarm". An intermediate state, i.e. a "non-precipitating" state exists between the transition from an initial state (the soil) to a final state (solid precipitant), called "unmixing", which can be manifested by a separation into two liquid layers or formation of droplets (de Jong Bungenberg & Kruyt, 1929).

Coacervation can be classified into two subtypes, complex and simple. A **complex coacervation** involves two or more polymers that form the coacervate via interactions of multiple components and can lead to the formation of structurally complex phases. A simple **coacervation,** involves a single polymer. Thus, Alexander OPARINE suggested in the first edition of his famous book "The origin of life" that liquid-liquid phase separation played a central role in creating the compartmentalization, predating the creation of the first cells and the appearance of the first living organisms on earth. His definition refers to the **self-coacervation** term or polyampholytes, which occurs when molecules of a single polymer interact with each other and form a network (e.g gel-like structure). It can be caused by changes in the chemical or physical properties of the liquid, such as pH, temperature, or concentration. This process is driven by the interactions, which can be electrostatic, hydrogen bonding, or hydrophobic interactions. In the second edition of his book, he proposed that membranes must have come first; arguing that the prebiotic soup contained molecules capable of forming cell-like structures (liposomes).

Coacervation is associated with various domains including pathological domains. For example, amyloid peptides are commonly associated with various human diseases, including neurodegenerative diseases such as Alzheimer's, Parkinson's, and type 2 diabetes (Najafi et al., 2021)(**Figure, 17**). These peptides can induce LLPS, although the role that Coacervation plays in amyloid aggregation is not understood (J. Phys. Chem. Lett. 2021,). Another example, illustrative of the diversity of the use of coacervation in biology, is in the marine world; some marine organisms produce extracellular coacervates to cope with the problems of adhesion and positioning underwater. These organisms secrete mixtures of polyelectrolytes and polymers that induce coacervation, whereas secretion of soluble polyelectrolytes would quickly be diluted in water (Kim et al., 2016)

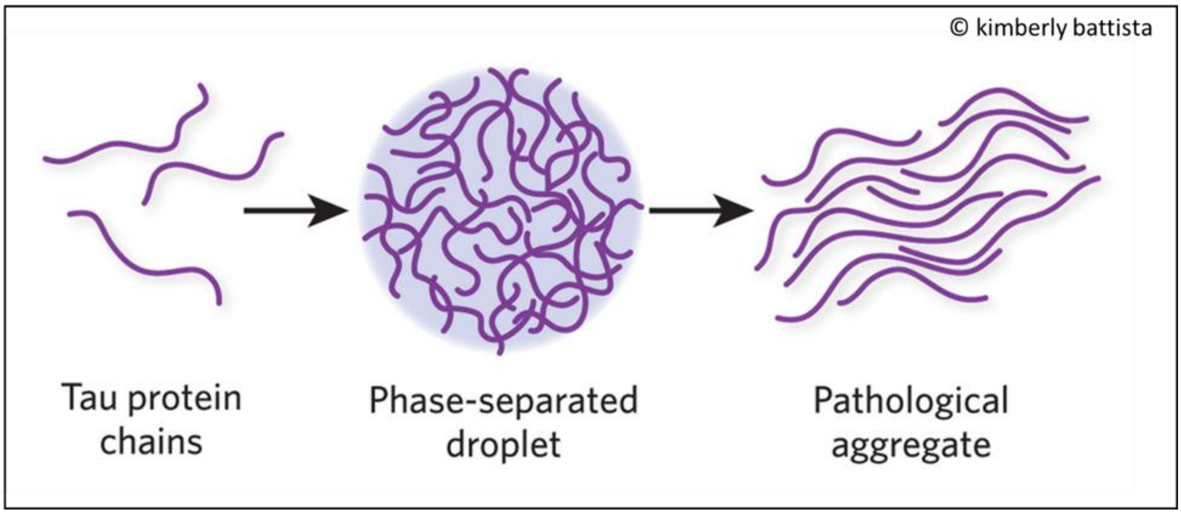

*Figure 17.* ***LLPS in disease:*** *Tau protein of Alzheimer's disease form phase-separated liquid droplets in neurons before developing into tau aggregates. Adapted from Kimberly battista*

The coacervation is an associative process that occurs when two or more polymers are mixed together and end up forming a new form (e.g. semi-solid phase forms). This process is driven by interactions, creating a network that can hold the liquids together. Both solute polymers are normally present in the dilute and dense phase. It describes generally the complexation between two electrolytes of opposite charge (**Figure, 18**). The phase separation by coacervation can involve different biological polymers, RNA, DNA molecules (Brangwynne et al., 2015b), peptides, or different proteins composed of multiple modular interaction domains and/or proteins containing intrinsically disordered regions (IDRs).

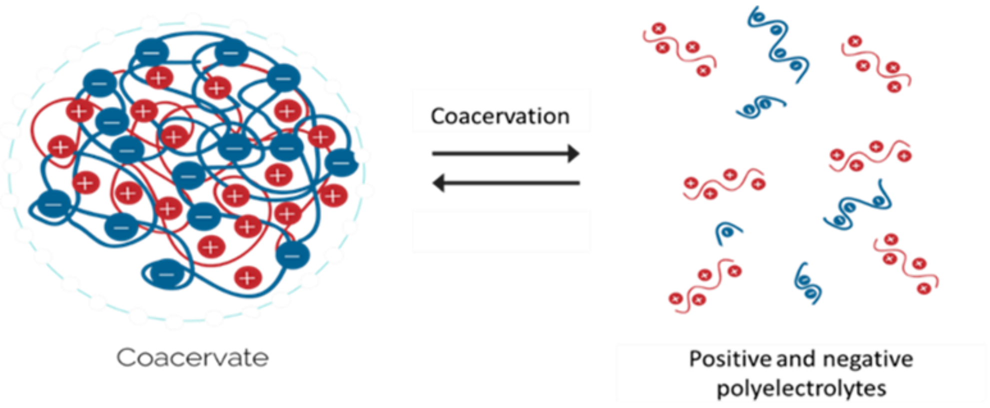

*Figure 18.* ***Schematic representation of Coacervation :*** *polyelectrolytes can phase separate into dense, polymer-rich regions called coacervates. Adapted from IGEM.org*

### (e) Intrinsically disordered proteins: the perfect molecular building blocks for inducing LLPS

Intrinsically disordered proteins (IDP) are proteins that are devoid of stable tertiary interactions. Some are entirely disordered, while others contain both long IDRs and folded domains. Both IDPs and IDRs therefore fail to adopt a well-defined three-dimensional structure in their isolated form, but for many of them, one part of the disordered region or the entire disordered region folds upon binding a partner (Dyson & Wright, 2005).

The discovery at the dawn of the XXI century, that a large number of human proteins were IDPs or contained IDRs, was the first stage of a revolution in the field of structural biology. Before, it was considered that any natural sequence of amino acids would correspond to a specific 3D structure (Dunker et al., 2001). The following findings that many IDPs had functions in cells and that their disordered state was essential for these functions was the second stage of this revolution, overturning the principle that the 3D structure determines the function. Indeed, IDPs play different roles in cells; they are notably involved in the signaling or in the assembly of multimolecular complexes.

More recently, many IDPs and proteins containing IDRs have been shown to provide the driving force for bimolecular liquid-liquid phase separation, potentially due to their close similarity to well-known multiphase systems observed with synthetic polymers ((Uversky et al., 2015)(Nott et al., 2015)). The determination of the link between IDRs and phase transitions has generated an increased interest in the conformational behavior of IDRs. The phase transition being considered as a form of aggregation that allows the formation of clusters, the IDPs would be perfect candidates for the formation of LLPS.

Since they have a high degree of conformational flexibility, they easily interact with other IDPs and form a network.

In the case of IDRs, LLPS can be promoted, by weak multivalent interactions, with several interacting motifs (SLiMs) or stickers *(*(Elbaum-Garfinkle et al., 2015)(Nott et al., 2015)*;*(Wang et al., 2018)*)*. Recent studies showed that phase separation might depend also on electrostatic interaction; *c*ompaction of proteins is mainly due to intra-molecular and electrostatic interaction. The relation between these interactions suggest that more compacted and dense proteins in matter of charged zones are most likely to form condensates (Somjee et al., 2020).

## 6. Neutrons and X-ray scattering studies of LLPS

Small-angle scattering is a biophysical method that provides information about the average molecular mass, size and shape of particles in solution. It allows studying spatial association of macromolecules and assemblies by changing different experimental conditions (such as temperature, pH and salinity) or for studying reaction in real time.

Due to the short wavelength of the probe radiation (0.01 nm - 3 nm), information can be obtained in the useful range of 1-1000 nm.

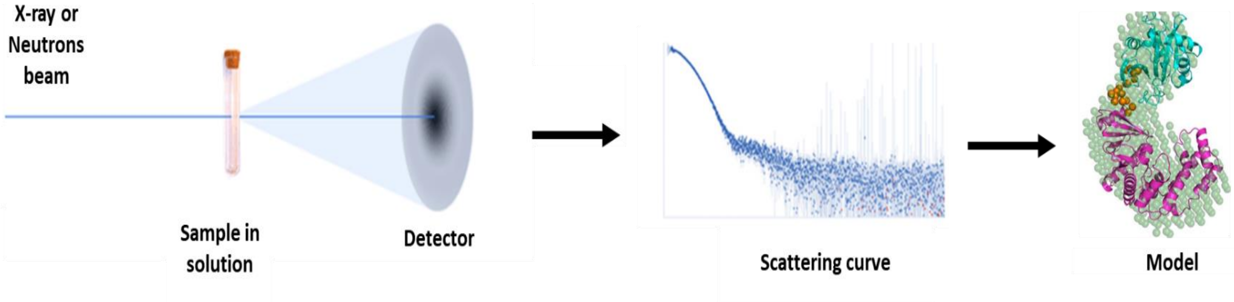

*Figure 19. Small angle scattering experiment*

The scattering of a solution of particles (particles + medium) is measured isotropically around the incident beam and then radially averaged to yield a plot of the scattering intensity as a function of scattering vector q (**Figure, 19**). The intensity and shape of this curve inform us about the structure of the particles and about interparticular interactions.

The scattering vector q is a coordinate in a reciprocal space and thus scattering at low q values, corresponding to small angles, probes structure at large length scales, while scattering at large q values, corresponding to large angles, probes structure at small length scales.

For a population of discrete scatterers, the scattering intensity is written:

$$I(q) = \frac{N_P}{V_{tot}} \cdot \langle V \cdot \Delta SLD \rangle^2 \cdot P(q) \cdot S^{eff}(q)$$

where:

- $N_P$ is the total number of particles in the observed volume
- $V_{tot}$ ($\frac{N_P}{V_{tot}}$ is the concentration of particles, called the *number density)*
- $V$ is the volume of the particle
- $\Delta SLD$ is the average contrast between the particle and medium (difference in scattering length densities).
- P(q) is the normalized form factor ($P(0) = 1$) describing the shape and size of the particle.
- $S^{eff}(q)$ is the effective structure factor accounting for interactions between particles ("effective" can be dropped only when interactions are identical for all particles in all directions, i.e. essentially for monodisperse spheres with a homogeneous surface potential).

## (a) Structural parameters determination from the scattering curve

In a system where interparticul interactions can be neglected, that is in well i.e dispersed (no aggregation) dilute (< 1 %) solutions of particles with no electrostatic attractions or repulsions (i.e. uncharged particles, or medium with low relative permittivity, or high ionic strength resulting in the screening of electric charges), the structure factor is neglected and reduced to $S^{eff}(q) = 1$. The forward scattering is then given by:

$$I(0) = \frac{N_P}{V_{tot}} \cdot \langle V \cdot \Delta SLD \rangle^2$$

### Molecular mass and radius of gyration ($R_g$)

Two relevant parameters can readily be obtained from SAS data in the low q range where the signal/noise ratio is the largest: Molecular mass and radius of gyration ($\mathrm{R_g}$) . The scattering intensity extrapolated to zero angle ($I_0$) is directly proportional to the average molecular mass of the particles in solution. By using a suitable calibration of the incident beam, this measurement directly reports on the average molecular mass. The variation of the scattering intensity with scattering angle (actually with the scattering vector q), informs about the average size of the particles in the form of an Rg that is independent of the shape of the particle.

In a short range of q, André GUINIER showed that the natural logarithm of scattering intensity varies linearly with q2 and that the slope of such a graph directly yields the value Rg value. Typically, for globular proteins, the GUINIER region is limited to q values such that q. $R_g$ < 1.3 and for random coil chains to q values such that q.Rg < 1.1. In these limits, the GUINIER approximation is given by :

$$\lim_{q\to 0} I(q) = I(0) \cdot exp\left(-\frac{q^2 R_g^2}{3}\right)$$

where $R_g$ represents the radius of the gyration; that is, the square root of the average squared distance of each scatterering center from the particle center, which is similarly defined as the mechanical Rg except based on SLD rather than density, and quantifies the spatial spread of scattering length of the scatterers:

$$R_g^2 = \frac{\int_0^{R_{max}} SLD(r) \cdot r^2 \cdot dr}{\int_0^{R_{max}} SLD(r) \cdot dr}$$

Note that for spheres with heterogenous distribution over their radii, experimental value is given by $R_g^2 = \frac{3}{5}\frac{\langle R^8 \rangle}{\langle R^6 \rangle}$, indicating that Rg is heavily influenced by larger particles.

## $\boldsymbol{I(0)}$ is proportional to the weight average molecular mass ($\boldsymbol{M_w}$)

The analysis of the scattering data by using the GUINIER approximation also provides a measure of the intensity at zero angle $I(0)$. For macromolecules, the equation can be written as a function of the concentration $c$ in g·mL$^{-1}$ (i.e. g·cm$^{-3}$) and the molecular mass $M_w$ in g·mol$^{-1}$:

$$I(0)/\mathrm{cm}^{-1} = c \cdot \frac{M_w}{d^2} \cdot \frac{\Delta SLD^2}{N_A}$$

Where d is the apparent density in g·cm-3, **ΔSLD** the contrast in cm-2 and $\mathbf{N_A}$ is Avogadro's number in mol-1. Provided $\mathbf{I(0)}$ is expressed on an absolute scale in units of cm-1, the weight average molecular mass is then given by**:**

$$M_w/\mathrm{g} \cdot \mathrm{mol}^{-1} = \frac{I(0) d^2 N_A}{c\, \Delta SLD^2}$$

A GUINIER plot where log I (q) is plotted as function of $q^2$ is a straight line from which and $R_g$ and $I(0)$ can be extracted (**Figure, 20**). The q-range at small angle over which the GUINIER approximation is valid ($q.R_g < 1, 3$ for globular proteins) is wider for small particles (small Rg) than for large particles (large Rg). In practice, deviation from linearity or absence of linearity in the GUINIER plot indicate the occurrence of interparticle interactions, either aggregation or repulsion. Typically, the independence of the GUINIER plot on particle/macrolecule concentration is used to evaluate the quality of a sample and demonstrate the absence of inter-particle interactions (**Figure, 20**).

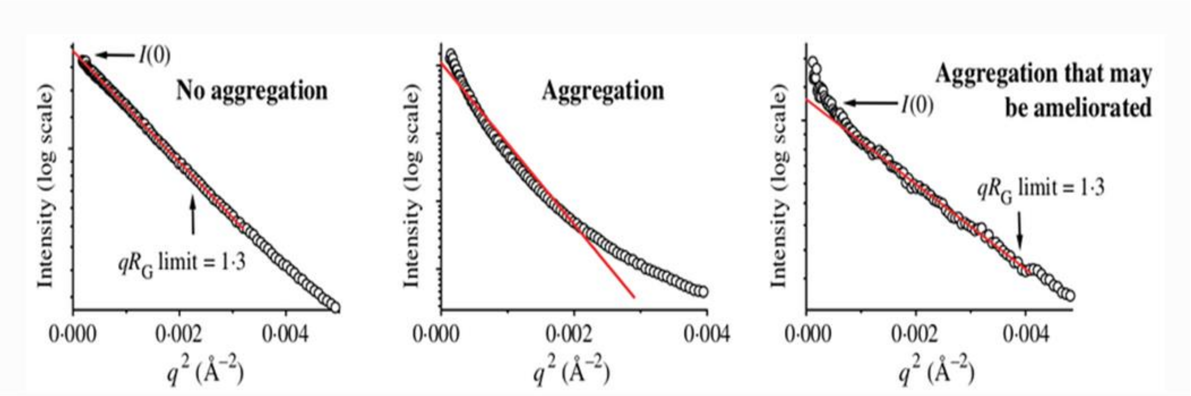

**bioxtas-raw**

*Figure 20. Assessing the quality of a sample using Guinier analysis.*

### Invariant scattering $Q$:

The scattered intensity is related to the mean square deviation of SLD in the sample through the invariant. In the case of two SLD domains (particle of homogeneous SLD and medium) of contrast $\Delta SLD$, with $\phi_P$ the volume fraction of particles:

$$\tilde{Q} = \int_0^\infty I(q) \cdot q^2 \cdot dq = 2 \cdot \pi^2 \cdot \phi \cdot (1 - \phi) \cdot \Delta SLD^2$$

For a mostly convex scatterer, with constant SLD of the scatterer and of the medium, Günther POROD has shown that the intensity decays at high q following $a_P \cdot q^{-4}$ for a straight interface between medium and particle. This situation is however rarely obtained with proteins, as they tend to have disordered domains.

The volume of the macromolecule-undergoing scattering can be calculated from $I_0$ and the Porod invariant $\tilde{Q}$ (Porod, 1982) in dilute conditions when $1 - \phi \approx 1$ and assuming negligible interactions: $S(0) \approx 1)$ :

$$V_P = 2 \cdot \pi^2 \cdot \frac{I(0)}{\tilde{Q}} \cdot \frac{(1-\phi)}{S(0)} \approx 2 \cdot \pi^2 \cdot \frac{I(0)}{\tilde{Q}}$$

Where the experimental invariant $\int_0^\infty I(q) \cdot q^2 \cdot dq$ can be determined from the data, but requires extrapolations between $q_{min}$ and 0 and between $q_{max}$ and ∞, which is usually done via the Guinier and Porod formula respectively:

$$\tilde{Q}^{exp} = \int_0^{q_{min}} I(0) \cdot \exp\left(-\frac{q^2 R_g^2}{3}\right) \cdot q^2 \cdot dq + \int_{q_{min}}^{q_{max}} I(q) \cdot q^2 \cdot dq + \int_{q_{max}}^{\infty} \mathrm{a_P} \cdot q^{-4} \cdot q^2 \cdot dq$$

The advantage of equation is that it does not consider any structural parameters, making it a useful tool to evaluate changes in the composition (for example phase-separation) due to external factors such as time or temperature.

## Pair-distribution function P(r):

The pair distribution function represents the Fourier transform of the SAXS scattering curve. It indicates the distances between atoms in the scattering particle, it can be determined directly from the electron density using the following expression:

$$P(r) = r^2 \left\langle \int_V \Delta\rho(\boldsymbol{r}) \Delta\rho(\boldsymbol{u} + \boldsymbol{r}) \mathrm{d}\boldsymbol{r} \right\rangle_\Omega .$$

Where Dmax is the maximum distance between the scatterers in the scattering particle. This parameter is useful for the characterization of proteins, and the distance distribution plot ( P(r) as a function of r) informs about the quality of the sample. Typically for macromolecules, P(r) = 0 at r= 0 and at r greater than Dmax, the maximum extension of the particle.

This function can be difficult to calculate, especially with proteins that contain disordered regions since the estimation of Dmax using indirect Fourier transformation requires fixing the value of Dmax, which can be difficult for chains of different lengths.

The shape of the P(r) function allows estimating some characteristics of the global shape of the studied molecule:

- Globular molecules have a bell-shaped P(r) function, whose maximum corresponds to Dmax/2
- Elongated particles have a maximum of P(r) function for r < Dmax/2;
- The P(r) function of flattened particles presents an enlarged maximum for r < Dmax/2 while that of holed particles presents a maximum for r > Dmax/2.

Besides giving us information on the quality and inter-particle boundaries of the protein, this function allows us also to calculate $R_G$ and $I_0$. Unlike the GUINIER method, this function takes into account the polydispersity and aggregation in a solution since the calculation is performed using the entire range of q values and is not limited to the small q region, which is particularly affected by the presence of aggregates.

$$I(0) = 4\pi \int_0^{D_{\max}} p(r)dr$$

$$Rg^2 = \frac{\int_0^{D_{\max}} r^2 p(r)dr}{2\int_0^{D_{\max}} r^2 p(r)dr}.$$

## Kratky plot

Small angle scattering is considered as a good method to identify and characterize protein without folded domains. The Kratky plot [$q^2 I(q)$ vs q], which can be calculated directly from the scattering curve, gives indication on the flexibility and folding of the protein.

For folded proteins, the Kratky plot yields a peak. The position of the peak provides some information about the overall size of the protein; extended polymers, such as random coil peptides, follow the POROD–KRATKY worm-like chain model (Kratky & Porod, 1949). Random coil or unstructured peptides lack the characteristic peak and are linear with respect to q in the large q-region (**Figure, 21**).

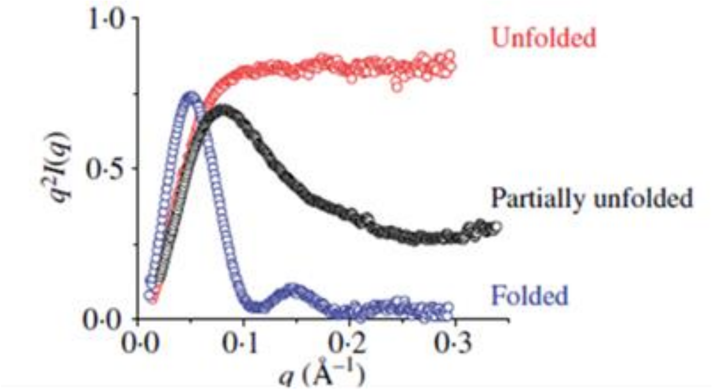

Christopher D Putnam

*Figure 21.Evaluation of the flexibility of a sample using the Kratky plot. Adapted from* (Putnam et al., 2007)

### (b) Choosing X-ray or neutrons:

Although the basic principles of X-ray and neutron scattering are similar, the two techniques have distinct characteristics and abilities. The selection between them depends on the specific experimental needs and the nature of the sample being studied.

Neutrons provide a unique contrast mechanism, which is based on the difference in coherent scattering length between hydrogen and deuterium. This allows the study of the hydrogen/deuterium distribution in a sample and can provide valuable information about the dynamics and interactions within a sample.

Additionally, it allows varying the scattering density by isotopic substitution, which is not possible with X-rays. This variation of the scattering density is used to study the internal structure of complexes of macromolecules such as proteins, nucleic acids and lipids, which have different mean neutron scattering densities. At certain ratios of $H_2O$ to $D_2O$, called match points, the scattering from the macromolecules equals that of the solvent, and is thus eliminated by subtracting the scattering from the buffer.

The scattering length density is different for different types of macromolecules and thus the match points are found at different $H_2O/D_2O$ ratio, providing a method to investigate complexes or mixtures of macromolecules. Typically, for proteins the match point is around 40-45% $D_2O$ (**Figure, 22**), and at that concentration, the scattering from a naturally hydrogenated protein will be indistinguishable from that of the buffer. This is used when we are interested in the shape of one component in a complex, making the second component "visible", in order to study how it changes upon complex formation. Additionally, in the case of a protein-protein complex, if one of the component is

prepared in a deuterated form, this method allows to see both protein independently at two different $H_2O/D_2O$ ratio, as the match point for a deuterated protein is around 100% $D_2O$.
Another advantage of neutron scattering is the lack of radiation damage makes neutrons a valuable tool for studying delicate or sensitive samples.

SAXS on the other hand is a powerful method for investigating the structures and conformations of biological molecules such as proteins, particularly for studying equilibrium systems like oligomers and protein mixtures. Its ability to probe a wide range of dimensions and molecular motions makes it a useful tool for understanding complex biological systems. The main advantages of SAXS experiments over neutron scattering is that they require less sample volume and lower concentration compared to neutron scattering, and it can be easily performed using X-ray sources such as synchrotron radiation.

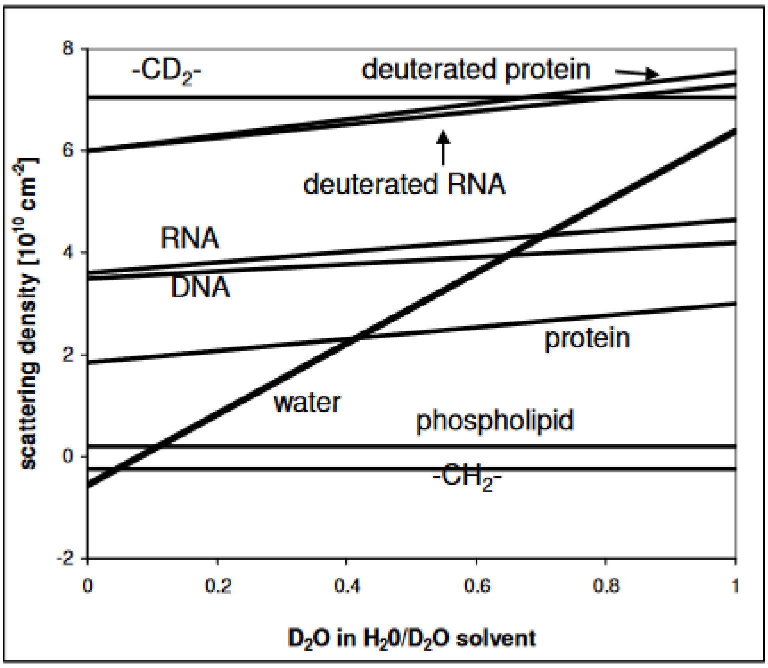

*Figure 22. Scattering density of various biological macromolecules. Adapted from* (Zaccai et al., 2016)

Based on the theory that phase separation is induced by the interaction between phosphoprotein and nucleoprotein, the plan during this project was to perform a small angle neutrons scattering experiment in which the phosphoprotein was deuterated and the nucleoprotein hydrogenated.

Unlike physico-chemistry, the sample is very limitating in biology, the sample volumes are reduced and therefore the experiences too. Moreover, both SAXS and SANS require highly pure samples, a first step of quality control should be done to ensure that the sample is well characterized before the scattering experiment is performed. If impurities of high molecular massare present in the solution, this can contribute strongly to the scattering signal and bias the data especially at low q. To this purpose, the quality control of our samples, which include the expression, and purification of proteins was very time consuming.

Few years ago, a complex produced in our lab of [**N**$_{\Delta 21}^{\mathbf{0}}$ (N protein without 21 first AA) + **P** ] of VSV (vesicular stomatitis virus) from the same family as rabies virus, *Rhabdoviridae*, was measured using isotopic variation via small angle neutrons scattering (Yabukarski et al., 2016). The complex of P+N was tested in different ratio of $H_2O/D_2O$; the deuterated P in red is visualized alone at 40% of $D_2O$ while N is seen alone at 100% of $D_2O$ (**Figure below, A**)

After demonstrating that $D_2O$ have no effect on the protein, by comparing both $H_2O$ and $D_2O$ scattering curve, each individual components within the N$_{\Delta 21}^{0}$P$_{FL}$ complex was analyzed according to the scattering curves shown below.

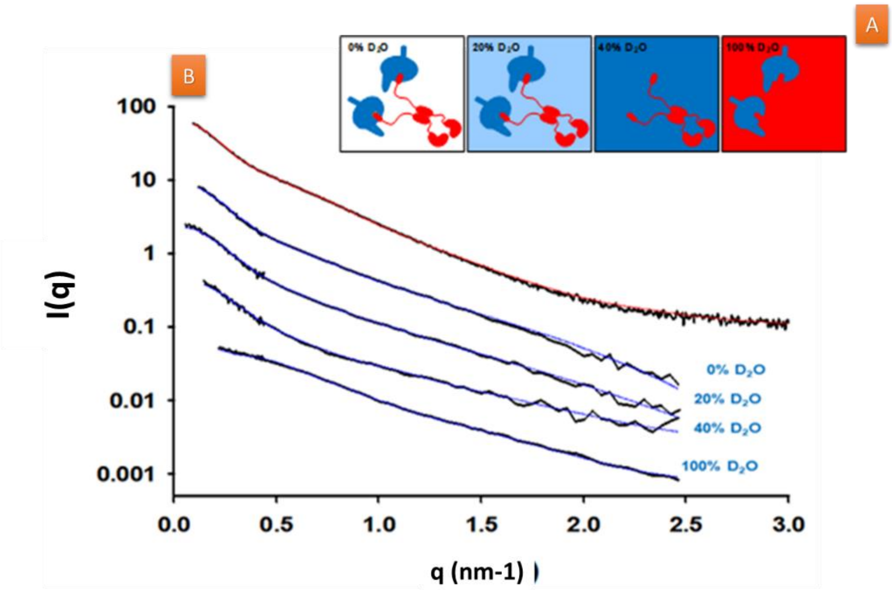

*Figure. **(A).** Representation of the contrast-matching SANS experiments; P is shown in red and $N_0$ in blue. **(B)** Fitting of SAS data at four different H2O/D2O ratio are shown in black and the fitted lines for a representative selected ensemble of 40 conformers are shown in red (SAXS) and blue (SANS). (Yabukarski et al., 2016)*

Data of individual protein (either P or N) has shown similar results as for that obtained for $N_{\Delta 21}{}^{0}$–$P_{60}$ complex and showed that the proteins has similar dimensions in its bound and free forms. In addition to other results, this experiment showed the co-existence of different stoichiometries of both proteins in the solution (Yabukarski et al., 2016).

### (c) Examples of the use of neutrons and X-rays scattering for studying LLPS

In order to better understand the LLPS phenomenon in biology, many studies have been performed on polymer solutions and more recently on protein solutions, which induce liquid-liquid phase separation. Even if much remains to be elucidated in this field, the uses of neutrons and X-rays have been of significant help in the understanding of these phenomena.

In literature, we found studies of systems exhibiting a lower critical solution temperature (LCST). Thus, BSA (bovine serum albumin) undergoes this type of LLPS. In their study (Da Vela et al., 2016), studied BSA in the presence of various trivalent salts. Very small-angle neutron scattering (VSANS) was combined with ultra-small-angle X-ray scattering (USAXS) to monitor the growth of the characteristic length over long times, in the absence of radiation damage. These experiments showed that a peak of structure factor increased in intensity and shifted towards small q with time, indicating slow reaction kinetics (**Figure, 23**). The effects of temperature and salt concentration were also clearly visible in USAXS. In addition, the use of neutrons and X-rays allowed tracking the changes in structures on the millimeter scale during the phase-separation process, and indicated that the kinetics of phase separation follows a spinodal decomposition.

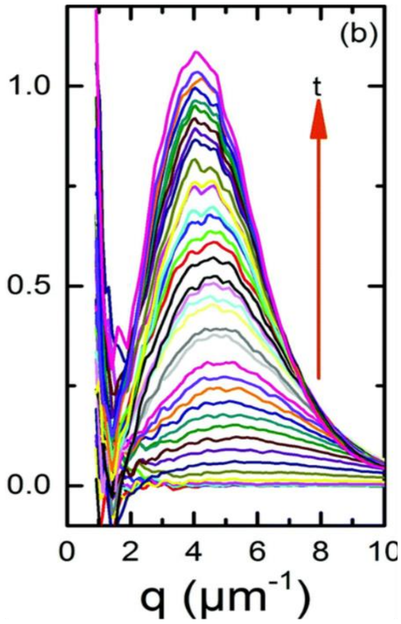

*Figure 23.USAXS profiles for a sample obtained of 175, mg/mL BSA and 42mM YCl, after a temperature jump to* $T_{jump} = 35℃$ (Da Vela et al., 2016).

Another example of the use of small-angle neutron is the study of (Prabhu et al., 2021). They investigated the interactions between two polymers, sodium polystyrene sulfonate and pollyldimethyl ammonium chloride at room temperature, which results in a liquid-liquid phase separation with a complex coacervate and a diluted phase. They used ultra-small angle neutron scattering (USAXS) to observe the kinetics of formation of the liquid droplets. They used USANS (**Figure, 24**) at various time to measure characteristic lengths during the phase separation, revealing that poly-disperse size droplets increases with time, while the average radii remain unaffected.

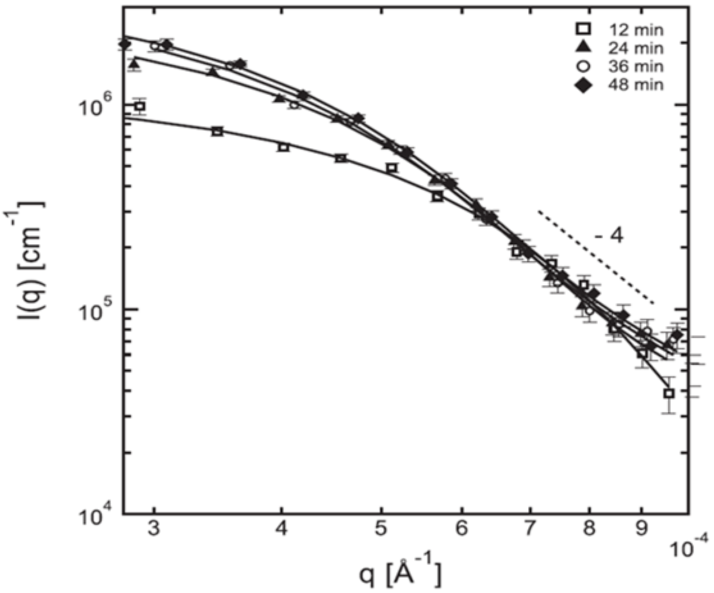

*Figure 24. USANS data at 45℃ as a function of time after heating from 22℃ to 45℃. The data shown as a function of equilibration time are fit by a model of polydisperse spheres. At the high q region, a lope of* $q^{-4}$ *is observed and expected for sharp interfaces* (Prabhu et al., 2021).

# II. Objectives

Relying on the recent discoveries that : (1) NEGRI’s bodies are liquid compartments formed by liquid-liquid phase separation and that (2) the recombinant expression of only RABV N and P in cultured cells was sufficient to induce phase separation and the appearance of cytoplasmic droplets recapitulating NBs properties (Nikolic et al., 2017a). And (3) on the work performed on both proteins in the group for more than 15 years ((Gerard et al., 2007, 2009; Gérard et al., 2022), (E. A. Ribeiro et al., 2008; E. de A. Ribeiro et al., 2009)(Leyrat et al., 2010, 2011, 2012) (Yabukarski et al., 2016)). We planned to reconstitute the process of LLPS *in vitro* with highly purified and well-characterized RABV nucleoprotein and phosphoprotein and to use neutron scattering experiments on different instruments at the institute Laue-Langevin (ILL) to probe these molecular processes at different time and length scales. Small angle neutron scattering with partial deuteration is pivotal to study the structural arrangement of proteins in the dense phase, with RABV proteins involved in this project, N and P, it can be used to understand how these proteins interact in the phase separation process, matching out one of the two proteins. We also planned to use X-ray and light scattering complementary methods to better understand LLPS process , these studies should provide new insights into the nature and strength of the interactions underlying the liquid-liquid phase separation and the structural arrangement of the proteins in the condensed phase.

**The specific goals of my PhD project were:**

- To set up the expression and purification protocols for the different proteins and protein complexes needed for neutron and x-ray scattering studies.
- To reproduce liquid-liquid phase separation *in vitro* and device experimental methods to measure the concentration and volume of both condensed and diluted phases.
- To establish phase diagrams describing how the system reacts to different experimental conditions (temperature, NaCl concentration, protein concentration,…).
- To use different biophysical methods to characterize the dimensions (Rh, Rg..), stoichiometry and shape of the proteins in the dense and possibly light phases at different points of the phase diagrams.

# III. Results

## 1. Establishment of the system

### (a) Protein production and quality control:

According to our initial hypothesis, the phase separation should be induced in the presence of both phosphoprotein (P) and nucleoprotein (N). We thus set up protocols for the production and purification both RABV P and N.

We expressed and purified the full-length RABV phosphoprotein in bacteria as well as different a variant deleted of the dimerization domain ($P_{\Delta 91-131}$), we purified a sample of deuterated P ($P_D$) and we chemically labelled the protein with a fluorescent probe (FAM-labeled P).

The nucleoprotein can exist either in complex with RNA (N-RNA complex) or with the phosphoprotein in the form a soluble $N^0$-$P_{68}$ complex. We thus devised a strategy to generate the $N^0$-$P_{68}$ complex between full-length RABV N protein ($N^0$) and the chaperon module of P, a peptide of 68 AA derived from the N-terminal end of P. We also generated a construct with RABV N in fusion with the mCherry protein. Our strategy was to use this complex in order to form N-RNA complexes with synthetic RNA molecules of well-defined lengths, and thus to generate homogeneous samples of NCs. We have produced and purified $N^0$-$P_{68}$ complex and $N^0$-$P_{68}$ complexed with an m-cherry protein ($N^0$-$P_{68}$-mCherry) both in bacteria and insects cells.

Unless otherwise specified, all samples were prepared in 20mM Tris-HCl buffer pH 7.5 containing 150 mM NaCl and 0.5 mM TCEP.

- ***RABV Phosphoprotein***

The construct of P contained a His-tag at its C-terminal extremity (**Figure, 25A**), after a first step of purification of the RABVP using a Ni-NTA column, and a second step by size exclusion chromatography, the samples were analyzed by SDS-PAGE to check the level of purity. RABVP migrates above the marker of 40k Da although the molecular mass of the monomer is only 33kDa (**Figure, 25B**). This abnormal migration is explained by the presence of a long I that is rich in negatively charged residues; this charged region do not bind SDS molecules like the rest of the protein, affecting the migration of the protein throughout the gel.

The samples were analyzed by SEC-MALLS-RI (size exclusion chromatography with multi-angle light scattering and refractometry) (**Figure, 25C**). The weight-averaged molecular mass was calculated from scattered light intensity and protein concentration obtained from excess refractive index. According to the theoretical mass of 33 kDa for one monomer, the value of molecular mass of 65 ± 2kDa confirmed that, in solution, RABV P forms dimers (Gerard et al., 2007, 2009).

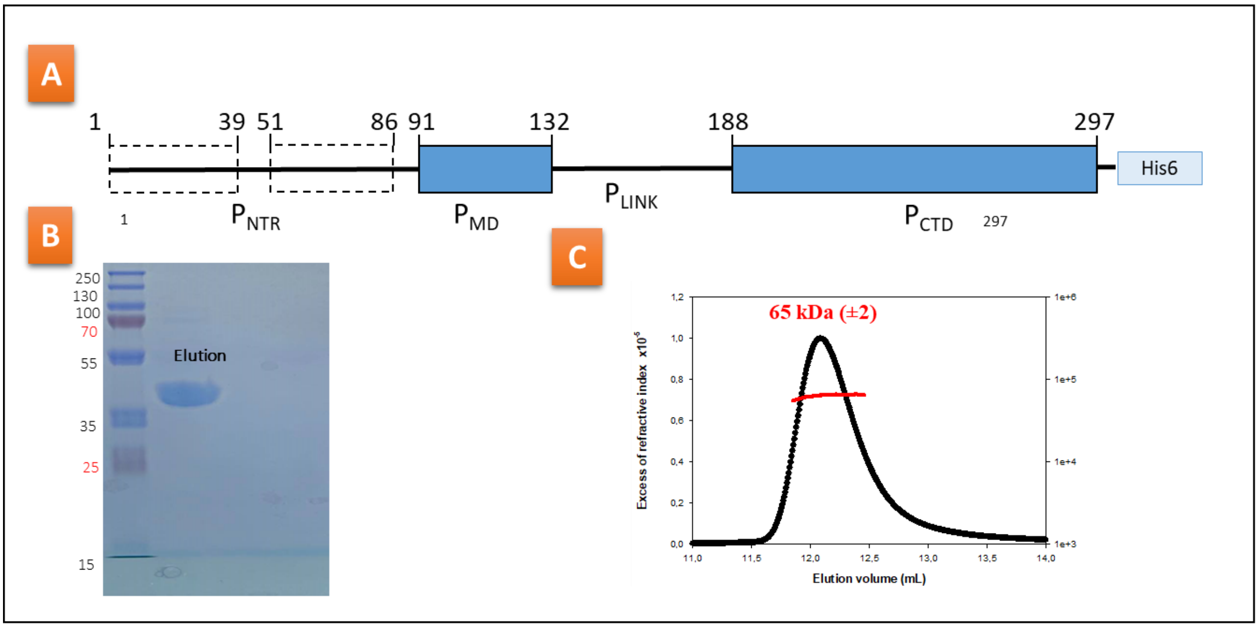

*Figure 25. (A)The schematic construct of RABV P showing an unstructured N-terminal domain and a structured C-terminal domain. (B) The purity of RABVP checked with 15% SDS PAGE visualized with Comassie blue. (C) SEC-MALLS analysis of RABVP, the red dots show the MM calculated from the laser light scattering*

To further validate the quality of our samples, we performed SAXS experiments in diluted conditions at 0.25 mg/mL, with 200mM NaCl and 4°C at BM29 BIOSAXS beamline at ESRF (**Figure, 26A**). The GUINIER plot (**Figure, 26B**) at small scattering vector (q) values was linear and yielded an average value of Rg = 5.05 ± 0.56 nm. The extrapolation of intensity at zero angle, $I_0$, as well as the Vc provided a measure of a molecular mass of 67 ± 1.3 kDa, in agreement with the theoretical mass of 67 kDa. The dimensionless Kratky indicated that the protein was globally disordered (**Figure, 26C**).

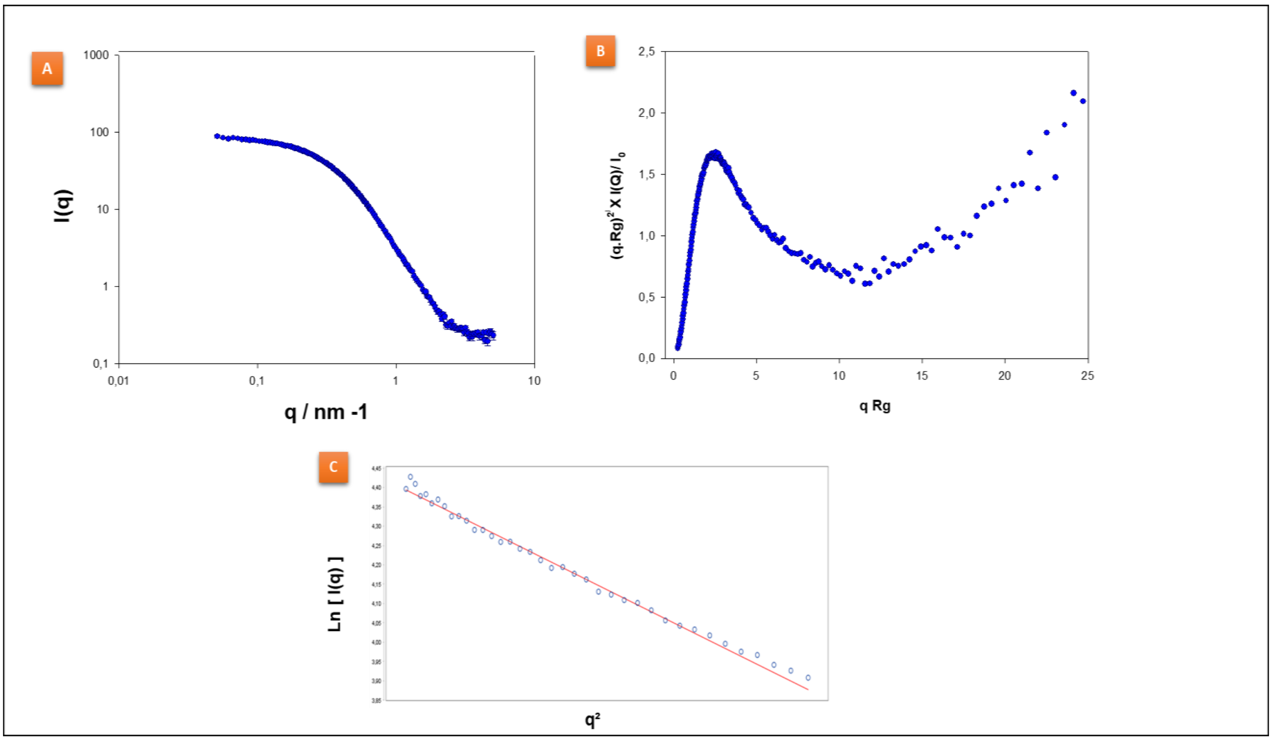

*Figure 26.* ***(A)*** *SAXS intensity plot of dimeric phosphoprotein at 0.8mg/mL in 200mM NaCl at 4°C.* ***(B)*** *Dimensionless Kratky plot of scattering data of RABVP.* ***(C)*** *The Guinier plot at small scattering vector (q) values.*

We also performed a sedimentation velocity experiments with RABV P also in diluted conditions (0.25 mg/mL), 200 mM NaCl, at 4°C and 20°C. The analysis shows a single symmetrical peak with continuous distribution of sedimentation coefficient (c(s)) centered on 3.6 S (**Figure, 27B**), which corresponded to the dimer of P confirming the existence of monodisperse species even at 20°C.

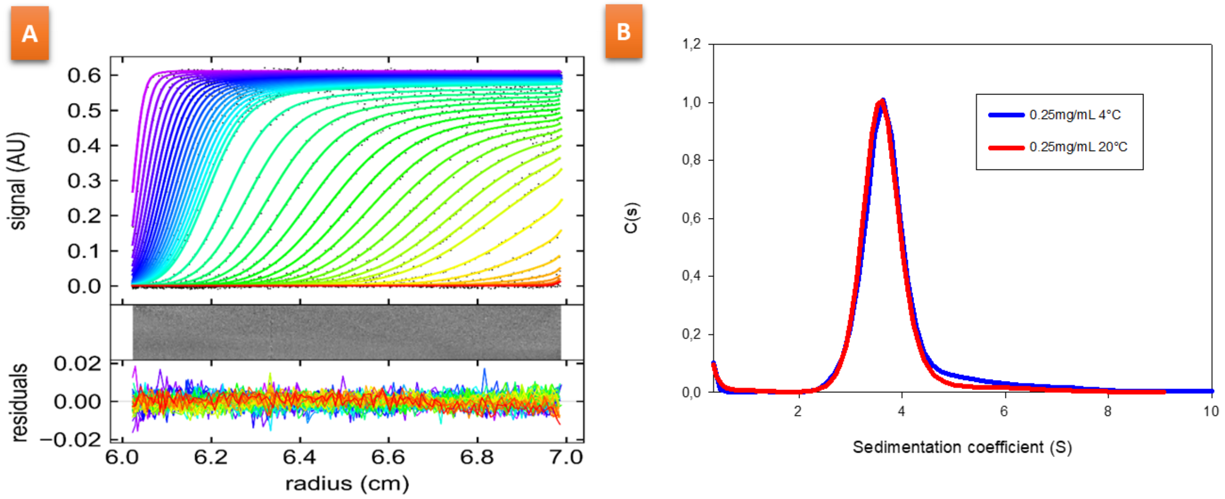

*Figure 27. Sedimentation coefficient distribution calculated by modeling of sedimentation velocity concentration profiles.**(A)** Scans and fitting curves resulting from the analysis with Sedfit software (tpo panel), residuals of the fit (bottom panel)**. (B)**Sedimentation coefficients distribution for RABVP at 0.25mg/mL at 4℃ and 20℃. The sedimentation coefficient at the maximum of the distribution is 3,6S*

We were able to determine the distribution of species and sorted the ions based on their mass-to-charge ratio, using electrospray mass spectrometry, the result show the presence of one dominant species of 34,056 +/- 1-2Da (**Figure, 28**), which correspond to the expected average mass of 34187.39 Da. The difference correspond to a methionine loss.

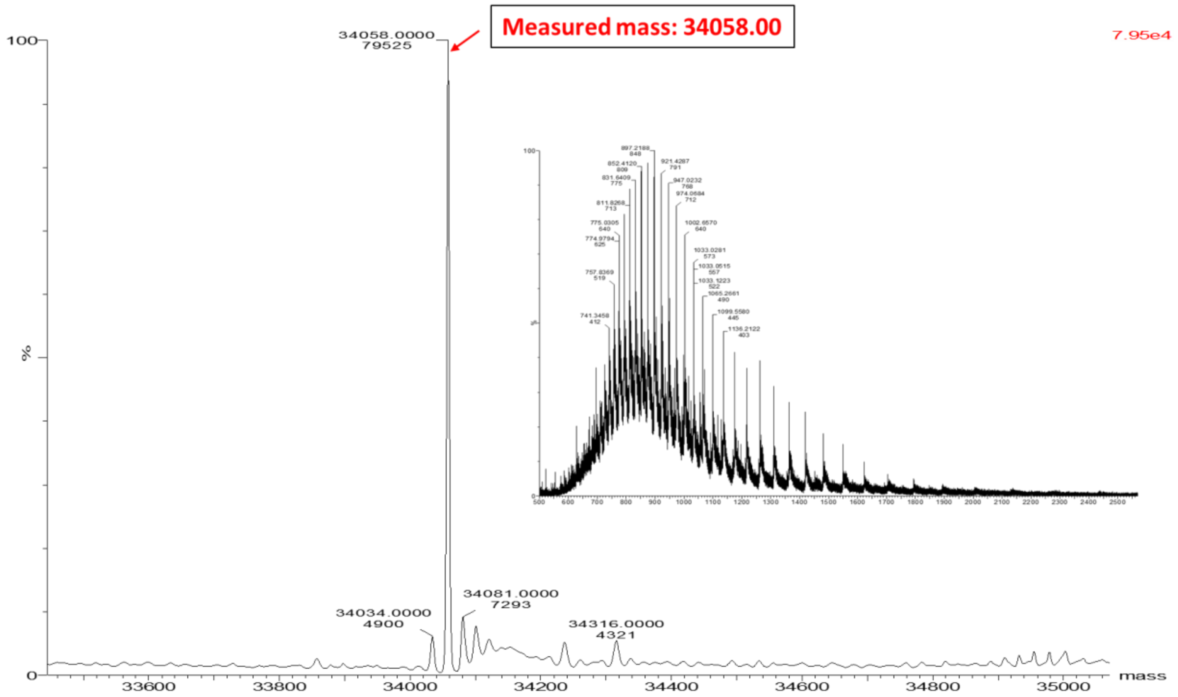

*Figure 28. Determination of the molecular mass of RV P by quadrupole mass spectrometry. The graph shows the deconvolution of the electrospray ionization mass spectrum. The calculated average is indicated by the red arrow*

## • ***Expression and purification of RABV PΔ91-131 ($P_{\Delta MD}$)***

Following the same steps as for full-length phosphoprotein, we produced a P construct where the dimerization domain was deleted. Thus, we expected the protein to be monomeric mass (29kDa) (**Figure, 29A**). After concentration, the gel filtration showed a first small pic mass (**Figure, 29B)** which might correspond to a bigger form of P, the protein having a cysteine in C terminal, it is possible that it has formed disulfide bridges. The second Pic corresponded to the protein of interest, SDS-PAGE showed a band of $P_{\Delta MD}$ that matched the expected molecular mass (**Figure, 29C**), and the weight-averaged molecular mass (MM) calculated by MALLS, 29 ± 1.2 was in agreement with the expected monomer mass (**Figure, 29D**). The concentration indicated by MALLS was 23mg/mL. -

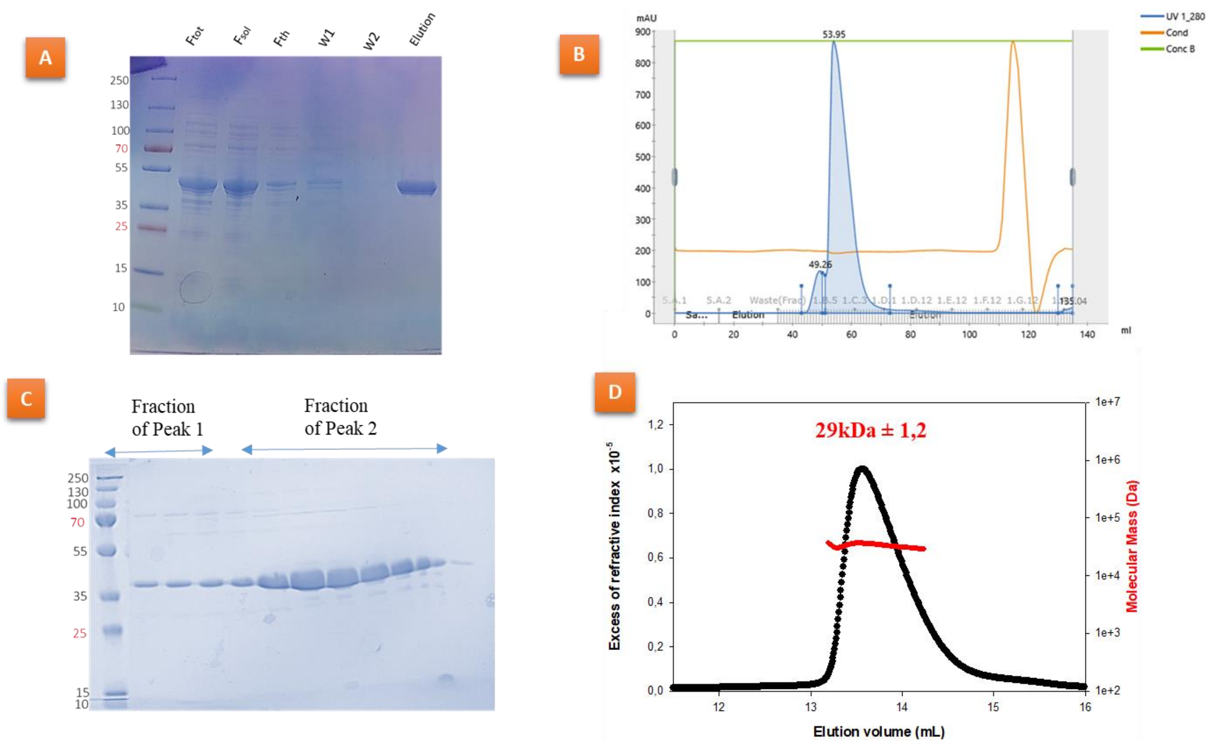

*Figure 29.* ***(A)*** *The purity of PΔ91-131 checked with 15% SDS PAGE visualized with comassie blue.* ***(B)*** *SEC-MALLS analysis of PΔ91-131, the red dots show the MM calculated from the laser light scattering.* ***(C)*** *The chromatogram of size exclusion chromatography (SEC) of the PΔ91-131. (****D****) Analysis of the fractions from SEC by 15% SDS-PAGE stained with coomassie blue*

## - ***Labelling of RABV P with a fluorescent probe (FAM)***

In order to follow liquid droplets and make molecular imaging, we took advantage of the presence of two cys residues in the C-terminal domain of the protein, including the terminal residue (C298). We thus labelled RABVP protein with a thiol reactive dye FAM maleimide. After chemical labelling, the protein was purified by SEC. After labelling, the protein became fluorescent and could be seen directly both on SEC and on SDS-PAGE (data not shown).

### • ***Expression and purification of RABV deuterated P ($P_D$)***

$P_D$ was previously produced at the ILL D-lab facility. The purity of the protein preparation was checked by 15% SDS−PAGE, where the $P_D$ appears as band of 40 kDa (**Figure, 30A**). The protein was slightly degraded but was used for our preliminary experiments.

The elution profile of the gel filtration showed two peaks (**Figure, 30B**) and SDS PAGE (15%) revealed that aggregates eluted in peak 1 and the protein in peak 2 (**Figure, 30C**).

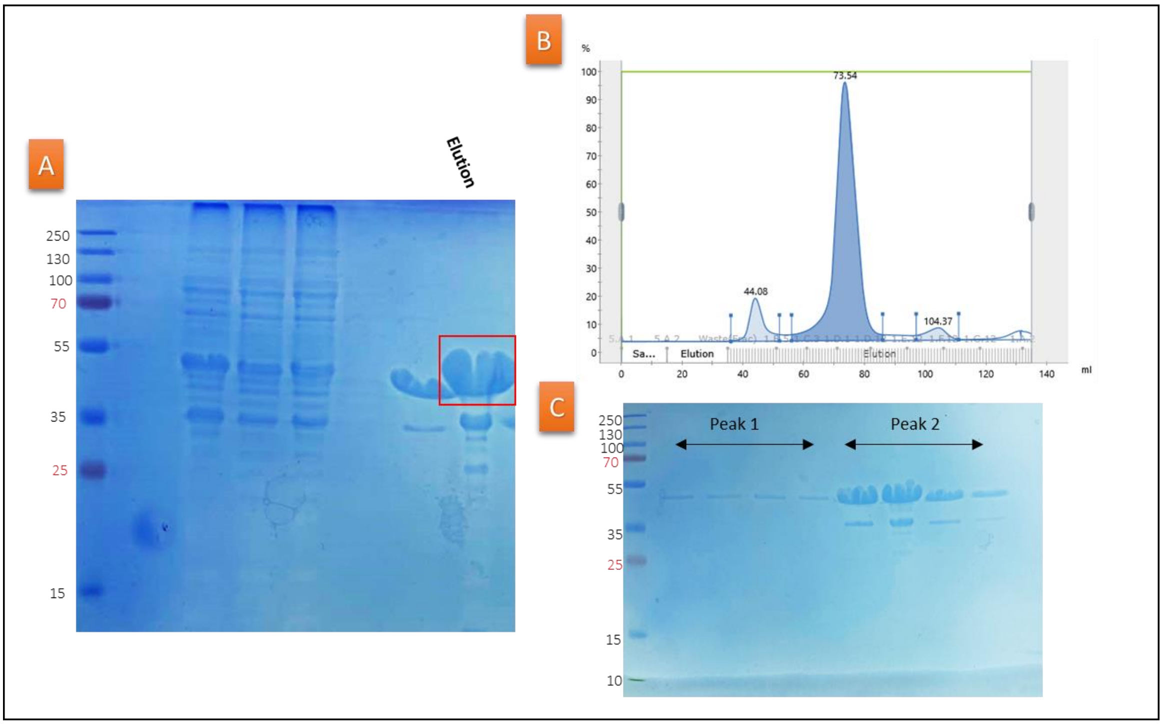

*Figure 30.* ***(A)*** *15% SDS-PAGE of the purification of $P_D$* ***(B)*** *The chromatogram of size exclusion chromatography (SEC) of the $P_D$.* ***(C)*** *Analysis of the fractions from SEC by 15% SDS-PAGE stained with coomassie blue*

- ***Expression and purification of the fusion protein $N_0$-$P_{68}$***

We devised a strategy to generate the complex $N^0$-$P_{68}$ between RNA-free unassembled RABV N protein ($N^0$) and the chaperon module of P, a peptide of 68 AA derived from the N-terminal end of P (**Figure, 31A**).

In the prospect of possibly producing deuterated sample, the $N^0$-$P_{68}$ construct was first expressed using bacterial expression system. However, the amount of protein at the end of the purification was very low (**Figure, 31B**). Furthermore, SDS gel showed that a common contaminant of *E. coli*, called SlyD is present in the elution fraction at 25kDa. The presence of this contaminant would thus require additional purification steps to eliminate, causing additional loss of protein material.

Therefore, we decided to express the construct by using an insect expression system (Hi5 cells), and we purified the fusion protein by a two-step protocol similar to that used for RABV P. The overexpressed fusion protein appeared as band of 70 kDa on SDS PAGE (**Figure, 31C**). After cleavage with the Tobacco Etch Virus (TEV) Protease (a highly specific cysteine protease), the N protein appeared as a band around 58 kDa, whereas $P_{68}$ is too small to be seen on this gel (MM = 5kDa). The sample was then concentrated and analyzed by SEC-MALLS-RI (**Figure, 31D**). The average molecular mass of 55 ± 2 kDa was in agreement with the theoretical mass of 56 kDa.

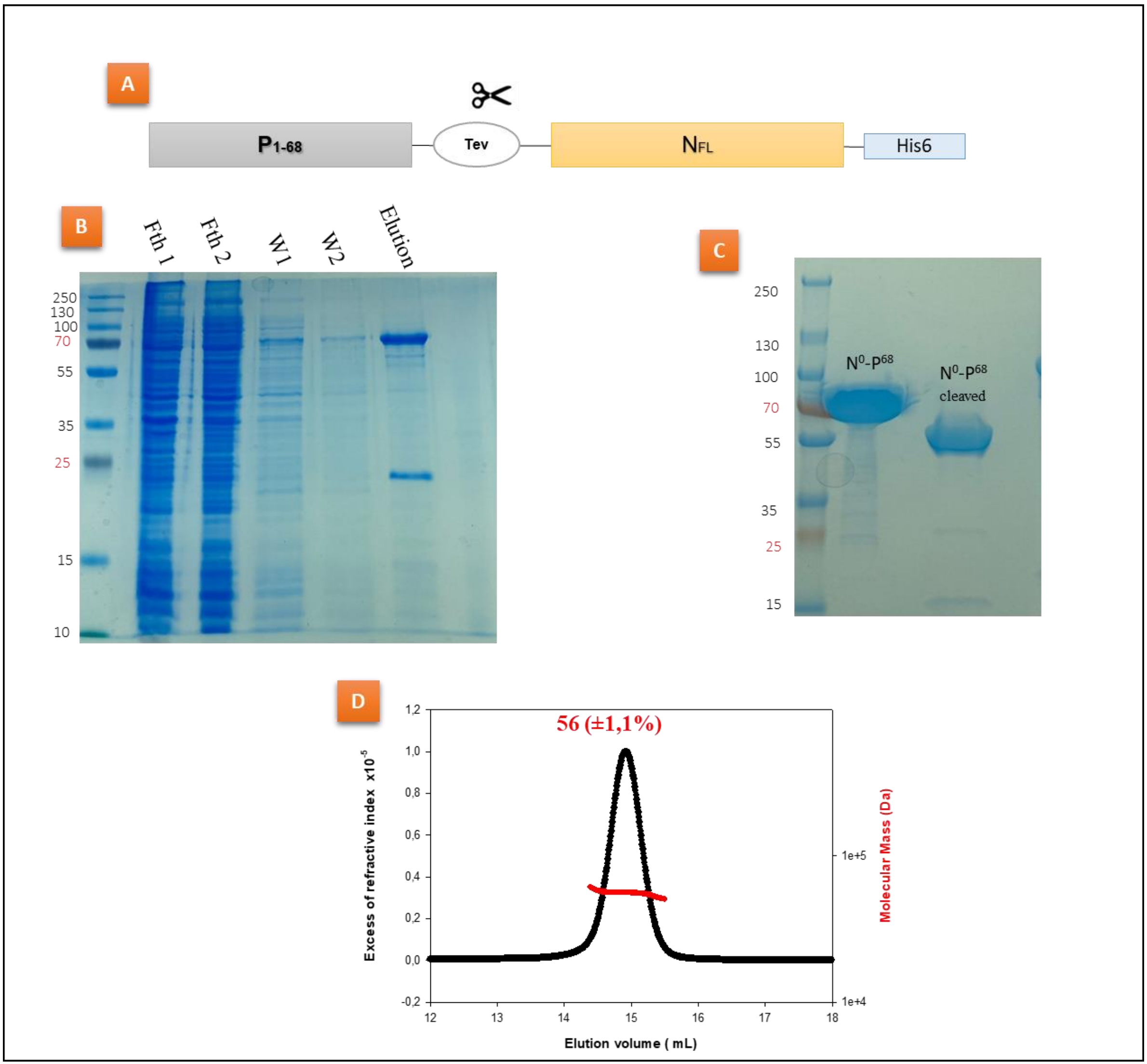

*Figure 31.* ***(A)*** *The schematic construct of the fusion protein $N^0$-$P_{68}$.* ***(B)*** *12% SDS-PAGE of the purification of $N^0$-$P_{68}$ using bacterial system of production. Fth : correspond to flow through and W :correspond to wash* ***(C)*** *12% SDS-PAGE of the purification of $N^0$-$P_{68}$ with and without TEV cleavage, and after cleavage with TEV using bacculovirus insect cells system for the production* ***(C)*** *SEC-MALLS analysis of $N^0$-$P_{68}$, the red dots show the MM calculated from the laser light scattering.*

- ***SAXS analysis of $N^0$-$P^{68}$***

We performed SEC-SAXS experiments with $N^0$-$P_{68}$ at the Swing beamline of the synchrotron SOLEIL in Paris.

The graph showed the chromatographic elution peak as monitored by SAXS intensity with the Rg at the different elution times (**Figure, 32A**). Homogenous Rg under the peak indicated a monodisperse sample and showed the absence of aggregation. We have averaged the points under the peak to realize an intensity plot (**Figure, 32B**). The GUINIER plot (**Figure, 32C**) at small scattering vector (q) values ($q.R_g < 1.3$) is linear at the different times of the chromatogram, and yielded a value of Rg = 3.0 ± 0.2 nm, while the extrapolation of intensity and zero angle, $I_0$ together with the Vc provided a measure of a the molecular mass of 52 ± 4 kDa , in agreement with the theoretical mass of 57 kDa.

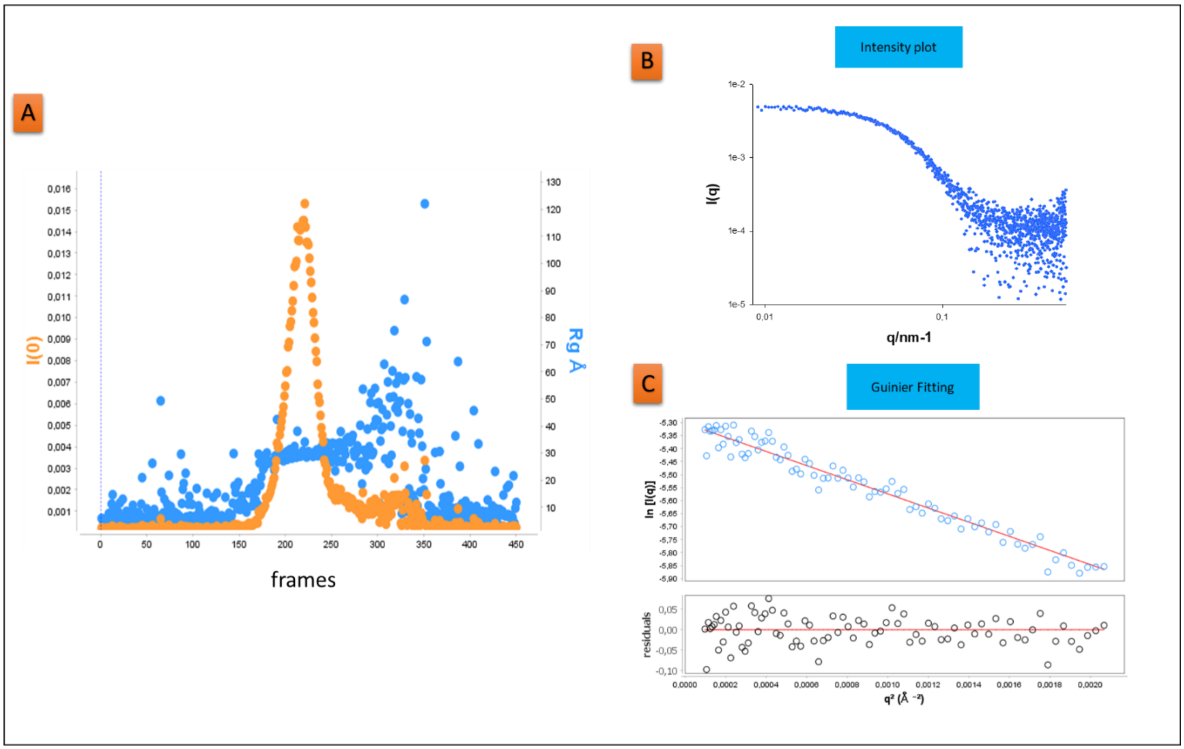

*Figure 32. SAXS analysis of $N_0$-$P_{68}$*

- ***Expression and purification of the fusion protein $N_0$-$P_{68}$-mCherry***

We generated a construction of $N^0$-$P_{68}$ combined with a monomeric red fluorescent protein called mCherry (**Figure, 33A**). $N_0$-$P_{68}$–mCherry was expressed using an insect cell expression system, and then purified. The purity of the protein preparation was checked by 12% SDS−PAGE (**Figure, 33B**). the $N_0$-$P_{68}$–mCherry protein appeared as a band around 90 kDa.

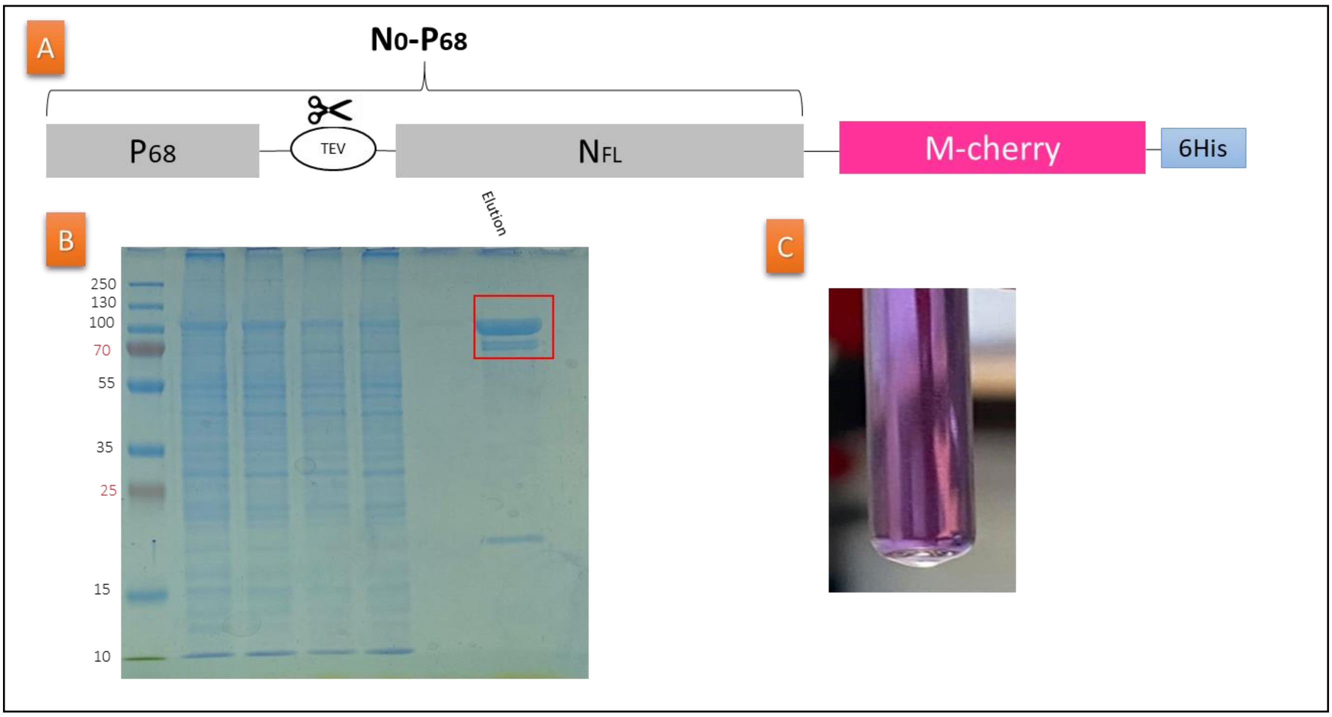

*Figure 33.* ***(A)*** *The schematic construct of the fusion protein N-P68-mCherry.****(B)*** *12% SDS-PAGE of the purification of N-P68-mCherry.* ***(C)*** *N-$P_{68}$-mCherry tube*

## ***Reconstitution of N-RNA NCs from $N^0$-P68 complex***

Using the purified and cleaved $N^0$-$P_{68}$ complex, we performed assays of NCs reconstitution, by mixing the complex with different types of RNAs of different length. We tested the formation of NCs by negative staining electron microscopy (ISBG EM platform). We could observe the formation of rings (**Figure, 34**), when we added a small RNA of 19 nucleotides, and possibly longer NC.

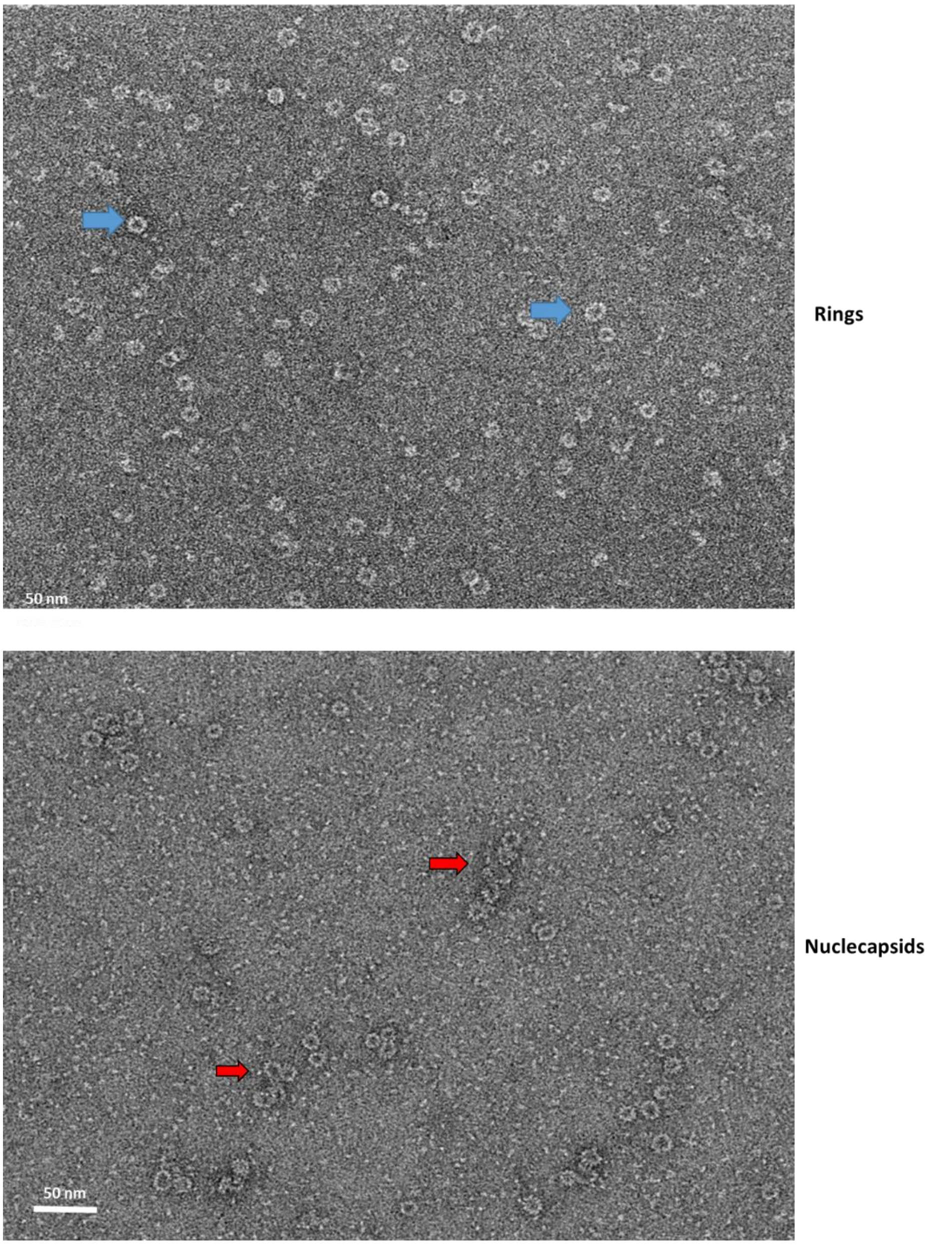

*Figure 34.Electron micrograph of N-RNA rings and NCs reconstituted from* $N_0$*-P*

- ***CONCLUSION***

On the basis of our initial hypothesis, we have been able to produce and purify P and $N^0$-$P_{68}$ complex and their different constructions. Analysis using instruments like SAXS, MALLS or electron microscopy, allow us to verify the monodispersity and purity of the proteins and proves that N binds to RNA.

## (b) RABV liquid-liquid phase separation enabling

### i. Phosphoprotein assembles into soluble complexes and induce LLPS

The following results will be presented in the form of an article that we plan to submit for publication in the next few weeks. Then, I will present additional results obtained during the thesis, which either were not conclusive, or confirmed the results presented in the article.

In this article, we show that RABV P alone undergoes a thermoresponsive liquid-liquid phase separation with a lower critical solution temperature (LCST). We have been able to define the optimal LLPS conditions. The process is temperature/ionic strength/ protein concentration dependent, and remains reversible. By contrast, with $P_{\Delta MD}$ in similar conditions, no LLPS was observed.

Using different biophysical methods, including analytical ultracentrifugation, small-angle X-ray scattering (SAXS) and Ultra small angle scattering (USAXS), we showed the effect of different parameters of RABV phosphoprotein and characterized the protein in both the diluted phase and in the coacervate.

# Rabies virus phosphoprotein induces liquid-liquid phase separation by self-coacervation

Fella Bouchama[1] Jean-Marie Bourhis[1], Caroline Mas[1], Christine Ebel[1], Sylvain Prevost[2], Thomas Zemb[3], Marc Jamin[1]

[1]Université Grenoble Alpes, CNRS, CEA, Institut de Biologie Structurale, 38000, Grenoble, France
[2] Institut Laue Langevin, Grenoble, France
[3] Institut des Sciences Séparatives Marcoule, CEA-Marcoule, France

**Running title:** Coacervation of rabies virus P induces liquid-liquid phase separation

* **Corresponding author:** Institut de Biologie Structurale (IBS), UMR 5075 CEA-CNRS-UJF, 71, Avenue des Martyrs, 38044 Grenoble, France

E-mail : marc.jamin@ibs.fr, Phone: + 33 4 76 20 94 62, Fax : + 33 4 76 20 94 00

# Abstract

The rabies virus (RABV) phosphoprotein (P) is an essential component of the RNA synthesizing machine of the virus and is involved in the creation of membrane-less compartments in the cytoplasm of infected cells, where transcription, replication and encapsidation of the viral genome occur. RABV P protein is an intrinsically disordered protein forming star-shaped dimers with two long, flexible and negatively charged N-terminal arms and two shorter C-terminal arms terminated by an electrostatically polarized, globular domain.

Here, we report that RABV P alone undergoes a thermoresponsive liquid-liquid phase separation with a lower critical solution temperature (LCST). We found that the phase separation is controlled by ionic strength and protein concentration but is not following a simple binary model, and we established phase diagrams. Using various biophysical methods, including analytical ultracentrifugation and small-angle X-ray scattering (SAXS), we discovered that already in the one-phase region of the phase diagram, RABV P dimers reversibly assembles into soluble and more compact complexes. Above the critical temperature, the system remained arrested in a state in which droplets of protein self-coacervate are suspended in a diluted phase. Using ultra-small-angle X-ray scattering (USAXS), we characterized the protein in both the diluted phase and in the coacervate. We discuss a possible model in which intra- and intermolecular interactions controls the coacervations.

# Introduction

Liquid-liquid phase separation (LLPS) induced by proteins and/or nucleic acids has recently re-emerged as a key mechanism for the formation of membrane-less cellular organelles (MLOs) and thereby for the control of many normal or pathogenic cellular processes ((Brangwynne et al., 2015a); (Hyman et al., 2014)). Some of these membrane-less organelles have been known for a long time, such as the nucleoli, which were discovered in the 1830s, or the Cajal bodies in 1903. Similarly, dense, eosinophilic inclusions, now called Negri's bodies, were discovered in the 1900's in the cytoplasm of neuronal cells of patients who died from rabies (Negri 1904).

Rabies is a neglected zoonotic, incurable brain disease, which despite the availability of efficient vaccine and post-exposure prophylaxis, continues to kill tens of thousands of people every year according to WHO (Dietzschold et al., 2008). Its etiological agent, the rabies virus (RABV), belongs to the family *Rhabdoviridae* and is a prototypic member of the order *Mononegavirales*, which regroups numerous nonsegmented negative-sense RNA viruses including important human pathogens such as measles virus, and mumps virus responsible of children diseases, respiratory syncytial virus, metapneumovirus and parainfluenza viruses responsible of mild to serious respiratory diseases, and some deadly zoonotic viruses such as rabies, Nipah, or Ebola viruses (Kuhn et al., 2020; Pringle, 1997).

All members of the order *Mononegavirales* are enveloped viruses that share similar architectures of their genome and virion. They encode homologous proteins that have similar structure and perform similar functions in the viral replication cycle. In particular, three proteins: the nucleoprotein (N), the phosphoprotein (P) and the large RNA-dependent RNA polymerase (L), assemble into a megadalton ribonucleoprotein complex (RNP) with the viral genomic RNA that constitutes the infectious part of the virus. Once released into the cytoplasm of a suitable host cell, this RNP complex carries out (i) the transcription of the genomic RNA into monocistronic messenger RNAs,(ii) the replication of the genome through the intermediate production of positive-sense antigenomic RNAs, which are then used to make new copies of the genome, and (iii) the packaging of both genomic and antigenomic RNAs in linear homopolymers of N, named nucleocapsids NCs (Iseni et al., 1998; Ruigrok et al., 2011).

In RABV infected cells, the RNPs are concentrated in Negri's bodies (RABV), which are the active center for viral RNA synthesis (transcription and replication) and NC assembly(Lahaye et al., 2009). Recently, Negri's bodies were shown to be membrane-less liquid compartments, formed by LLPS (Nikolic et al., 2017a). Similar cellular inclusions could be reproduced in cultured cells by co-expressing RABV N and P proteins (Nikolic et al., 2017a) and liquid-liquid phase separation could be induced in solution by the RABV P protein in the presence of 5% PEG 8000 (Nevers et al., 2022)

RABV phosphoprotein is an essential multi-functional component of the RNA synthesizing machine with a modular architecture (Gerard et al., 2007, 2009) (Gerard et al. 2007, 2009) (Jespersen et al., 2019) . It acts both as a cofactor of the L polymerase (Horwitz et al., 2020) and as a chaperone of unassembled nucleoprotein ($N^0$) (Gérard et al., 2022), but also hijacks cellular components and counteracts the host's antiviral responses (El Asmi et al., 2018). RABV P forms dimers (Gerard et al. 2007), where each protomer consists of a long N-terminal intrinsically disordered region ($P_{NTR}$, aa 1-90) and a C-terminal region ($P_{CTR}$) made of two folded domains, the multimerization domain, $P_{MD}$ (aa 91-131) and the C-terminal domain (aa 186-297), $P_{CTD}$, which are connected by a flexible linker (aa 132-185) ((Gerard et al., 2009; Mavrakis et al., 2004) (Ivanov et al., 2010)) (**Figure, 1A**). Globally, RABV $P_{FL}$ has an isoelectric point of 5.4, and thus a RABV P dimer bears about 22 negative net charges at pH 7.5. However, the distribution of charged residues is rather asymmetrical, and thus, each $P_{NTR}$ bears 14 negative net charges (28 per dimer), whereas the dimerization domain is neutral (**Figure, 1A**). Together, the C-terminal linker and C-terminal domain bears about 3 negative net charges (6 per dimer), but the folded C-terminal domain presents a dipolar surface charge distribution, with a negative proximal moiety and a positive distal moiety (**Figure, 1B**). The RABV P dimer appears thus as star with two flexible and negatively charged arms and with two arms ending by a globular, dipolar domain (**Figure, 1C**) (Jespersen et al., 2019).

Here, we discovered that RABV P alone induces liquid-liquid phase separation in aqueous solutions at pH 7.5 in the absence of crowding agent. We investigated the dependence on temperature, protein concentration and ionic strength.

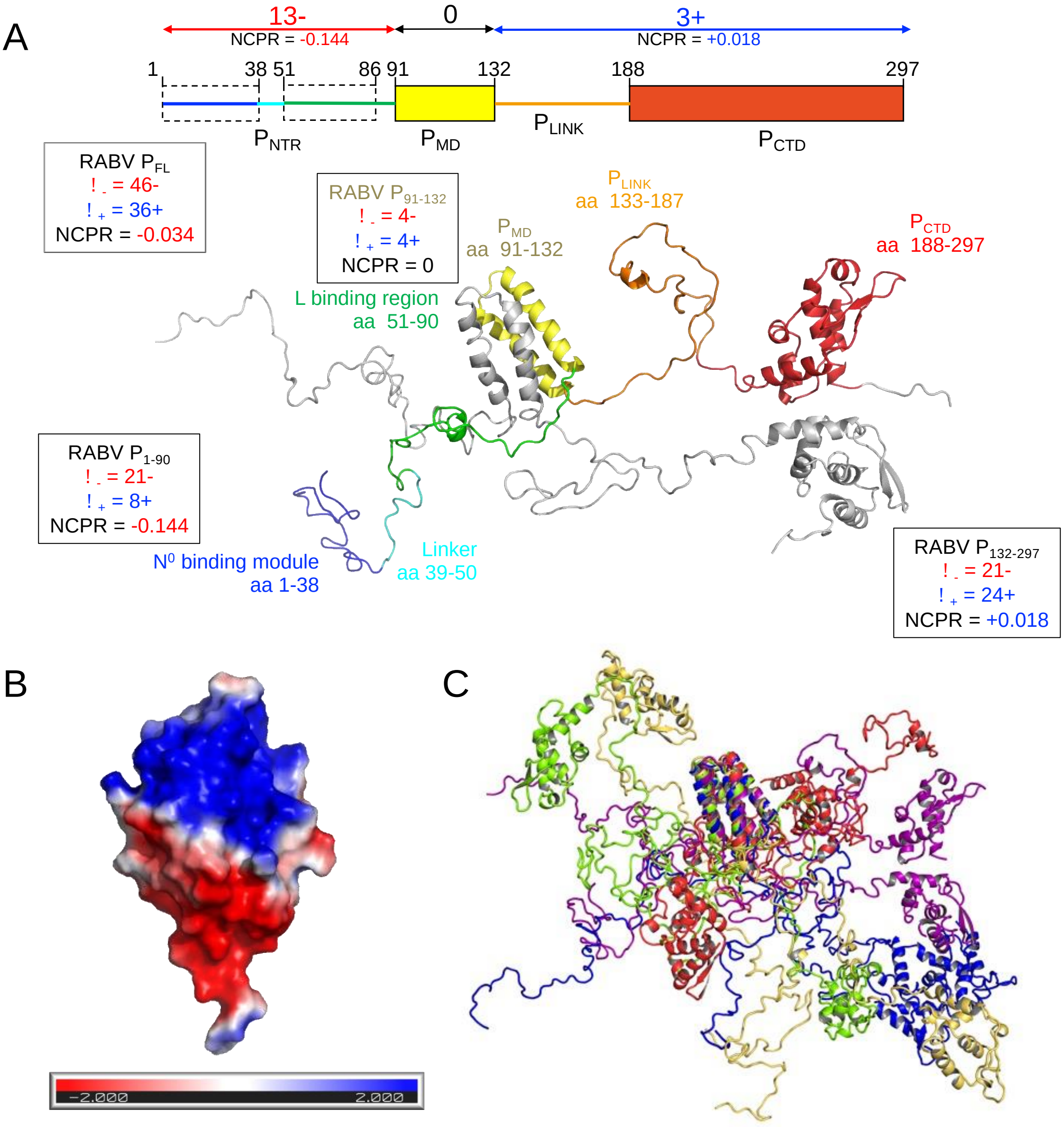

**Figure 0. Structural description of rabies virus phosphoprotein (RABV P). (A)** Schematic representation of the protein and cartoon representation of a dimer. The upper part of the Figure shows a schematic representation of the protein, with boxes showing folded domains, dashed boxes showing known MoREs (i.e. regions that are disordered in isolation but folds or adopts a rigid conformation upon binding to a partner) and the lines show intrinsically disordered regions. The lower part shows a cartoon model of one possible conformer of a RABV P dimer including the crystal structures of the dimerization domain and C-terminal domain. One chain is colored as in the scheme above, with $P_{MD}$ in yellow and $P_{CTD}$ in red. The number of charges and net charge per residues (NCPR) are shown for different segments of the protein inside boxes. **(B)** Electrostatic surface potential of the C-terminal domain showing the bipolar distribution of negative charges (in red) and positive charges (in blue). **(C)** Ensemble model of RABV P taken from Jespersen et al. (2019). The 5 conformers of RABV P were selected to collectively reproduced the SAXS curve and are aligned on their dimerization domain.

# Results

## Full-length RABV P induces reversible thermoresponsive liquid-liquid phase separation with a lower critical solution temperature (LCST)

We expressed the RABV phosphoprotein ($P_{FL}$) in *E. coli*. We purified the protein by successive affinity chromatography and size exclusion chromatography as previously described(Gerard et al. 2007, 2009). We used electrospray mass spectrometry to assess the presence of post-translational modifications in $P_{FL}$. We measured an average molecular mass of 34,056.0 ± 1 Da in perfect agreement with the calculated average molecular mass for a full-length protein lacking its N-terminal methionine (34,187.4603 – 131.1986 (Met) = 34,056.2617 Da). This modification was expected as the penultimate N-terminal residue is a serine, which is known to lead to a high degree of methionine excision in *E. coli* (Hirel et al., 1989).

We discovered that at protein concentration above 1 $mg.mL^{-1}$ (e.g. 4 $mg.mL^{-1}$ - 60 μM) in 20 mM Tris/HCl buffer at pH 7.5 (1 mM TCEP) and intermediate NaCl concentration ranging between 90 and 150 mM NaCl, RABV $P_{FL}$ induced reversible liquid-liquid phase separation in a temperature controlled process (**inset in Figure, 2A**). In these conditions at low temperature (5°C), $P_{FL}$ solutions were clear and homogenous, but upon rising temperature above a threshold temperature, the solutions became opalescent. To monitor the onset of light scattering at the threshold temperature, called $T_{cloud}$, we placed the solution in an absorbance spectrometer at 5°C and slowly increased the temperature, while measuring the optical density at 350 nm at regular temperature intervals (**Figure, 2A**). The onset of phase separation into two phases was marked by an increases in optical density caused by extensive multiple scattering of the incident beam. Using bright field microscopy, we observed the presence of spherical micrometer-size droplets (**Figure, 2B**), which randomly moved in solution and coalesced into larger droplets over time, supporting their liquid character. As long as the temperature was kept below 30°C, the solutions became clear again by decreasing the temperature below the threshold temperature, and the droplets disappeared (**Figure, 2B**), showing that the unmixing was fully reversible in these conditions. However, if we raised temperature above 30°C, protein aggregation occurred and the cloudiness of the solution could not be fully reversed by decreasing the temperature. By repeating this experiment with FAM-labeled P protein, we observed enhanced fluorescence in the droplets over the solution background, confirming that the P protein concentrated inside the liquid droplets (**Figure, 2C**).

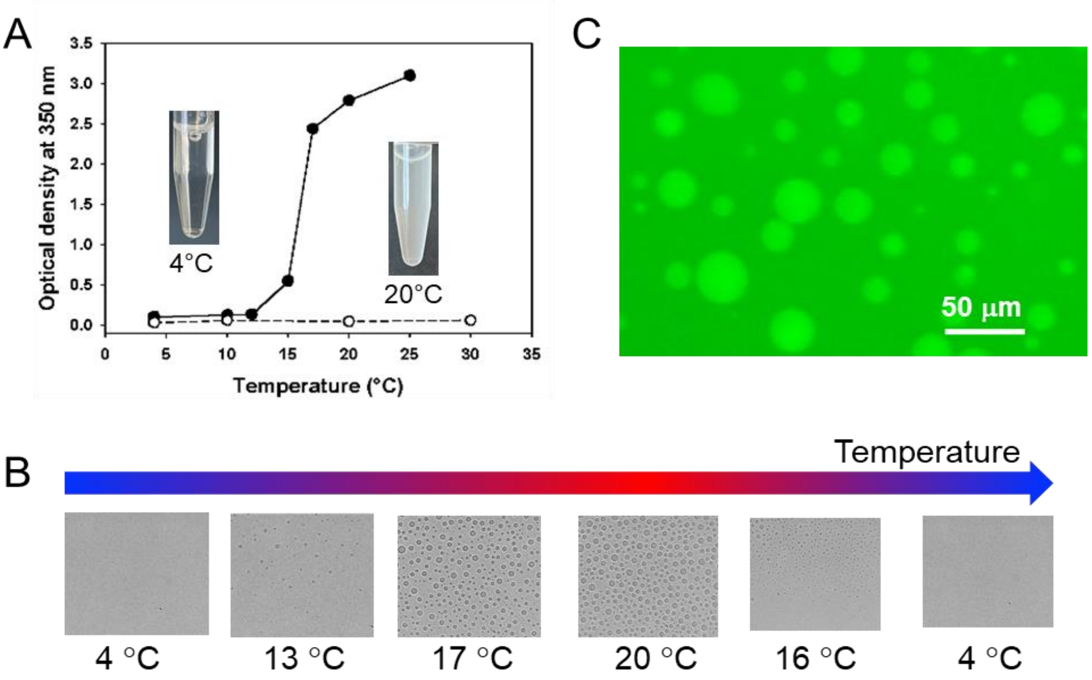

**Figure, 2. Full-length RABV P induces reversible thermoresponsive liquid-liquid phase separation with a lower critical solution temperature (LCST). (A)** Temperature dependence of the optical density at 350 nm of RABV P upon heating. The sample RABV P at 4 mg.mL$^{-1}$ was prepared in 20 mM Tris/HCl at pH.5 containing 120 mM NaCl (ionic strength = 150 mM) at 4°C and the optical density at 350 mM was measured upon heating. The close symbols are for full-length RABV P and the open symbols are for $P_{\Delta MD}$. **(B)** Appearance of micrometer-size droplets observed by bright-field microscopy upon heating and their disappearance observed upon cooling the solution. **(C)** Liquid droplets formed by FAM-labeled RABV P observed by fluorescence microscopy .

We also expressed in *E. coli* and purified by a similar protocol a fragment lacking the dimerization domain (aa 93-133, $P_{\Delta MD}$). By contrast, with $P_{\Delta 93-133}$ in similar conditions, no increase in light scattering could be observed when temperature was increased (**Figure, 1A**), indicating the absence of unmixing and confirming that the dimerization domain was essential for inducing the liquid-liquid phase separation (Nevers et al., 2022; Nikolic et al., 2017a).

In conclusion, RABV P is a thermosensitive protein that induces reversible LLPS above a critical temperature, the phase behavior in dependent on charge screening by dissolved salts and the dimeric state of the protein appeared essential for this process.

### In its reference state, RABV P is a dimer with long intrinsically disordered regions

To further investigate the mechanism of LLPS induced by RABV P protein, we defined reference conditions: 20 mM Tris/HCl buffer at pH 7.5 containing 200 mM NaCl and 0.5 mM TCEP, in which Debye-Hückel screening of charges is effective (Robert J. Silbey, 2004) and we characterized the state of the protein in these conditions. We estimated the ionic strength of this solution at 210 mM using conductance measurements and a calibration with NaCl solutions of varying concentrations.

We showed that in these conditions at low temperature (5°C) and low protein concentration (lower than 1 mg.mL$^{-1}$ – 15 μM), $P_{FL}$ eluted from a SEC column as single peak. Its molecular mass determined from static light scattering and refractometry measurements (SEC-MALLS) was constant throughout the chromatographic peak with $MM/M_n$ ratio (where MM and $M_n$ are the weight average and number-average molecular masses, respectively) of 1.001, indicating a monodisperse species (**Figures, 3A**). The MM values of 65 ± 2 kDa was in agreement with the theoretical molecular mass for dimers (68.4 kDa), as previously shown (Gerard et al. 2007, 2009) (**Figures, 3A**). By using dynamic light scattering, we observed a single species with an hydrodynamic radius of 5.6 ± 0.2 nm, also in agreement with previous results (Gerard et al. 2007) (**Figures, 3B**). We recorded SAXS curves for scattering vector (q) values ranging from 0.05 to 5.0 nm$^{-1}$ over a concentration range of 0.25 to 0.80 mg.mL$^{-1}$ (**Figure, 3C**). The Guinier plots at low q values ($q.R_g < 1.3$) were linear and showed no interparticle interactions and no dependence on protein concentration (**Figure, 3C, inset**). We determined a $R_g$ value of 5.0 ± 0.1 nm in agreement with previous measurements (Gerard et al. 2007; Jespersen et al. 2019), while the dimensionless Kratky indicated that the protein was globally disordered (**Figure, 3D**). An analysis of the power law decay of the scattering intensity showed that RABV P behave as a Gaussian chain with an fractal dimensions ν of 0.39 ($R_g$ = 4.9 nm, $I_0$ = 42.5), slightly lower than that expected for an ideal chain in a theta solvent (0.50) (**Figure, 2C**). Finally, we characterized RABV $P_{FL}$ by sedimentation velocity at a concentration of 0.80 mg.mL$^{-1}$ (**Figure, 3E**). We did not detect the presence of large species, and we calculated the continuous sedimentation distribution (*c*(*s*) versus *s*) by using numerical solutions of the Lamm equation to fit the boundaries (**Figure, 3F**). We obtained a values of 1.65 for the translational friction ratio (*f*/*f*0) and a sedimentation coefficient distribution centered on a $s_{20,w}$ value of 3.6 S that is in agreement with the value of 3.5 ± 0.1 S previously found for dimeric RABV P (Gerard et al. 2007).

Additionally, we measured an MM value of 29 ± 1 kDa for $P_{\Delta MD}$ by SEC-MALLS in agreement with the theoretical molecular mass for the monomer (29.4 Da) as previously shown (Gerard et al. 2009) (**Figure,s 3A**)

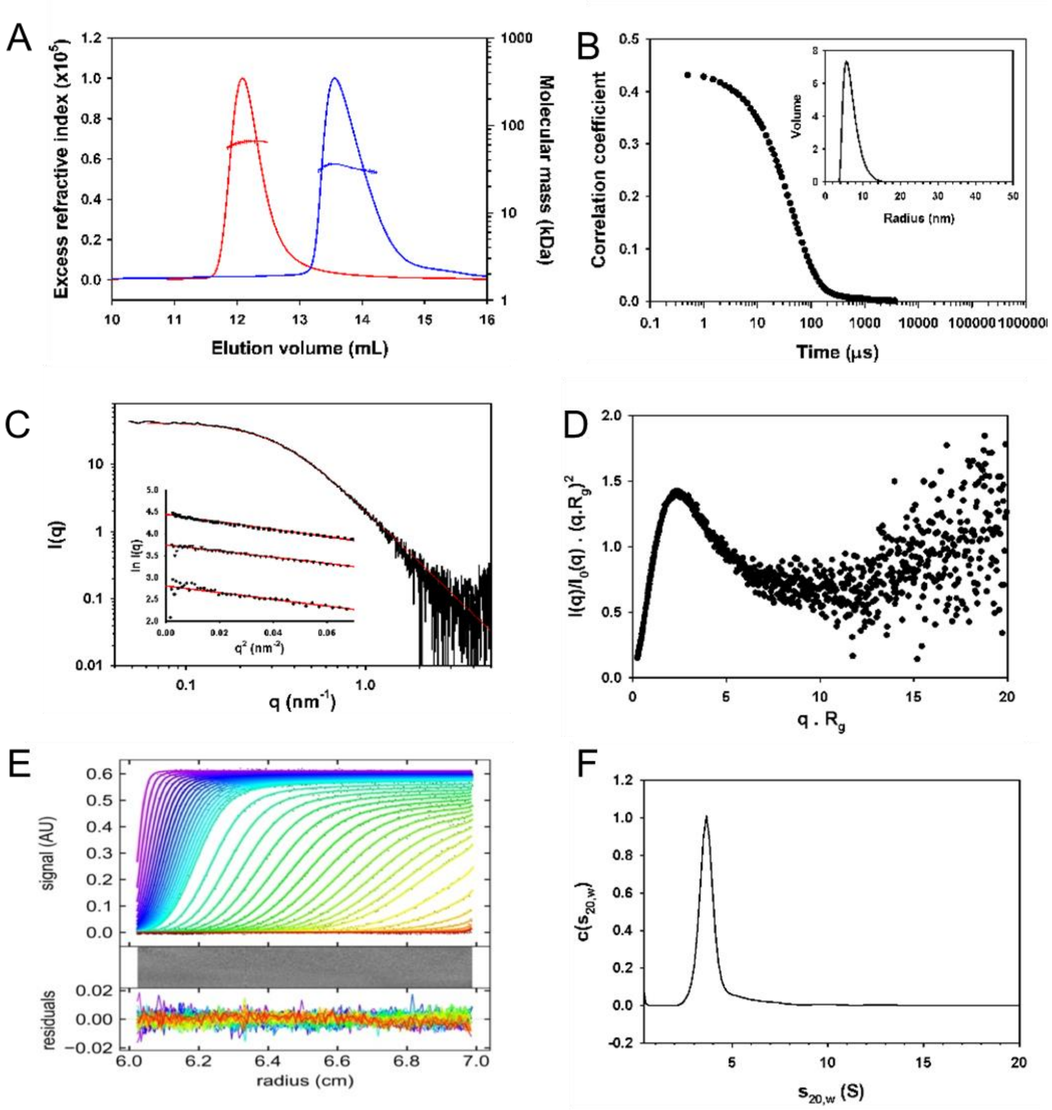

**Figure 3. RABV P forms dimers with long intrinsically disordered regions.** All experiments were performed in 20 mM Tris/HCl pH 7.5 buffer containing 200 mM NaCl. **(A)** SEC-MALLS analysis of RABV P and RABV $P_{\Delta MD}$. The lines show the chromatograms monitored by differential refractive index measurements. The crosses indicate the molecular mass across each elution peak calculated from static light scattering and refractive index, and the numbers indicate the weight-averaged molecular mass (kDa) with standard deviations (the molecular mass calculated from the aa sequence are 68.4 kDa for $P_{FL}$ and 29.4 Da for $P_{\Delta MD}$, respectively). **(B)** DLS analysis of RABV P. The graph shows the correlation plot and the inset shows the distribution in mass. **(C)** SAXS curve . The curve was recorded with a sample at a RABV P concentration of 0.8 mg.mL$^{-1}$. The red line shows the fit with a

Gaussian model. The inset shows the Guinier plot at three RABV P concentrations (0.25, 0.50 and 0.8 mg.mL$^{-1}$). **(D)** Kratky plot. **(E)** Sedimentation velocity. The Figure shows the scans and fitting curves resulting from the analysis with Sedfit software, residuals of the fit (lower panel), for RABV P. The ultracentrifuge was run at 42,000 rpm and 20 °C. Cells were scanned at 280 nm. **(F)** Sedimentation coefficient distribution calculated by modeling of sedimentation velocity concentration profiles.

These results demonstrated that in these reference conditions, we had monodisperse solutions of RABV P dimer characterized by an average Rg of 5.0 ± 0.1 nm and a sedimentation coefficient ($s_{20,w}$) of 3.6 S.

## LLPS induced by RABV P depends on protein and salt concentrations

At a given ionic strength, we found that the onset of light scattering occurred at different temperatures depending on protein concentration. At an ionic strength of 130mM (20mM tris/HCl buffer at pH 7.5 containing 120 mM NaCl), we observed for example the onset of light scattering at 25°C for a RABV P concentration of 0.8 mg.mL$^{-1}$ and at 14°C for a RABV P concentration of 4.0 mg.mL$^{-1}$ (**Figure, 4A**). To complement these results, we used capillary flow experiments (Stender et al., 2021), and injected samples at three protein concentrations containing 1% FAM-labeled protein for fluorescence monitoring. At low concentration (15 µM = 1.0 mg.mL$^{-1}$), almost no spikes were detected, but at higher concentrations (35 µM = 2.4 mg.mL$^{-1}$), we observed spikes, which indicated the presence of droplets in solution and thus the occurrence of phase separation in these conditions (**Figure, 4B**). We found that the number of spikes increased with protein concentration (53 µM = 3.6 mg.mL$^{-1}$), indicating that a larger number of droplets formed. The intensity of the spikes also increased with protein concentration suggesting either the formation of larger droplets or higher concentrations in the dense phase.

We then investigated the dependence of LLPS on ionic strength by varying the salt concentration. At ionic strength below 100 mM (20 mM Tris/HCl buffer at pH 7.5 containing 90 mM NaCl) and at or above 210 mM (20 mM Tris/HCl buffer at pH 7.5 containing 200 to 500mM NaCl), no increase in light scattering was detected upon raising the temperature up to 30°C (**Figure, 4C**), no spikes were observed in capillary flow experiments (**Figure, 4D**) and no droplets were observed by microscopy (**Figure, 4E**). In the intermediate range, at ionic strength between 100 mM and 200 mM, LLPS was induced in a temperature and protein concentration dependent process (**Figure, 4C-E**).

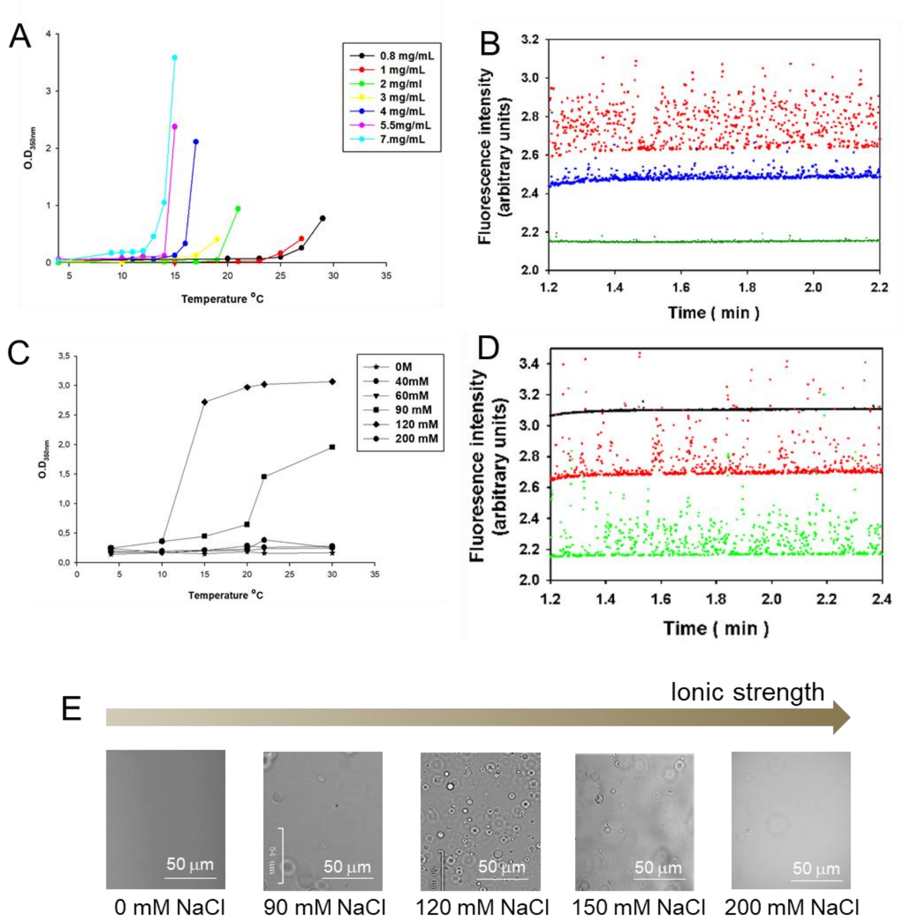

**Figure 4. Dependence of LLPS on protein and salt concentration. (A)** Determination of Tcloud at different RABV P concentrations. **(B)** Capillary flow experiments at different RABV P concentrations. Three samples were injected at 1.0 (in green), 2.4 (in blue) and 3.6 (in red) mg.mL-1. **(C)** Determination of Tcloud at different ionic strengths. **(D)** Capillary flow experiments at different ionic strengths, 210 (black), 100 (red), 130 (green) mM. (**E**) Bright-field microscopy. Samples at different ionic strengths.

## The concentration of the light phase differs little from that of the dense phase

Plotting the onset temperature, $T_{cloud}$, determined at the different protein concentrations (**Figure, 4A**) provided a coexistence curve (**Figure, 5**). The value of $T_{cloud}$ decreased with increasing RABV P concentration, levelling off near 14°C for protein concentrations above 6 mg.mL$^{-1}$. The coexistence curve defined two separated regions in the phase diagram, one with a single, homogenous phase below the curve and one with two coexisting phases above the curve. In a system, that shows LCST behavior, the left branch of the coexistence curve gives the concentration of the diluted phase, while the right branch gives the concentration of the coexisting dense phase. However, RABV P could not be concentrated above 9.0 mg.mL$^{-1}$ by using a centrifugal filter and a lower critical solution temperature (LCST) could not clearly be determined as the curve reached a plateau.

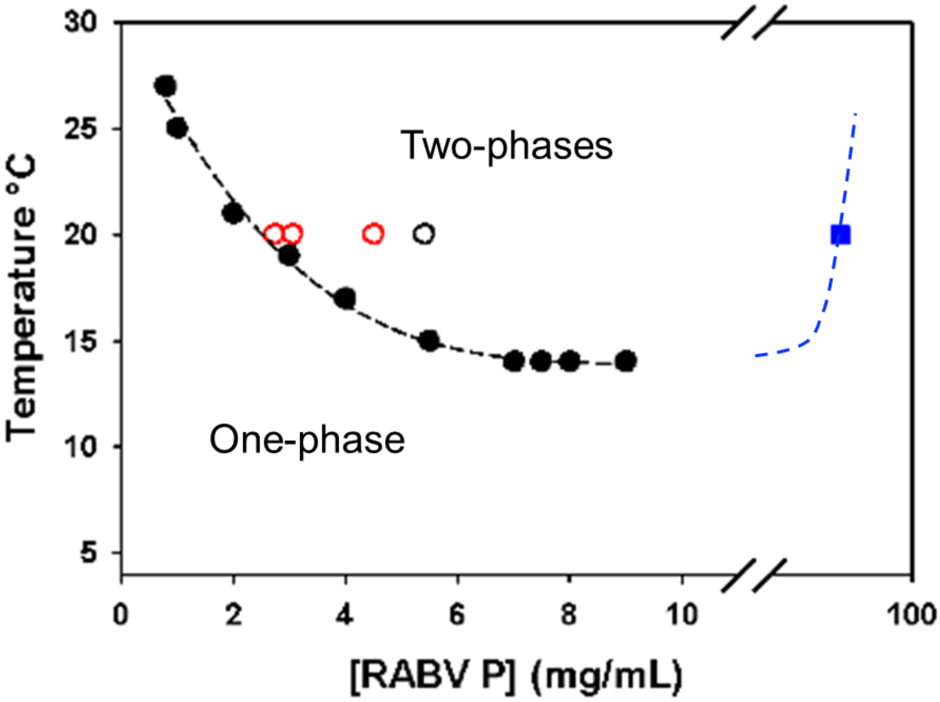

**Figure 5. Phase diagram.** The close black circles were obtained by the measurement of Tcloud at varying RABV P concentrations (taken from Figure, 4A). The red circles show the RABV P concentration measured in the diluted phase obtained at different RABV P concentration in capillary flow experiments (Taken from Figure, 4B). The open black circle shows the concentration of the diluted phase measured after transfer of the solution to 20°C and centrifugation. The blue square shows the estimated concentration in the coacervate from the USAXS experiment (Figure, 9).

To further probe the system, we prepared samples of RABV P at 5°C, at an ionic strength of 210 mM and at protein concentrations above 2 mg.mL$^{-1}$ and transferred the samples at 20°C. The solutions became rapidly opalescent indicating that LLPS occurred, and droplets were visible by light microscopy (**Figure, 2B**), but separation by gravity into two overlaying phases could not be reached after overnight incubation. We therefore performed the separation by centrifugation at 1,000 g after 2 hours or after overnight incubation at 20°C ((Milkovic & Mittag, 2020)). Although a dense phase was visible at the bottom of the tube, its volume was too small to be precisely measured or to take an aliquot. We determined the concentration of the light phase by UV absorbance spectroscopy, and found concentrations clearly larger than those expected from the coexistence curve obtained from T$_{\text{Cloud}}$ measurements (open black circle in **Figure, 5**).

We also measured the concentration of the light phase in identical conditions at different protein concentrations in capillary flow experiments. We confirmed by these measurements that the concentration of the light phase was higher than expected from the coexistence curve. Also, protein concentration in the light phase at 20°C varied with initial protein concentration in contradiction with the behavior observed in simple binary systems (open red circles in **Figure, 5**).

These results demonstrated that the system is more complex than a binary system.

### Full-length RABV P assembles into soluble complexes below the critical temperature

To unravel the mechanism by which RABV P induces LLPS, we investigated the effects of protein concentration, ionic strength and temperature on protein conformation and assembly in the region of the phase diagram below the critical temperature, where a single homogenous phase is present (**Figure, 5**).

First, we recorded SAXS data at low temperature (5°C), ionic strength of 210 mM and at different protein concentrations (**Figure, 6A**). At concentrations below 1 mg.mL$^{-1}$, using samples directly taken from the SEC, RABV P was dimeric with a $R_g$ of 5.0 ± 0.5 nm (**Figure, 5B**). However, at concentrations above 1 mg.mL$^{-1}$ the molecular mass calculated from intensity at zero angle ($I_0$) and the $R_g$ value increased, indicating that the protein assembled into soluble complexes. Thus, at 3.0 mg.mL$^{-1}$, we obtained an average MM of 170 ± 10 kDa for an $R_g$ of 6.1 ± 0.6 nm. The scattering decay could also be reproduced by considering two Gaussian chain components, one corresponding to the dimeric protein ($R_g = 4.9$ and $\nu = 0.39$) and accounting for 30% of the molecules and one corresponding to larger and more compact complexes ($R_g = 7.0$ and $\nu = 0.28$) and accounting for the remaining 70 % of the molecules (**Figure, 6A**).

These results were complemented by sedimentation velocity experiments. At 5°C, $I = 210$ mM, and protein concentration up to 1 mg.mL$^{-1}$, the continuous sedimentation distribution ($c(s)$ versus $s$) indicated the presence of a single species with a $s_{20,w}$ value centered on 3.6 ± 0.1 S (**Figures,, 3E-F**), but at higher protein concentrations, additional species appeared, confirming the formation a larger soluble complexes (**Figure, 6D**). The additional peaks in the distribution varied in size and no attempt was made at this stage to resolve the size of these complexes. However, at 3.5 and 6.5 mg.mL$^{-1}$ the dimer at 3.6 S accounted for 33% and 25% of the molecules in agreement with the proportion of dimers estimated in similar conditions from SAXS.

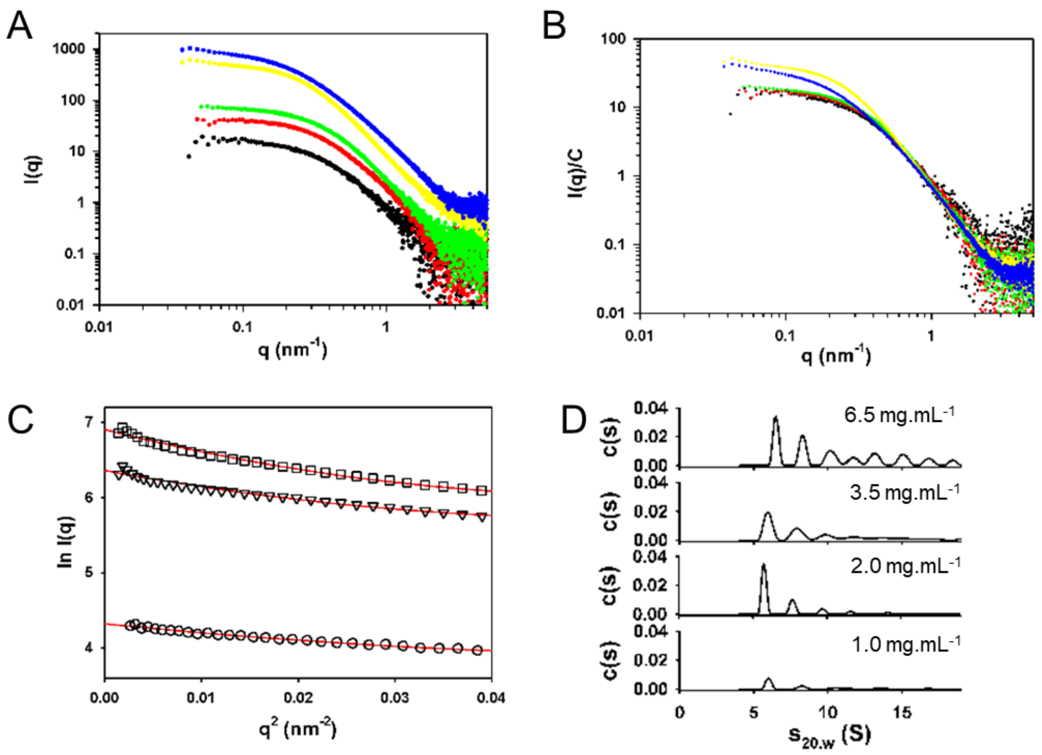

**Figure, 6. Assembly of RABV P as a function of protein concentration below the critical temperature.** All experiments were performed in 20 mM Tris/HCl buffer at pH 7.5 containing 200 mM NaCl (ionic strength of 210 mM) and at 5°C. **(A)** Raw small-angle X-ray scattering data at different protein concentrations. RABV P concentrations are 0.25 (in black), 0.50 (in red), 0.80 (in green), 3.0 (in yellow) and 6.0 (in blue) mg.mL$^{-1}$. **(B)** Small-angle X-ray scattering curves normalized for protein concentration. Same color code as in panel A. **(C)** Guinier plot. The plot shows the data at three RABV P concentrations: 0.80 (open circles), 3.0 (open triangles) and 6.0 (open squares) mg.mL$^{-1}$. **(D)** Sedimentation velocity. The data were fitted by fixing the position of the dimer at 3.6 S and only the contributions of larger species are shown.

Second, we recorded SAXS curves at low temperature (5°C), low protein concentration (0.25 mg.mL$^{-1}$) and at ionic strengths varying from 10 mM to 210 mM (**Figure, 7A**). At 210 mM, RABV P is dimeric with a $R_g$ of 5.0 ± 0.1nm, but at lower ionic strengths, the average molecular mass calculated from the scattering intensity at zero angle ($I_0$) increased, indicating that also in these conditions the protein assembled into soluble complexes. A maximum aggregation number was found at $I = 60$ mM (average MM = 604 ±3 kDa and $R_g = 7.4 \pm 0.1$ nm), suggesting that RABV P assembly was controlled by electrostatics. Debye-Hückel screening of surface charges ($I = 210$ mM) prevented intermolecular interactions, while partial screening ( 60 < I <

130 mM) favored intermolecular interactions and induced the assembly (average MM = 188 ± 2 kDa and Rg = 6.3 ± 0.1 nm at I = 130 mM). At the lowest ionic strength (I = 10 mM), stronger electrostatics hindered the interactions (average MM =268± 2kDa and Rg = 6.5 ± 0.1nm) (**Figure, 7A**).

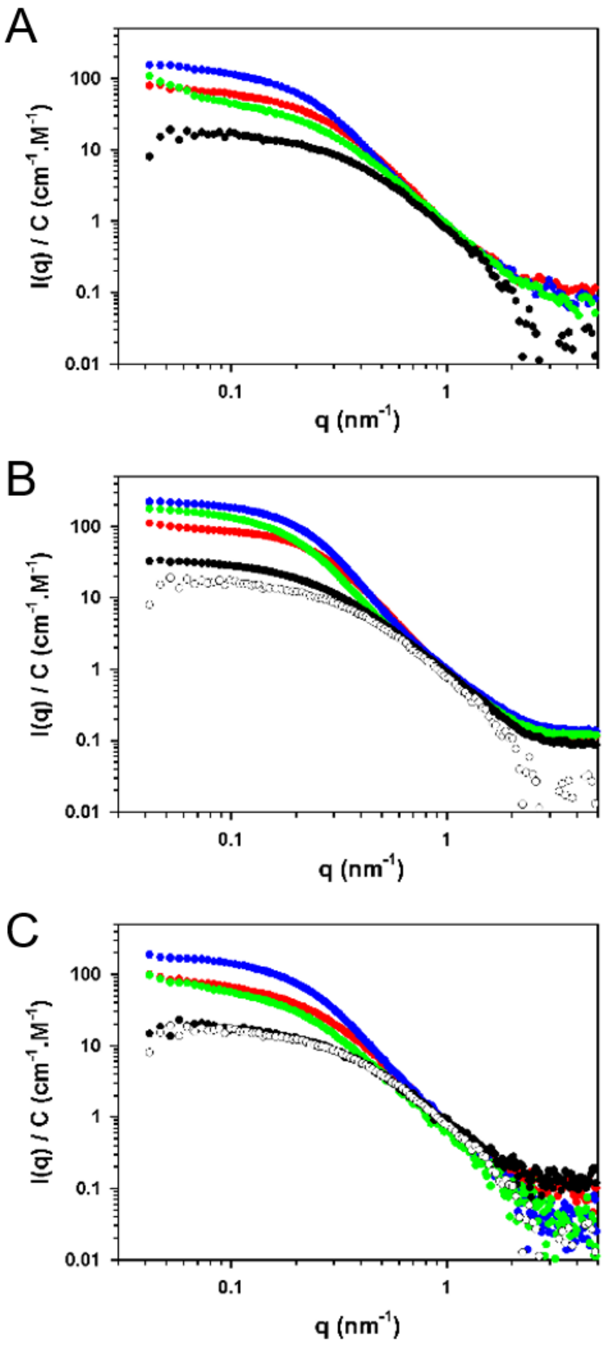

**Figure, 7. Assembly of RABV P as a function of ionic strength below the critical temperature.** All experiments were performed in 20 mM Tris/HCl buffer at pH 7.5 containing varying concentrations of NaCl and at 5°C. **(A)** Initial samples. The RABV P concentration of all samples was 0.25 mg.mL$^{-1}$ and the NaCl concentrations were: 0 mM (in red), 50 mM (in blue), 120 mM (in green) and 200 mM (in black). **(B)** Concentrated samples. The RABV P was concentrated to 2.0 mg.mL$^{-1}$ and the NaCl concentrations are in the same color code as in panel A. The open circles shows the sample at 0.25 mg.mL-1 and at 200 mM as a reference. (C) Diluted samples. The samples were diluted to 0.25 mg.mL-1.

Next, we tested the reversibility of the concentration dependent assembly at 5°C and different ionic strengths. Starting with samples at 0.25 mg.mL$^{-1}$ directly taken from the SEC, we measured SAXS profiles after concentrating the samples to 2.0 mg.mL$^{-1}$ and then after diluting these samples to bring them back to 0.25 mg.mL$^{-1}$ (**Figures, 7B and 7C**). At an ionic strength of 210 mM, concentrating the protein induced an increase in $I_0/C$ of about three fold, accompanied by an increase in Rg from 5.0 ± 0.5 nm to 6.5 ± 1 nm (**Figures, 7B**). However, both changes were fully reversible, and the SAXS curve measured after dilution was superimposed on the initial curve (**Figure, 7C**). At lower ionic strength, the initial $I_0/C$ and $R_g$ values were larger than at 210 mM, and concentrating the samples resulted in further increases in both parameters (**Figure, 7B**). Again these changes were reversible and diluting the samples to their initial concentrations brought these parameters very close to their initial values. At all ionic strengths, the SAXS profiles after dilution were nearly superimposable to the initial profiles demonstrating that the assembly induced by increasing protein concentration was reversible (**Figure, 7C**).

Finally, we measured the effect of temperature at low protein concentration and two different ionic strengths by SAXS (**Figure, 8**). The samples were prepared at 5°C, transferred to 20°C and incubated for 2 hours before SAXS curves were measured. At ionic strength of 210 mM, the protein remained dimeric without changing size ($R_g$ = 5.0 ± 0.5 nm). At ionic strength of 130 mM, RABV P was larger at 5°C ($R_g$ = 6.4 ± 0.5 nm), but no changes were observed after transfer at 20°C. We also complemented these results by performing sedimentation velocity at 20°C and I = 210 mM. At RABV P, concentrations lower than 1 mg.mL$^{-1}$ the sedimentation coefficient remained the same and no evidence of assembly was found. By contrast, at concentrations equal or larger than 1 mg.mL$^{-1}$ additional species appeared, and at 6.5 mg.mL$^{-1}$ phase separation occurred. These results demonstrated that at an ionic strength of 210 mM at which Debye-Hückel screening of charges by diluted salts is almost complete, the assembly observed at the highest concentrations of RABV P was completely reversible. At lower ionic strength, RABV P assembled in soluble complexes that reversibly increased in size with protein concentration but not with temperature.

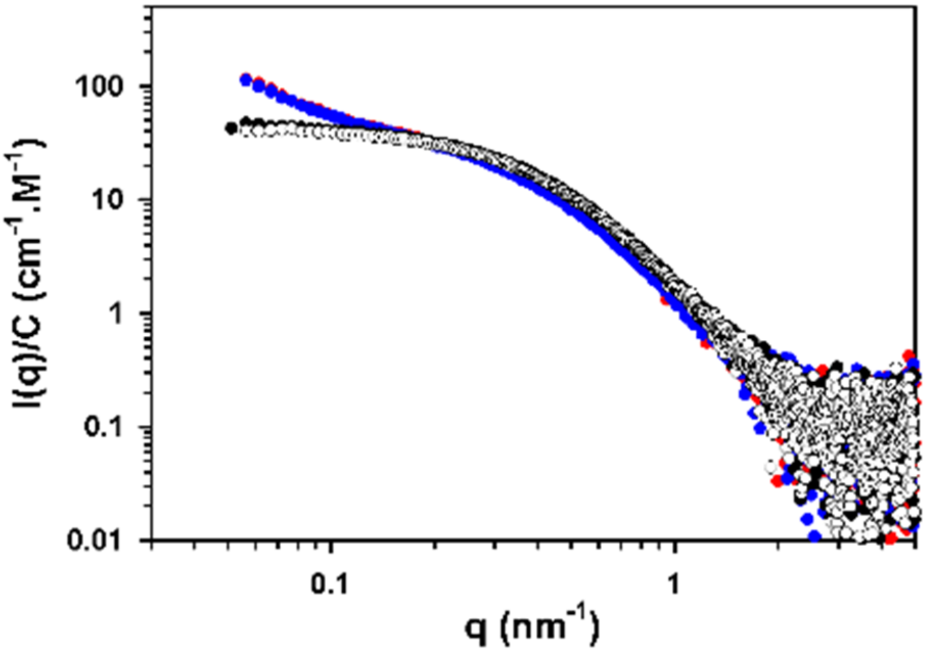

**Figure, 8. Effects of temperature and salt on RABV P assembly.** The experiments were performed in 20 mM Tris/HCl buffer at pH 7.5 containing 120 mM NaCl at 5°C (blue circles) and 20°C (red circles) or 200 mM NaCl at 5°C (open black circles) and 20°C (close black circles).

## Full-length RABV P soluble complexes coalesce into liquid droplets

To investigate the formation of micrometer-size liquid droplets in solution, we prepared a sample of RABV P at 9 mg.mL$^{-1}$ and at an ionic strength of 130 mM. After incubation at 20°C, the solution became opalescent indicating that LLPS occurred. The sample was then loaded in a capillary tube (diameter = 2 mm) and centrifuged at 1,000 g for 20 min. This resulted in the separation into two overlaying phases in the capillary. The upper transparent phase that represented about 95% of the volume was separated by a visible boundary from a lower opalescent phase that represented about 5% of the volume (**inset of Figure, 9**). By absorbance spectroscopy, we determined a RABV P concentration of 4.5 mg.mL$^{-1}$ in the upper phase and calculated a concentration of about 90 mg.mL$^{-1}$ in the lower phase.

We complemented SAXS with ultra-small-angle X-ray scattering (USAXS) by repeating the measurements at two sample-detector distances (1 m and 30 m). We characterized the protein in both the lower and upper phases by vertically moving the capillary in the X-ray beam. **Figure, 9** shows typical USAXS profiles obtained for the upper and lower phases.

In the upper phase, scattering was visible in two different regimes, with two “plateau” regions. Above 0.1 nm$^{-1}$ (red part of the curve), the scattering decay resembles that seen for soluble complexes of RABV P below the critical temperature of the phase diagram (**Figure, 6**). For q values ranging from 0.01 to 0.1 nm$^{-1}$, a plateau region and another scattering decay indicated the presence of additional larger soluble complexes (apparent $R_g$ value = 44.4 ± 2.7). The plateau at low q indicated rather well-defined dimensions. The scattering below 0.01 nm$^{-1}$ was too noisy and is not shown here.

In the lower phase, scattering was also visible in two different regimes with a single plateau region in the intermediate q range (0.05 – 0.2 nm$^{-1}$). Above 0.1 nm$^{-1}$, the shape of the curve follows a similar trend than that of the upper phase, with the scattering decay following a power law in $q^{-2}$, that reported on the incorporation of soluble complexes of RABV P into the coacervate. The curve was shifted up on the intensity scale by 40 fold with regards to the diluted phase. A rough estimation showed that half this increase resulted from the concentration change (4.5 mg.mL$^{-1}$ x 20 = 90 mg.mL$^{-1}$), and the other half likely from the enlargement of the complexes as already observed at lower concentration (**Figure, 6A**). The scattering decay in ultra-small q range (0.002 and 0.02 nm$^{-1}$) followed a power law in $q^{-4}$ reflecting the scattering from a rather smooth surface of micrometer size domains.

In conclusion, these results revealed a complex composition of our samples in both phases; we still find the reference dimeric protein in the liquid phase and the dense probably with different proportions. In both phases, different and larger state of the protein coexists with the dimeric form in the solution. In the dense phase, we find large domains ($q^{-4}$ slope); we interpret these domains as coming from the dilute phase, which could be trapped in the gel dense phase.

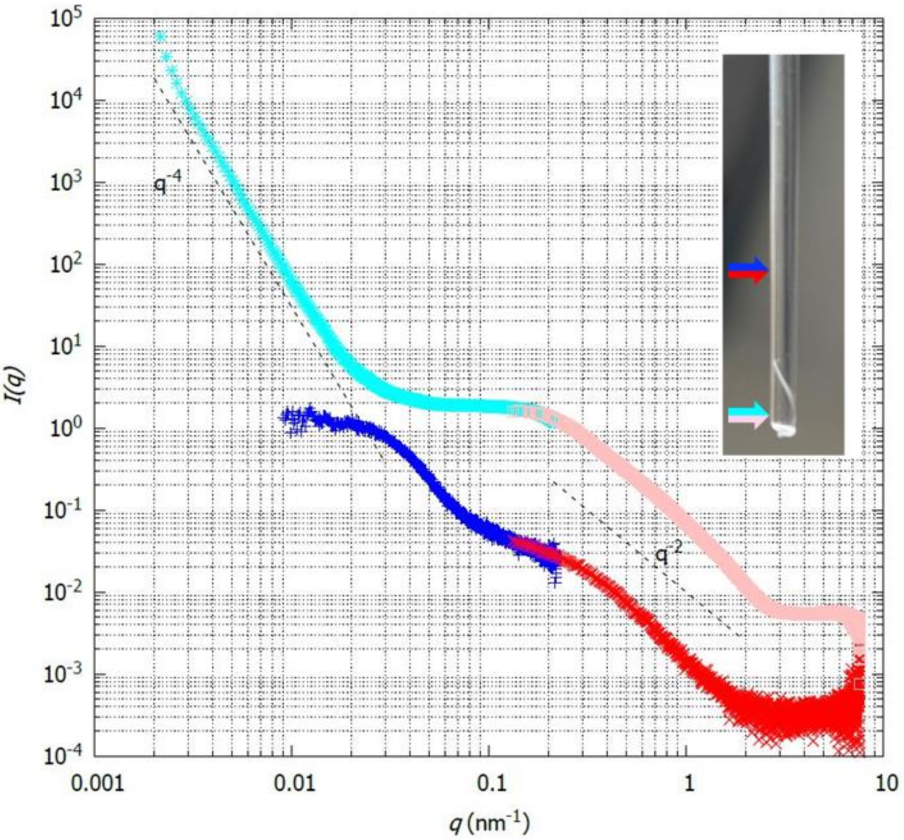

**Figure, 9. Small-angle X-ray scattering of RABV above the critical temperature.** The USAXS and SAXS curves were measured with sample-detector distances of 1 and 30 m. The red/blue curve was measured in the diluted phase at a concentration of 4.5 mg.mL$^{-1}$, whereas the cyan/pink curve was measured in the coacervate at an estimated concentration of 90 mg.mL$^{-1}$.

## References

Alberti, S. (2017). Phase separation in biology. *Current Biology*, *27*, R1097–R1102. https://doi.org/10.1111/pbi.1280

Albertini, A. A. V., Ruigrok, R. W. H., & Blondel, D. (2011). *Rabies Virus Transcription and Replication* (pp. 1–22). https://doi.org/10.1016/B978-0-12-387040-7.00001-9

Albertini, A. A. V., Wernimont, A. K., Muziol, T., Ravelli, R. B. G., Clapier, C. R., Schoehn, G., Weissenhorn, W., & Ruigrok, R. W. H. (2006). Crystal structure of the rabies virus nucleoprotein-RNA complex. *Science*, *313*(5785). https://doi.org/10.1126/science.1125280

Amarasinghe, G. K., Ayllón, M. A., Bào, Y., Basler, C. F., Bavari, S., Blasdell, K. R., Briese, T., Brown, P. A., Bukreyev, A., Balkema-Buschmann, A., Buchholz, U. J., Chabi-Jesus, C., Chandran, K., Chiapponi, C., Crozier, I., de Swart, R. L., Dietzgen, R. G., Dolnik, O., Drexler, J. F., … Kuhn, J. H. (2019). Taxonomy of the order Mononegavirales: update 2019. *Archives of Virology*, *164*(7), 1967–1980. https://doi.org/10.1007/s00705-019-04247-4

Baltimore, D. (1971). Expression of animal virus genomes. *Bacteriological Reviews*, *35*(3), 235–241. https://doi.org/10.1128/MMBR.35.3.235-241.1971

Banani, S. F., Lee, H. O., Hyman, A. A., & Rosen, M. K. (2017). Biomolecular condensates: organizers of cellular biochemistry. *Nature Reviews Molecular Cell Biology*, *18*(5), 285–298. https://doi.org/10.1038/nrm.2017.7

Bates, F. S. (1991). Polymer-Polymer Phase Behavior. *Science*, *251*(4996), 898–905. https://doi.org/10.1126/science.251.4996.898

Baudin, F., Bach, C., Cusack, S., & Ruigrok, R. W. H. (1994). Structure of influenza virus RNP. I. Influenza virus nucleoprotein melts secondary structure in panhandle RNA and exposes the bases to the solvent. *EMBO Journal*, *13*(13). https://doi.org/10.1002/j.1460-2075.1994.tb06614.x

Biamonti, G., & Vourc'h, C. (2010). Nuclear Stress Bodies. *Cold Spring Harbor Perspectives in Biology*, *2*(6), a000695–a000695. https://doi.org/10.1101/cshperspect.a000695

Blondel, D., Maarifi, G., Nisole, S., & Chelbi-Alix, M. (2015). Resistance to Rhabdoviridae Infection and Subversion of Antiviral Responses. *Viruses*, *7*(7), 3675–3702. https://doi.org/10.3390/v7072794

Blondel, D., Regad, T., Poisson, N., Pavie, B., Harper, F., Pandolfi, P. P., de Thé, H., & Chelbi-Alix, M. K. (2002). Rabies virus P and small P products interact directly with PML and reorganize PML nuclear bodies. *Oncogene*, *21*(52), 7957–7970. https://doi.org/10.1038/sj.onc.1205931

Boija, A., Klein, I. A., & Young, R. A. (2021). Biomolecular Condensates and Cancer. *Cancer Cell*, *39*(2), 174–192. https://doi.org/10.1016/j.ccell.2020.12.003

Brangwynne, C. P., Tompa, P., & Pappu, R. V. (2015a). Polymer physics of intracellular phase transitions. *Nature Physics*, *11*(11), 899–904. https://doi.org/10.1038/nphys3532

Brangwynne, C. P., Tompa, P., & Pappu, R. V. (2015b). Polymer physics of intracellular phase transitions. *Nature Physics*, *11*(11). https://doi.org/10.1038/nphys3532

Brown, J. C., Newcomb, W. W., & Wertz, G. W. (2010). Helical Virus Structure: The Case of the Rhabdovirus Bullet. *Viruses*, *2*(4), 995–1001. https://doi.org/10.3390/v2040995

Charlier, C. M., Wu, Y.-J., Allart, S., Malnou, C. E., Schwemmle, M., & Gonzalez-Dunia, D. (2013). Analysis of Borna Disease Virus Trafficking in Live Infected Cells by Using a Virus Encoding a Tetracysteine-Tagged P Protein. *Journal of Virology*, *87*(22). https://doi.org/10.1128/jvi.01127-13

Chelbi-Alix, M. K., Vidy, A., Bougrini, J. El, & Blondel, D. (2006). Rabies Viral Mechanisms to Escape the IFN System: The Viral Protein P Interferes with IRF-3, Stat1, and PML Nuclear Bodies. *Journal of Interferon & Cytokine Research*, *26*(5), 271–280. https://doi.org/10.1089/jir.2006.26.271

Cole, J. L., & Hansen, J. C. (1999). Analytical ultracentrifugation as a contemporary biomolecular research tool. In *Journal of Biomolecular Techniques* (Vol. 10, Issue 4).

Cole, J. L., Lary, J. W., P. Moody, T., & Laue, T. M. (2008). Analytical Ultracentrifugation: Sedimentation Velocity and Sedimentation Equilibrium. In *Methods in Cell Biology* (Vol. 84). https://doi.org/10.1016/S0091-679X(07)84006-4

Da Vela, S., Braun, M. K., Dörr, A., Greco, A., Möller, J., Fu, Z., Zhang, F., & Schreiber, F. (2016). Kinetics of liquid–liquid phase separation in protein solutions exhibiting LCST phase behavior studied by time-resolved USAXS and VSANS. *Soft Matter*, *12*(46), 9334–9341. https://doi.org/10.1039/C6SM01837H

Davis, B. M., Rall, G. F., & Schnell, M. J. (2015a). Everything You Always Wanted to Know about Rabies Virus (But Were Afraid to Ask). In *Annual Review of Virology* (Vol. 2). https://doi.org/10.1146/annurev-virology-100114-055157

Davis, B. M., Rall, G. F., & Schnell, M. J. (2015b). Everything You Always Wanted to Know about Rabies Virus (But Were Afraid to Ask). In *Annual Review of Virology* (Vol. 2, pp. 451–471). Annual Reviews Inc. https://doi.org/10.1146/annurev-virology-100114-055157

de Castro Martin, I. F., Fournier, G., Sachse, M., Pizarro-Cerda, J., Risco, C., & Naffakh, N. (2017). Influenza virus genome reaches the plasma membrane via a modified endoplasmic reticulum and Rab11-dependent vesicles. *Nature Communications*, *8*(1), 1396. https://doi.org/10.1038/s41467-017-01557-6

de Jong Bungenberg, H. G., & Kruyt, H. R. (1929). Chemistry—Coacervation (Partial miscibility in colloid systems). *Proc. K. Ned. Akad. Wet.*, *32*.

Derdowski, A., Peters, T. R., Glover, N., Qian, R., Utley, T. J., Burnett, A., Williams, J. V., Spearman, P., & Crowe, J. E. (2008). Human metapneumovirus nucleoprotein and phosphoprotein interact and provide the minimal requirements for inclusion body formation. *Journal of General Virology*, *89*(11), 2698–2708. https://doi.org/10.1099/vir.0.2008/004051-0

Dhulipala, S., & Uversky, V. N. (2022). uvesk. *Biomolecules*, *12*(10), 1436. https://doi.org/10.3390/biom12101436

Dietzschold, B., Li, J., Faber, M., & Schnell, M. (2008). Concepts in the pathogenesis of rabies. *Future Virology*, *3*(5), 481–490. https://doi.org/10.2217/17460794.3.5.481

Dietzschold, B., Schnell, M., & Koprowski, H. (n.d.). Pathogenesis of Rabies. In *The World of Rhabdoviruses* (pp. 45–56). Springer-Verlag. https://doi.org/10.1007/3-540-27485-5_3

Dinh, P. X., Beura, L. K., Das, P. B., Panda, D., Das, A., & Pattnaik, A. K. (2013). Induction of Stress Granule-Like Structures in Vesicular Stomatitis Virus-Infected Cells. *Journal of Virology*, *87*(1), 372–383. https://doi.org/10.1128/JVI.02305-12

Du, M., & Chen, Z. J. (2018). DNA-induced liquid phase condensation of cGAS activates innate immune signaling. *Science*, *361*(6403), 704–709. https://doi.org/10.1126/science.aat1022

Dunker, A. K., Lawson, J. D., Brown, C. J., Williams, R. M., Romero, P., Oh, J. S., Oldfield, C. J., Campen, A. M., Ratliff, C. M., Hipps, K. W., Ausio, J., Nissen, M. S., Reeves, R., Kang, C., Kissinger, C. R., Bailey, R. W., Griswold, M. D., Chiu, W., Garner, E. C., & Obradovic, Z. (2001). Intrinsically disordered protein. *Journal of Molecular Graphics & Modelling*, *19*(1), 26–59. https://doi.org/10.1016/s1093-3263(00)00138-8

Dyson, H. J., & Wright, P. E. (2005). Intrinsically unstructured proteins and their functions. *Nature Reviews Molecular Cell Biology*, *6*(3), 197–208. https://doi.org/10.1038/nrm1589

El Asmi, F., Brantis-De-carvalho, C. E., Blondel, D., & Chelbi-Alix, M. K. (2018).

Rhabdoviruses, antiviral defense, and sumo pathway. In *Viruses* (Vol. 10, Issue 12). https://doi.org/10.3390/v10120686

Elbaum-Garfinkle, S., Kim, Y., Szczepaniak, K., Chen, C. C.-H., Eckmann, C. R., Myong, S., & Brangwynne, C. P. (2015). The disordered P granule protein LAF-1 drives phase separation into droplets with tunable viscosity and dynamics. *Proceedings of the National Academy of Sciences*, *112*(23), 7189–7194. https://doi.org/10.1073/pnas.1504822112

Emerson, S. U., & Yu, Y. (1975). Both NS and L proteins are required for in vitro RNA synthesis by vesicular stomatitis virus. *Journal of Virology*, *15*(6). https://doi.org/10.1128/jvi.15.6.1348-1356.1975

Emsley, P., & Cowtan, K. (2004). Coot : model-building tools for molecular graphics. *Acta Crystallographica Section D Biological Crystallography*, *60*(12), 2126–2132. https://doi.org/10.1107/S0907444904019158

Flory, P. J. (1942). Thermodynamics of High Polymer Solutions. *The Journal of Chemical Physics*, *10*(1), 51–61. https://doi.org/10.1063/1.1723621

Follett, E. A. C., Pringle, C. R., Wunner, W. H., & Skehel, J. J. (1974). Virus Replication in Enucleate Cells: Vesicular Stomatitis Virus and Influenza Virus. *Journal of Virology*, *13*(2), 394–399. https://doi.org/10.1128/jvi.13.2.394-399.1974

Fouquet, B., Nikolic, J., Larrous, F., Bourhy, H., Wirblich, C., Lagaudrière-Gesbert, C., & Blondel, D. (2015). Focal Adhesion Kinase Is Involved in Rabies Virus Infection through Its Interaction with Viral Phosphoprotein P. *Journal of Virology*, *89*(3), 1640–1651. https://doi.org/10.1128/JVI.02602-14

Gaudin, Y., Tuffereau, C., Durrer, P., Brunner, J., Flamand, A., & Ruigrok, R. (1999). Rabies virus-induced membrane fusion. *Molecular Membrane Biology*, *16*(1), 21–31. https://doi.org/10.1080/096876899294724

Ge, P., Tsao, J., Schein, S., Green, T. J., Luo, M., & Zhou, Z. H. (2010). Cryo-EM Model of the Bullet-Shaped Vesicular Stomatitis Virus. *Science*, *327*(5966), 689–693. https://doi.org/10.1126/science.1181766

Gérard, F. C. A., Bourhis, J. M., Mas, C., Branchard, A., Vu, D. D., Varhoshkova, S., Leyrat, C., & Jamin, M. (2022). Structure and Dynamics of the Unassembled Nucleoprotein of Rabies Virus in Complex with Its Phosphoprotein Chaperone Module. *Viruses*, *14*(12). https://doi.org/10.3390/v14122813

Gerard, F. C. A., Ribeiro, E. D. A., Albertini, A. A. V., Gutsche, I., Zaccai, G., Ruigrok, R. W. H., & Jamin, M. (2007). Unphosphorylated Rhabdoviridae phosphoproteins form elongated dimers in solution. *Biochemistry*, *46*(36), 10328–10338. https://doi.org/10.1021/bi7007799

Gerard, F. C. A., Ribeiro, E. de A., Leyrat, C., Ivanov, I., Blondel, D., Longhi, S., Ruigrok, R. W. H., & Jamin, M. (2009). Modular Organization of Rabies Virus Phosphoprotein. *Journal of Molecular Biology*, *388*(5), 978–996. https://doi.org/10.1016/j.jmb.2009.03.061

Greninger, A. L. (2018). The challenge of diagnostic metagenomics. *Expert Review of Molecular Diagnostics*, *18*(7), 605–615. https://doi.org/10.1080/14737159.2018.1487292

Harty, R. N., Paragas, J., Sudol, M., & Palese, P. (1999). A Proline-Rich Motif within the Matrix Protein of Vesicular Stomatitis Virus and Rabies Virus Interacts with WW Domains of Cellular Proteins: Implications for Viral Budding. *Journal of Virology*, *73*(4), 2921–2929. https://doi.org/10.1128/JVI.73.4.2921-2929.1999

HEENEY, J. L. (2006). Zoonotic viral diseases and the frontier of early diagnosis, control and prevention. *Journal of Internal Medicine*, *260*(5), 399–408. https://doi.org/10.1111/j.1365-2796.2006.01711.x

Hidaka, Y., Lim, C.-K., Takayama-Ito, M., Park, C.-H., Kimitsuki, K., Shiwa, N., Inoue, K., & Itou, T. (2018). Segmentation of the rabies virus genome. *Virus Research*, *252*, 68–75.

https://doi.org/10.1016/j.virusres.2018.05.017

Hirel, P. H., Schmitter, J. M., Dessen, P., Fayat, G., & Blanquet, S. (1989). Extent of N-terminal methionine excision from Escherichia coli proteins is governed by the side-chain length of the penultimate amino acid. *Proceedings of the National Academy of Sciences of the United States of America*, *86*(21). https://doi.org/10.1073/pnas.86.21.8247

Horwitz, J. A., Jenni, S., Harrison, S. C., & Whelan, S. P. J. (2020). Structure of a rabies virus polymerase complex from electron cryo-microscopy. *Proceedings of the National Academy of Sciences of the United States of America*, *117*(4). https://doi.org/10.1073/pnas.1918809117

HOWLETT, G., MINTON, A., & RIVAS, G. (2006). Analytical ultracentrifugation for the study of protein association and assembly. *Current Opinion in Chemical Biology*, *10*(5), 430–436. https://doi.org/10.1016/j.cbpa.2006.08.017

Huggins, M. L. (1942). Some Properties of Solutions of Long-chain Compounds. *The Journal of Physical Chemistry*, *46*(1), 151–158. https://doi.org/10.1021/j150415a018

Hyman, A. A., Weber, C. A., & Jülicher, F. (2014). Liquid-liquid phase separation in biology. In *Annual review of cell and developmental biology* (Vol. 30, pp. 39–58). https://doi.org/10.1146/annurev-cellbio-100913-013325

Inoue, T., & Tsai, B. (2013). How Viruses Use the Endoplasmic Reticulum for Entry, Replication, and Assembly. *Cold Spring Harbor Perspectives in Biology*, *5*(1), a013250–a013250. https://doi.org/10.1101/cshperspect.a013250

Irie, T., Licata, J. M., Jayakar, H. R., Whitt, M. A., Bell, P., & Harty, R. N. (2004). Functional Analysis of Late-Budding Domain Activity Associated with the PSAP Motif within the Vesicular Stomatitis Virus M Protein. *Journal of Virology*, *78*(14), 7823–7827. https://doi.org/10.1128/JVI.78.14.7823-7827.2004

Iseni, F., Barge, A., Baudin, F., Blondel, D., & Ruigrok, R. W. H. (1998). Characterization of rabies virus nucleocapsids and recombinant nucleocapsid-like structures. *Journal of General Virology*, *79*(12). https://doi.org/10.1099/0022-1317-79-12-2909

Ivanov, I., Crépin, T., Jamin, M., & Ruigrok, R. W. H. (2010). Structure of the Dimerization Domain of the Rabies Virus Phosphoprotein. *Journal of Virology*, *84*(7). https://doi.org/10.1128/jvi.02557-09

Jespersen, N. E., Leyrat, C., Gérard, F. C., Bourhis, J. M., Blondel, D., Jamin, M., & Barbar, E. (2019). The LC8-RavP ensemble Structure Evinces A Role for LC8 in Regulating Lyssavirus Polymerase Functionality. *Journal of Molecular Biology*, *431*(24). https://doi.org/10.1016/j.jmb.2019.10.011

Kammouni, W., Wood, H., Saleh, A., Appolinario, C. M., Fernyhough, P., & Jackson, A. C. (2015). Rabies virus phosphoprotein interacts with mitochondrial Complex I and induces mitochondrial dysfunction and oxidative stress. *Journal of NeuroVirology*, *21*(4), 370–382. https://doi.org/10.1007/s13365-015-0320-8

Kim, S., Huang, J., Lee, Y., Dutta, S., Yoo, H. Y., Jung, Y. M., Jho, Y., Zeng, H., & Hwang, D. S. (2016). Complexation and coacervation of like-charged polyelectrolytes inspired by mussels. *Proceedings of the National Academy of Sciences*, *113*(7). https://doi.org/10.1073/pnas.1521521113

Koonin, E. V., Krupovic, M., & Agol, V. I. (2021). The Baltimore Classification of Viruses 50 Years Later: How Does It Stand in the Light of Virus Evolution? *Microbiology and Molecular Biology Reviews*, *85*(3). https://doi.org/10.1128/MMBR.00053-21

Koonin, E. V, Senkevich, T. G., & Dolja, V. V. (2006). The ancient Virus World and evolution of cells. *Biology Direct*, *1*(1), 29. https://doi.org/10.1186/1745-6150-1-29

Kuhn, J. H., Adkins, S., Alioto, D., Alkhovsky, S. V., Amarasinghe, G. K., Anthony, S. J., Avšič-Županc, T., Ayllón, M. A., Bahl, J., Balkema-Buschmann, A., Ballinger, M. J., Bartonička, T., Basler, C., Bavari, S., Beer, M., Bente, D. A., Bergeron, É., Bird, B. H., Blair, C., … Zhou, X. (2020). 2020 taxonomic update for phylum Negarnaviricota (Riboviria: Orthornavirae), including the large orders Bunyavirales and Mononegavirales. *Archives of Virology*, *165*(12). https://doi.org/10.1007/s00705-020-04731-2

Lahaye, X., Vidy, A., Pomier, C., Obiang, L., Harper, F., Gaudin, Y., & Blondel, D. (2009). Functional Characterization of Negri Bodies (NBs) in Rabies Virus-Infected Cells: Evidence that NBs Are Sites of Viral Transcription and Replication. *Journal of Virology*, *83*(16), 7948–7958. https://doi.org/10.1128/jvi.00554-09

Lamarsh, J. R., & Melkonian, E. (1977). Introduction to Nuclear Engineering. *Physics Today*, *30*(6). https://doi.org/10.1063/1.3037597

Leabu, M. (2006). Membrane fusion in cells: molecular machinery and mechanisms. *Journal of Cellular and Molecular Medicine*, *10*(2), 423–427. https://doi.org/10.1111/j.1582-4934.2006.tb00409.x

Leyrat, C., C.A. Gerard, F., de Almeida Ribeiro Jr., E., Ivanov, I., W.H. Ruigrok, R., & Jamin, M. (2010). Structural Disorder in Proteins of the Rhabdoviridae Replication Complex. *Protein & Peptide Letters*, *17*(8), 979–987. https://doi.org/10.2174/092986610791498939

Leyrat, C., Ribeiro, E. A., Gérard, F. C. A., Ivanov, I., Ruigrok, R. W. H., & Jamin, M. (2011). Structure, interactions with host cell and functions of rhabdovirus phosphoprotein. In *Future Virology* (Vol. 6, Issue 4, pp. 465–481). https://doi.org/10.2217/fvl.11.10

Leyrat, C., Schneider, R., Ribeiro, E. A., Yabukarski, F., Yao, M., Gérard, F. C. A., Jensen, M. R., Ruigrok, R. W. H., Blackledge, M., & Jamin, M. (2012). Ensemble Structure of the Modular and Flexible Full-Length Vesicular Stomatitis Virus Phosphoprotein. *Journal of Molecular Biology*, *423*(2), 182–197. https://doi.org/10.1016/j.jmb.2012.07.003

Li, Y., Dong, W., Shi, Y., Deng, F., Chen, X., Wan, C., Zhou, M., Zhao, L., Fu, Z. F., & Peng, G. (2016). Rabies virus phosphoprotein interacts with ribosomal protein L9 and affects rabies virus replication. *Virology*, *488*, 216–224. https://doi.org/10.1016/j.virol.2015.11.018

Liang, B. (2020). Structures of the Mononegavirales Polymerases. *Journal of Virology*, *94*(22). https://doi.org/10.1128/JVI.00175-20

Liu, J., Wang, H., Gu, J., Deng, T., Yuan, Z., Hu, B., Xu, Y., Yan, Y., Zan, J., Liao, M., DiCaprio, E., Li, J., Su, S., & Zhou, J. (2017). BECN1-dependent CASP2 incomplete autophagy induction by binding to rabies virus phosphoprotein. *Autophagy*, *13*(4), 739–753. https://doi.org/10.1080/15548627.2017.1280220

Majeed, S. A., Sekhosana, K. E., & Tuhl, A. (2020). Progress on phthalocyanine-conjugated Ag and Au nanoparticles: Synthesis, characterization, and photo-physicochemical properties. *Arabian Journal of Chemistry*, *13*(12), 8848–8887. https://doi.org/10.1016/j.arabjc.2020.10.014

Mavrakis, M., McCarthy, A. A., Roche, S., Blondel, D., & Ruigrok, R. W. H. (2004). Structure and function of the C-terminal domain of the polymerase cofactor of rabies virus. *Journal of Molecular Biology*, *343*(4). https://doi.org/10.1016/j.jmb.2004.08.071

Milkovic, N. M., & Mittag, T. (2020). Determination of protein phase diagrams by centrifugation. In *Methods in Molecular Biology* (Vol. 2141). https://doi.org/10.1007/978-1-0716-0524-0_35

Najafi, S., Lin, Y., Longhini, A. P., Zhang, X., Delaney, K. T., Kosik, K. S., Fredrickson, G. H., Shea, J., & Han, S. (2021). Liquid–liquid phase separation of Tau by self and complex coacervation. *Protein Science*, *30*(7), 1393–1407. https://doi.org/10.1002/pro.4101

Neil, S. J. D., Eastman, S. W., Jouvenet, N., & Bieniasz, P. D. (2006). HIV-1 Vpu Promotes Release and Prevents Endocytosis of Nascent Retrovirus Particles from the Plasma Membrane. *PLoS Pathogens*, *2*(5), e39. https://doi.org/10.1371/journal.ppat.0020039

Nevers, Q., Scrima, N., Glon, D., Le Bars, R., Decombe, A., Garnier, N., Ouldali, M., Lagaudrière-Gesbert, C., Blondel, D., Albertini, A., & Gaudin, Y. (2022). Properties of rabies virus phosphoprotein and nucleoprotein biocondensates formed in vitro and in cellulo. *PLOS Pathogens*, *18*(12), e1011022. https://doi.org/10.1371/journal.ppat.1011022

Nikolic, J., Lagaudrière-Gesbert, C., Scrima, N., Blondel, D., & Gaudin, Y. (2019). Structure and Function of Negri Bodies. In *Advances in Experimental Medicine and Biology* (Vol. 1140, pp. 111–127). Springer New York LLC. https://doi.org/10.1007/978-3-030-14741-9_6

Nikolic, J., Le Bars, R., Lama, Z., Scrima, N., Lagaudrière-Gesbert, C., Gaudin, Y., & Blondel, D. (2017a). Negri bodies are viral factories with properties of liquid organelles. *Nature Communications*, *8*(1), 1–13. https://doi.org/10.1038/s41467-017-00102-9

Nikolic, J., Le Bars, R., Lama, Z., Scrima, N., Lagaudrière-Gesbert, C., Gaudin, Y., & Blondel, D. (2017b). Negri bodies are viral factories with properties of liquid organelles. *Nature Communications*, *8*(1). https://doi.org/10.1038/s41467-017-00102-9

Nott, T. J., Petsalaki, E., Farber, P., Jervis, D., Fussner, E., Plochowietz, A., Craggs, T. D., Bazett-Jones, D. P., Pawson, T., Forman-Kay, J. D., & Baldwin, A. J. (2015). Phase transition of a disordered nuage protein generates environmentally responsive membraneless organelles. *Molecular Cell*, *57*(5), 936–947. https://doi.org/10.1016/j.molcel.2015.01.013

Nozawa, R., Yamamoto, T., Takahashi, M., Tachiwana, H., Maruyama, R., Hirota, T., & Saitoh, N. (2020). Nuclear microenvironment in cancer: Control through liquid-liquid phase separation. *Cancer Science*, *111*(9), 3155–3163. https://doi.org/10.1111/cas.14551

Ohki, S. (Ed.). (1991). *Cell and Model Membrane Interactions*. Springer US. https://doi.org/10.1007/978-1-4615-3854-7

Oksayan, S., Wiltzer, L., Rowe, C. L., Blondel, D., Jans, D. A., & Moseley, G. W. (2012). A Novel Nuclear Trafficking Module Regulates the Nucleocytoplasmic Localization of the Rabies Virus Interferon Antagonist, P Protein. *Journal of Biological Chemistry*, *287*(33), 28112–28121. https://doi.org/10.1074/jbc.M112.374694

Pearce, J. (2002). Louis Pasteur and Rabies: a brief note. *Journal of Neurology, Neurosurgery & Psychiatry*, *73*(1), 82–82. https://doi.org/10.1136/jnnp.73.1.82

Pellett, P. E., Mitra, S., & Holland, T. C. (2014). *Basics of virology* (pp. 45–66). https://doi.org/10.1016/B978-0-444-53488-0.00002-X

Poch, O., Sauvaget, I., Delarue, M., & Tordo, N. (1989). Identification of four conserved motifs among the RNA-dependent polymerase encoding elements. *EMBO Journal*, *8*(12). https://doi.org/10.1002/j.1460-2075.1989.tb08565.x

Poulsen, N. N., Andersen, N. Z., Østergaard, J., Zhuang, G., Petersen, N. J., & Jensen, H. (2015). Flow induced dispersion analysis rapidly quantifies proteins in human plasma samples. *The Analyst*, *140*(13), 4365–4369. https://doi.org/10.1039/C5AN00697J

Prabhu, V. M., Ali, S., Bleuel, M., Mao, Y., & Ma, Y. (2021). *Ultra-small angle neutron scattering to study droplet formation in polyelectrolyte complex coacervates* (pp. 261–276). https://doi.org/10.1016/bs.mie.2020.07.001

Pringle, C. R. (1997). The order Mononegavirales--current status. *Archives of Virology*, *142*(11).

Putnam, C. D., Hammel, M., Hura, G. L., & Tainer, J. A. (2007). X-ray solution scattering (SAXS) combined with crystallography and computation: defining accurate macromolecular structures, conformations and assemblies in solution. *Quarterly Reviews of Biophysics*, *40*(3), 191–285. https://doi.org/10.1017/S0033583507004635

Rabouille, C. (2019). Membraneless organelles in cell biology. *Traffic*, *20*(12), 885–886. https://doi.org/10.1111/tra.12686

Ranganathan, S., & Shakhnovich, E. (2019). Liquid-liquid microphase separation leads to formation of membraneless organelles. *BioRxiv*, 2019.12.18.881565.

https://doi.org/10.1101/2019.12.18.881565

Redondo-Morata, L., Losada-Pérez, P., & Giannotti, M. I. (2020). *Lipid bilayers: Phase behavior and nanomechanics* (pp. 1–55). https://doi.org/10.1016/bs.ctm.2020.08.005

Ribeiro, E. A., Favier, A., Gerard, F. C. A., Leyrat, C., Brutscher, B., Blondel, D., Ruigrok, R. W. H., Blackledge, M., & Jamin, M. (2008). Solution Structure of the C-Terminal Nucleoprotein–RNA Binding Domain of the Vesicular Stomatitis Virus Phosphoprotein. *Journal of Molecular Biology*, *382*(2), 525–538. https://doi.org/10.1016/j.jmb.2008.07.028

Ribeiro, E. de A., Leyrat, C., Gérard, F. C. A., Albertini, A. A. V., Falk, C., Ruigrok, R. W. H., & Jamin, M. (2009). Binding of Rabies Virus Polymerase Cofactor to Recombinant Circular Nucleoprotein–RNA Complexes. *Journal of Molecular Biology*, *394*(3), 558–575. https://doi.org/10.1016/j.jmb.2009.09.042

Riggs, C. L., Kedersha, N., Ivanov, P., & Anderson, P. (2020). Mammalian stress granules and P bodies at a glance. *Journal of Cell Science*, *133*(16). https://doi.org/10.1242/jcs.242487

Rincheval, V., Lelek, M., Gault, E., Bouillier, C., Sitterlin, D., Blouquit-Laye, S., Galloux, M., Zimmer, C., Eleouet, J.-F., & Rameix-Welti, M.-A. (2017). Functional organization of cytoplasmic inclusion bodies in cells infected by respiratory syncytial virus. *Nature Communications*, *8*(1), 563. https://doi.org/10.1038/s41467-017-00655-9

Robert J. Silbey, R. A. A. M. G. B. (2004). *Physical Chemistry, 4th Edition* (martin batey).

Roossinck, M. J., & Bazán, E. R. (2017). Symbiosis: Viruses as Intimate Partners. *Annual Review of Virology*, *4*(1), 123–139. https://doi.org/10.1146/annurev-virology-110615-042323

Ruff, K. M., Roberts, S., Chilkoti, A., & Pappu, R. V. (2018). Advances in Understanding Stimulus-Responsive Phase Behavior of Intrinsically Disordered Protein Polymers. *Journal of Molecular Biology*, *430*(23), 4619–4635. https://doi.org/10.1016/j.jmb.2018.06.031

Ruigrok, R. W. H., Crépin, T., & Kolakofsky, D. (2011). Nucleoproteins and nucleocapsids of negative-strand RNA viruses. *Current Opinion in Microbiology*, *14*(4). https://doi.org/10.1016/j.mib.2011.07.011

Ryan, V. H., & Fawzi, N. L. (2019). Physiological, Pathological, and Targetable Membraneless Organelles in Neurons. *Trends in Neurosciences*, *42*(10), 693–708. https://doi.org/10.1016/j.tins.2019.08.005

Sitnikova, N. L., Sprik, R., Wegdam, G., & Eiser, E. (2005). Spontaneously Formed trans - Anethol/Water/Alcohol Emulsions: Mechanism of Formation and Stability. *Langmuir*, *21*(16), 7083–7089. https://doi.org/10.1021/la046816l

Solon, J., Gareil, O., Bassereau, P., & Gaudin, Y. (2005). Membrane deformations induced by the matrix protein of vesicular stomatitis virus in a minimal system. *Journal of General Virology*, *86*(12), 3357–3363. https://doi.org/10.1099/vir.0.81129-0

Somjee, R., Mitrea, D. M., & Kriwacki, R. W. (2020). Exploring relationships between the density of charged tracts within disordered regions and phase separation. *Pacific Symposium on Biocomputing*, *25*(2020). https://doi.org/10.1142/9789811215636_0019

Stender, E. G. P., Ray, S., Norrild, R. K., Larsen, J. A., Petersen, D., Farzadfard, A., Galvagnion, C., Jensen, H., & Buell, A. K. (2021). Capillary flow experiments for thermodynamic and kinetic characterization of protein liquid-liquid phase separation. *Nature Communications*, *12*(1). https://doi.org/10.1038/s41467-021-27433-y

te Velthuis, A. J. W., Grimes, J. M., & Fodor, E. (2021). Structural insights into RNA polymerases of negative-sense RNA viruses. *Nature Reviews Microbiology*, *19*(5), 303–318. https://doi.org/10.1038/s41579-020-00501-8

Thaker, S. K., Ch'ng, J., & Christofk, H. R. (2019). Viral hijacking of cellular metabolism. *BMC Biology*, *17*(1), 59. https://doi.org/10.1186/s12915-019-0678-9

Uversky, V. N. (1993). Use of fast protein size-exclusion liquid chromatography to study the unfolding of proteins which denature through the molten globule. *Biochemistry*, *32*(48), 13288–13298. https://doi.org/10.1021/bi00211a042

Uversky, V. N., Kuznetsova, I. M., Turoverov, K. K., & Zaslavsky, B. (2015). Intrinsically disordered proteins as crucial constituents of cellular aqueous two phase systems and coacervates. *FEBS Letters*, *589*(1), 15–22. https://doi.org/10.1016/j.febslet.2014.11.028

Vidy, A., Chelbi-Alix, M., & Blondel, D. (2005). Rabies Virus P Protein Interacts with STAT1 and Inhibits Interferon Signal Transduction Pathways. *Journal of Virology*, *79*(22), 14411–14420. https://doi.org/10.1128/JVI.79.22.14411-14420.2005

Vitale, S. A., & Katz, J. L. (2003). Liquid Droplet Dispersions Formed by Homogeneous Liquid−Liquid Nucleation: “The Ouzo Effect.” *Langmuir*, *19*(10), 4105–4110. https://doi.org/10.1021/la026842o

WALL, F. T. (1954). Principles of Polymer Chemistry. Paul J. Flory. Cornell Univ. Press, Ithaca, New York, 1953. 688 pp. Illus. $8.50. *Science*, *119*(3095). https://doi.org/10.1126/science.119.3095.555-a

Wang, J., Choi, J.-M., Holehouse, A. S., Lee, H. O., Zhang, X., Jahnel, M., Maharana, S., Lemaitre, R., Pozniakovsky, A., Drechsel, D., Poser, I., Pappu, R. V., Alberti, S., & Hyman, A. A. (2018). A Molecular Grammar Governing the Driving Forces for Phase Separation of Prion-like RNA Binding Proteins. *Cell*, *174*(3), 688-699.e16. https://doi.org/10.1016/j.cell.2018.06.006

Weber, D. J., Juliano, J. J., & Rutala, W. A. (2015). Systemic infection from animals. In *Clinical Infectious Disease* (pp. 790–796). Cambridge University Press. https://doi.org/10.1017/CBO9781139855952.135

Weinherg, A. M. (1959). The Physical Theory of Neutron Chain Reactors. *Physics Today*, *12*(3). https://doi.org/10.1063/1.3060719

Weisskopf, V. (1937). Statistics and Nuclear Reactions. *Physical Review*, *52*(4), 295–303. https://doi.org/10.1103/PhysRev.52.295

Wichgers Schreur, P. J., & Kortekaas, J. (2016). Single-Molecule FISH Reveals Non-selective Packaging of Rift Valley Fever Virus Genome Segments. *PLOS Pathogens*, *12*(8), e1005800. https://doi.org/10.1371/journal.ppat.1005800

Xu, Y., Liu, F., Liu, J., Wang, D., Yan, Y., Ji, S., Zan, J., & Zhou, J. (2016). The co-chaperone Cdc37 regulates the rabies virus phosphoprotein stability by targeting to Hsp90AA1 machinery. *Scientific Reports*, *6*(1), 27123. https://doi.org/10.1038/srep27123

Yabukarski, F., Leyrat, C., Martinez, N., Communie, G., Ivanov, I., Ribeiro, E. A., Buisson, M., Gerard, F. C., Bourhis, J.-M., Jensen, M. R., Bernadó, P., Blackledge, M., & Jamin, M. (2016). Ensemble Structure of the Highly Flexible Complex Formed between Vesicular Stomatitis Virus Unassembled Nucleoprotein and its Phosphoprotein Chaperone. *Journal of Molecular Biology*, *428*(13), 2671–2694. https://doi.org/10.1016/j.jmb.2016.04.010

Zaccai, N. R., Sandlin, C. W., Hoopes, J. T., Curtis, J. E., Fleming, P. J., Fleming, K. G., & Krueger, S. (2016). *Deuterium Labeling Together with Contrast Variation Small-Angle Neutron Scattering Suggests How Skp Captures and Releases Unfolded Outer Membrane Proteins* (pp. 159–210). https://doi.org/10.1016/bs.mie.2015.06.041

Zhou, Y., Su, J. M., Samuel, C. E., & Ma, D. (2019). Measles Virus Forms Inclusion Bodies with Properties of Liquid Organelles. *Journal of Virology*, *93*(21). https://doi.org/10.1128/JVI.00948-19

### ii. Complementary results

For the next part, note that 120 mM NaCl = 130mM of ionic strength.

- ***RABV P forms supramolecular complexes above a thresheld concentration***

As shown in the article, at concentrations equal or higher than 1 mg/mL species larger than the dimer appeared (**Figure, 35**), and the dimer disappeared. Dimeric form represented 57% at 2mg/mL, 32% at 3.5mg/mL and 23% at 6.5 mg/mL (**Figure, 36**).

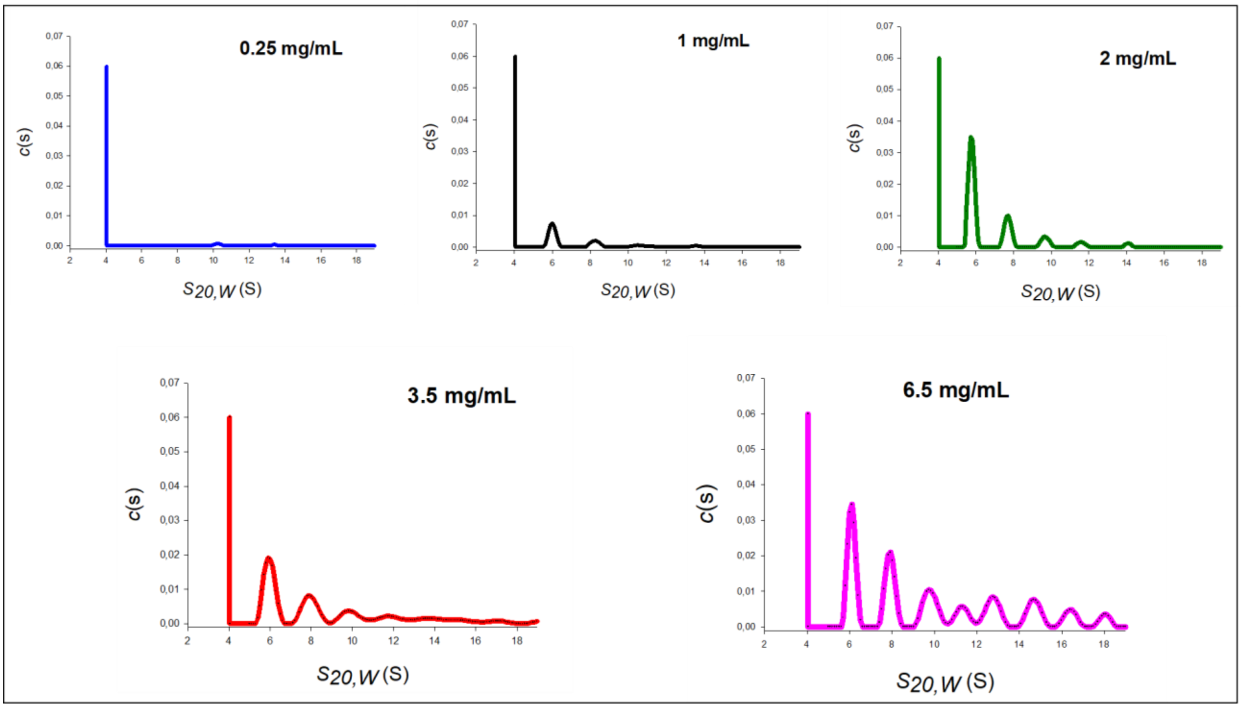

*Figure 35. Sedimentation velocity analysis of RABV phosphoprotein at different protein concentrations. The sedimentation coefficients at the maximum of the distributions, which correspond to the dimer, were set to 4S, and represented by a single line; pics correspond to larger forms than dimer.*

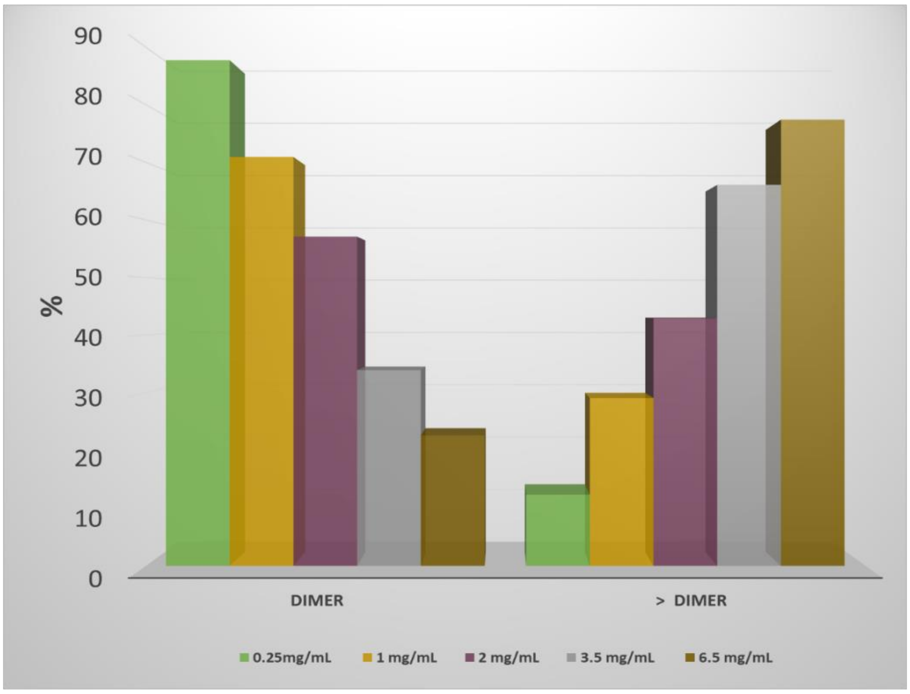

*Figure 36. Sedimentation velocity analysis: Distribution of the dimer and forms larger than the dimer obtained by sedimentation velocity experiment in different protein concentrations.*

Measurements of RABV P in diluted conditions (0.5mg/mL) at 200 mM and 500 mM NaCl showed similar results at both 4°C and 20°C (**Figure, 37**). We measured $R_g$ values of 4.70 ± 0.07 and 4.81 ± 0.04 for 200 mM and 500 mM respectively. Thus, 200 mM NaCl (in which electrostatics is largely screened by the diluted salt) was sufficient to maintain the protein in its dimeric state in the solution, at least a low protein concentrations.

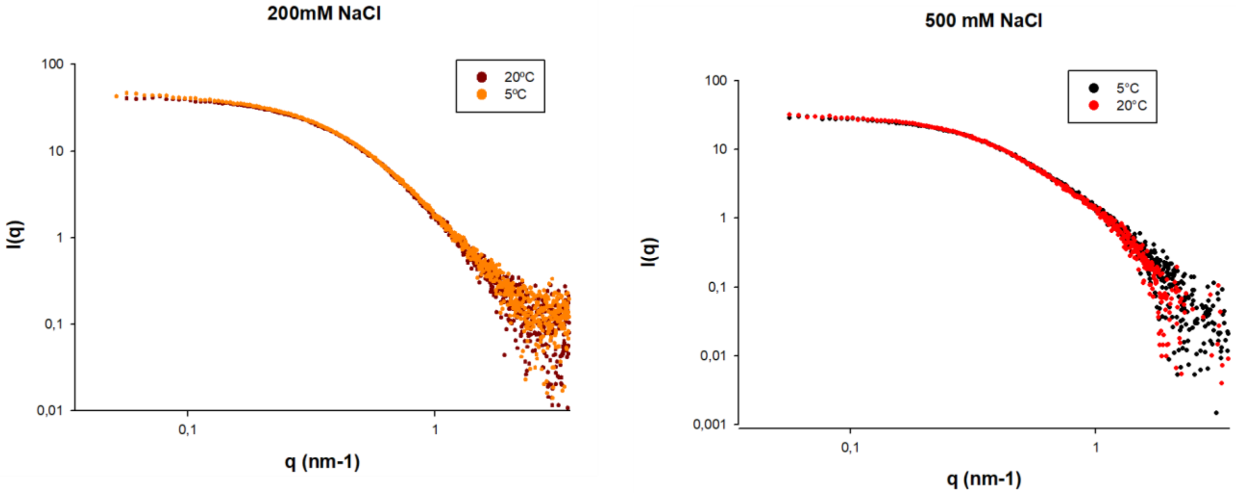

*Figure 37.Raw SAXS scattering data of RABV P at a protein concentration of 0.5mg/mL, and salt concentration of 200mM and 500mM NaCl at 5 ℃ and 20 °*

### • ***SANS and SAXS measurement of LLPS***

We investigated by SAXS and SANS the shape and size of RABV P in the region of the phase diagram where liquid liquid phase separation occurred. In a first experiment, we measured SANS profiles in the q range comprised between 0.04 nm$^{-1}$ and 0.6 nm$^{-1}$, at an ionic strength of 130 mM and at a protein concentration of 8 mg.mL$^{-1}$ (**Figures, 38A and 38B**). We concentrated the sample and filled the cuvette at 5°C and measured SANS profiles at increasing temperatures up to 20°C. The profiles between 4 to 11 °C are shown in (**Figure, 38A**) and those between 11 to 20 °C and after bringing the sample back to 4 °C are shown in (**Figure, 38B**)

At each temperature, we determined the Rg value and the intensity at zero angle ($I_0$) by using GUINIER approximation for Q.Rg < 1.3. At 5°C, the solution was transparent but the $R_g$ of 10.5 ± 0.5 nm and the average MM of kDa determined from $I_0$ showed that the protein was already assembled into soluble supramolecular complexes, even larger than those found in similar conditions but at lower protein concentrations (**Figure, 38C**). The scattering invariant values that is essentially proportional to the concentration of proteins, decreased with increasing temperature, and did not come back to its initial value at 4°C (**Figure, 38D**).

Both $R_g$ and $I_0$ values increased with temperature up to 13°C, the temperature from which the sample became opalescent indicating the onset of phase separation (**Figure, 38A**). Above 13°C, both Rg and $I_0$ values decreased with increasing temperature, likely reflecting the formation of droplets of micrometer size. The droplets were too large to give a measurable scattering signal in this q range, and the measured signal reported only on the size and concentration of the supramolecular complexes that remained in the diluted phase. At 20°C, we measured an $R_g$ value of 9.0 ± 0.5 nm and an average MM of 284 ± 4 kDa for these soluble complexes, and lowering the temperature to 4°C had no effect on the size or average MM.

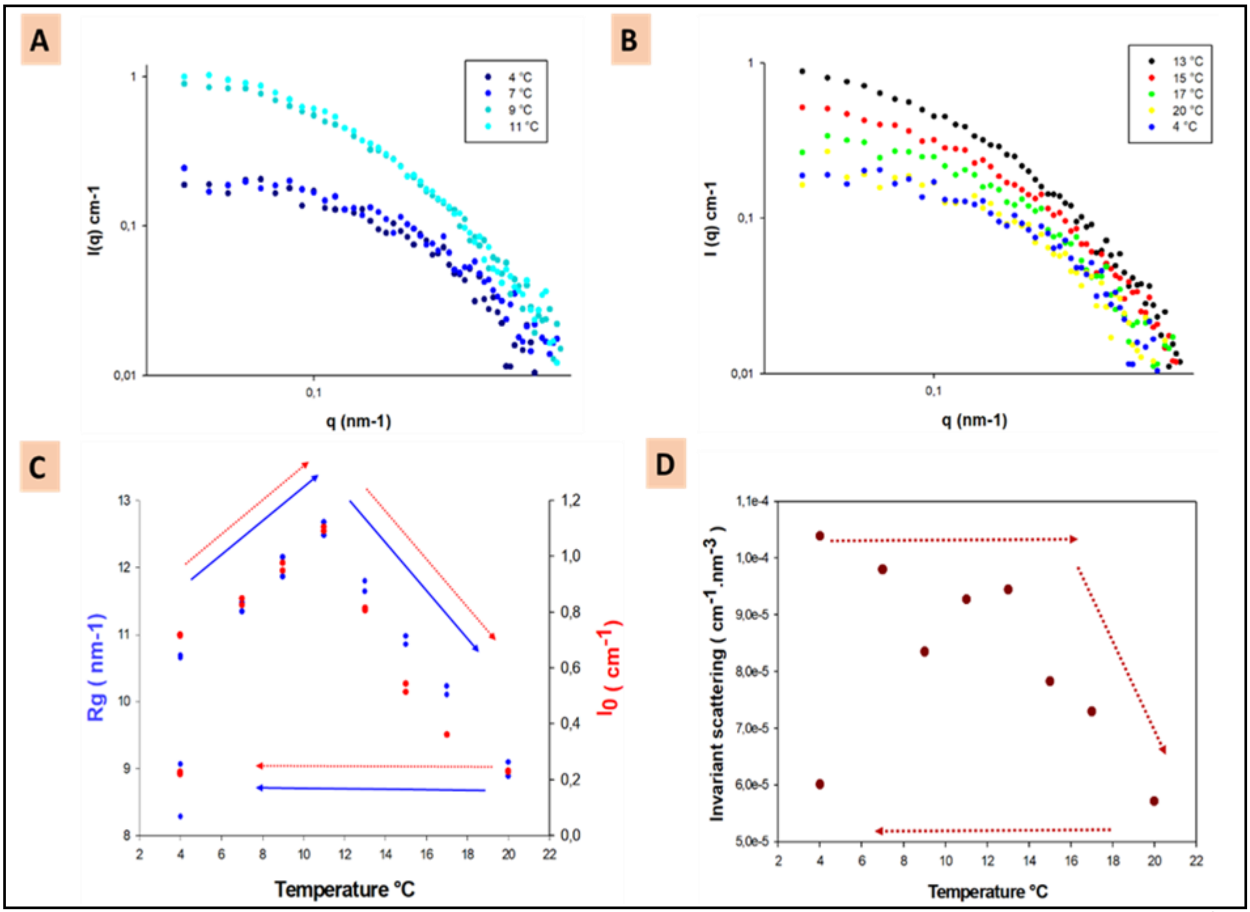

*Figure 38. SANS experiment were done with RABV P sample with a protein concentration of 8 mg/mL, and salt concentration of 120mM NaCl, after increasing temperatures. : (**A**) From 4℃ to 11℃. **(B)** From 13℃ to 20℃ and comeback to 4℃. **(C).** Evolution of $R_g$ and $I_0$ values from SANS experiment at increasing temperatures and comeback to 4℃. (**D**). Evolution of Invariant scattering values from SANS experiment.*

We complemented these results with SAXS measurements. We prepared a sample at an ionic strength of 130 mM, a RABV P concentration of 8 mg.mL$^{-1}$ and 5°C, and then we measured the sample at increasing temperature (**Figure, 39A**). At this protein concentration, the solution undergoes liquid-liquid phase separation near 14°C. The results showed a graduate increase of scattering at small q range. We then centrifuged the sample at 20°C and 1000 g and measured the concentration of the supernatant by absorbance spectroscopy (= 4.5 mg/mL). We measured SAXS profile for q values ranging 0.04 nm$^{-1}$ to 6 nm$^{-1}$ (**Figure, 39B**). The Rg and MM of the light phase calculated from $I_0$ revealed $R_g$= 9.25 ± 0.25 and MM =300 ± 3 kDa (almost five fold the MM of the dimer). Given the gel-like aspect of the coacervate, it was difficult to collect and measure the volume. To obtain information about the coacervate, we estimated visually the volume to be 50 uL and resuspended the with 200 uL of buffer and recorded the SAXS curve. We measured an $R_g$ of 15.89 ± 0.22.

Results of SANS and SAXS confirmed our results obtained using USAXS (Article **Figure, 9**). We observed the same plateau region in the intermediate q range (0.05 – 0.2 $nm^{-1}$) for both diluted and dense phase. The shape of curve for both phases followed a similar trend than that of the diluted phase, with the scattering decay following a power law in $q^{-2}$. On the other hand, the scattering invariant obtained from SANS experiment that is proportional to the concentration of proteins helped understanding our observations, the non-reversible decrease observed with increasing temperature demonstrated that less scattering material remained in solution.

Unlike for SANS measurement (**Figures, 38A,B**), SAXS measurements at increasing temperature (**Figure, 39A**) did not show a decrease in signal starting from 14°C. The time scale for SAXS and SANS acquisition differed. For SAXS, samples are stored at low temperature and simply injected in a heated capillary and the measurements are performed a few minutes after injection. Whereas, for SANS, samples are loaded in a 1 mm cuvette in sample changer, and thus more time is left for macroscopic phase separation. Thus, using SAXS we assumed that we observed the formation of larger forms before the appearance of droplets in the solution.

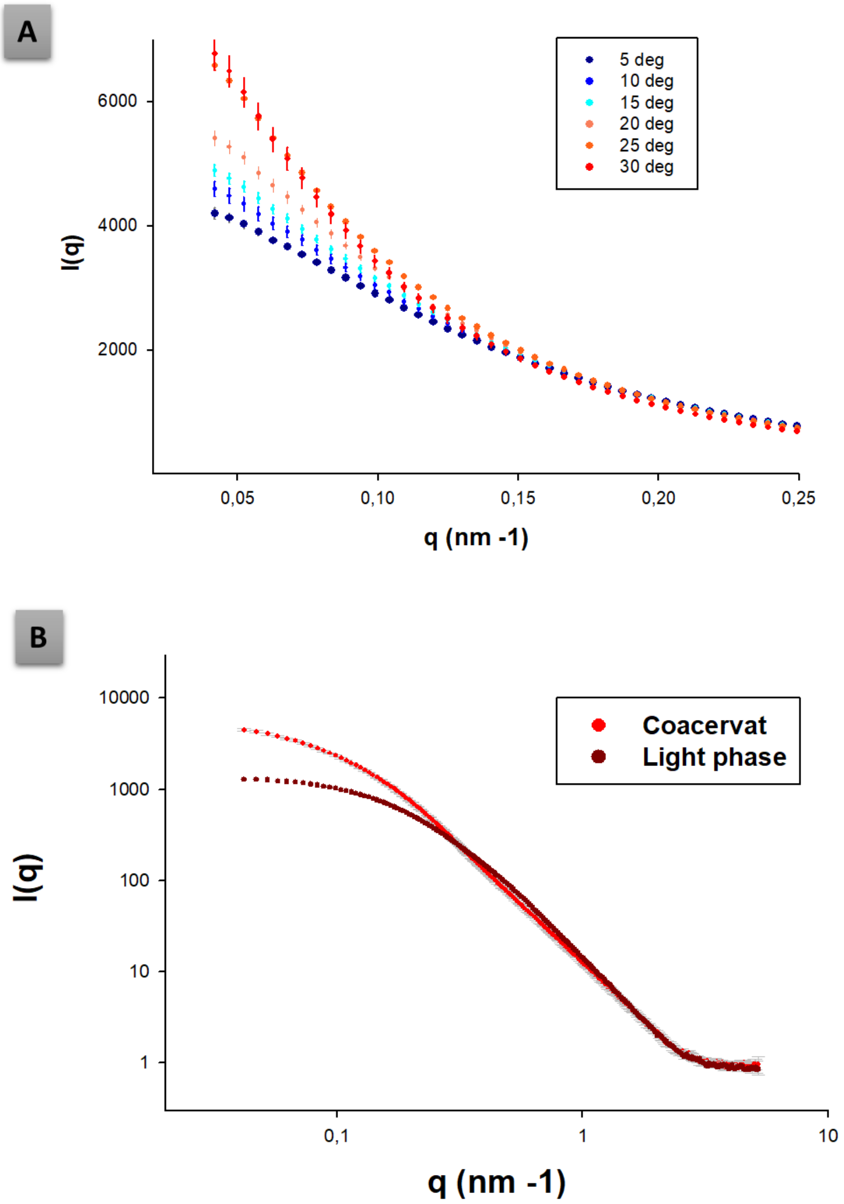

*Figure 39. SAXS experiment of RABV P at 8mg/mL, 120mM NaCl salt concentration, which forms LLPS above 14℃. (**A**) Raw SAXS scattering data measured by increasing temperature from 5℃ to 30℃. (**B**) Raw SAXS scattering data of the sample after centrifugation at 100g, 20℃, resulting supernatant (Light phase) and pellet (coacervate) were measured at 20℃.*

In order to confirm our results, we repeated light phase/coacervate measurement using SAXS and USAXS. We used RABV P samples at 8mg/mL and 6mg/mL LLPS samples at room temperature, but tried to use perfluorinated oil at the base of the capillary to raise the coacervate in hope of providing a flat interface, that could improve our measurments. In principle, since the density of the oil is larger than that of water, it should sediment at the bottom of the tube. However, our results showed that the oil was still mixed with the coacervate. Consequently, the transmission also fluctuates. Despite this hurdle, long analysis, allowed us to confirm a major part of the previous results (Article, **Figure, 9**). In the few intensity spectra of the coacervate that we managed to analyze, we found the plateau at intermediate q (0.1nm$^{-1}$) and a power low of q$^{-3}$ at low q. Moreover, the transition from coacervate to oil is much faster in the most diluted solution (6 mg/mL), which was coherent since the volume of coacervate was smaller.

We performed several USAXS experiments (ID02), and the path to obtain these results was far from easy. We measured both phases after centrifugation several times and encountered many problems with the type of capillaries used. Moreover we tried different types of centrifugations (with a swinging bucket rotor or vertically) but even at low centrifugation speed the capillaries broke during centrifugation.

- ***RABV P above the critical temperature***

In a simple binary system, the plot of T$_{\text{Cloud}}$ as a function of protein concentration at a given ionic strength determines the coexistence line or binodal (Thomson et al. 1987). This plot defines regions in the phase plot where one or two phases exist and predicts that at a given temperature the concentrations of both light and dense phases are independent of protein concentration. Only the volumes of the light and dense phases vary with protein concentration. A similar curve should be obtained when solutions at an initial temperature well below the coexistence curve are transferred and incubated above T$_{\text{Cloud}}$ and allowed to separate into two coexisting phases. The concentrations of the dense and diluted phases should fall on the coexistence curve at the set temperature.

As shown previously, we established RABV P phase diagram, which follows an LCST system, by measuring T$_{\text{cloud}}$, in the first place. Then, upon transferring a solution from low temperature to a temperature above the LCST, phase separation occur, thus, by centrifugation droplets sediment, and result in a two-phase decomposition. After we removed carefully the supernatant (light phase) for concentration determination by spectrophotometry, we obtained high concentration values compared to what was expected based on our binodal curve (**Figure, 40A**) generated from $T_{\mathbf{cloud}}$ (Article**, Figure, 5**). For example, for a solution of 7 mg/ml concentration, the measured light concentration was 4 mg/ml, whereas based on the binodal curve ($T_{cloud}$) we expected a concentration < 1 mg/mL. At a given temperature, the light phase concentration and by extension the dense phase concentration are not constant; they change depending on the total protein concentration. These results are in agreement with our results using FIDA, which shows according to the baseline that the concentration of light phase is still high (**Figure, 40B**).

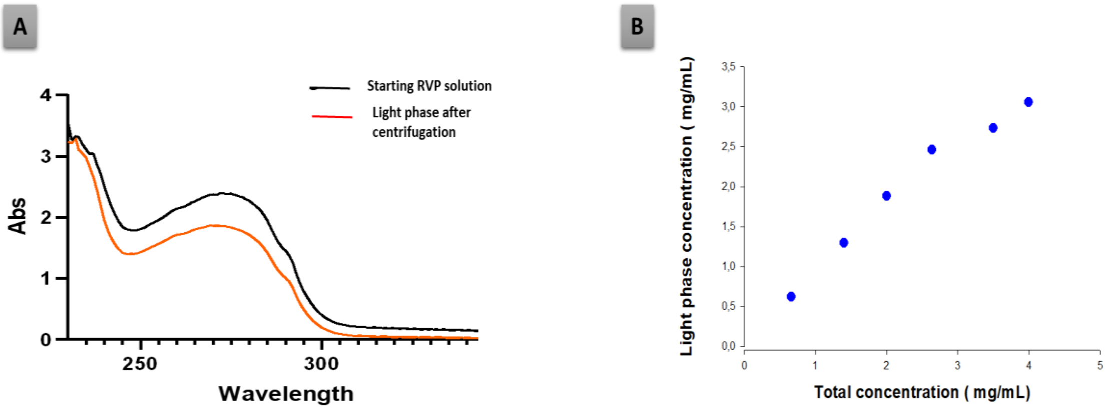

*Figure, 40.* ***(A)*** *Absorbance spectra of the initial RABV P solution and light phase after centrifugation.* ***(B)*** *Plot showing the light phase concentration at each total concentration of RABV P measured by FIDA.*

After centrifugation, the light phase, although well above the critical concentration at this temperature, failed to induce phase separation; even when reincubated in the same conditions than the one in which we initially induced phase separation (High protein concentration, 120mM NaCl, high temperature).

We hypothesized that this unexpected behavior could originate from the presence of an unrecognized contaminant that allowed the phase separation to be induced, would be concentrated in the coacervate and would thus disappear from the diluted phase. Although all our protein purification steps and experiments were performed in the presence of a reducing agent (1mM TCEP), we suspected that P could form intermolecular disulfide bridges, or would be post-transcriptionally modified. We also suspected possible changes in pH or salt concentration (NaCl) (sedimentation of ions with the protein in the dense phase).

Therefore, we spent time exploring several hypotheses in order to find an explanation; we performed among other tests electrospray mass spectrometry (**Figure, 28**) to assess the presence of post-translational modifications in $P_{FL}$. Results revealed an average molecular mass of 34,056.0 ± 1 Da in perfect agreement with the calculated average molecular mass for a full-length protein lacking its N-terminal methionine (34,187.4603 – 131.1986 (Met) = 34,056.2617 Da) which eliminated this hypotheses.

# 1. Nucleoprotein and Phosphoprotein LLPS assays

## (a) P and N interact but do not form LLPS in vitro

In the following part, I will describe some preliminary experiments, which need to be reproduced and improved. , when N is mentioned alone, it refers to the cleaved $N_0$-$P_{68}$ complex, and $P_{LLPS}$ refers to a solution of P, which undergoes liquid-liquid phase separation.

We have tested the ability of mixtures of both $N_0$-$P_{68}$ complex and P to induce liquid-liquid phase separation together, or with other partners. For that, we tested several conditions:

A. Upon addition of $N_0$-$P_{68}$ complex to a florescent $P_{LLPS}$ (120 mM NaCl, room temperature), the turbidity of the solution disappeared, suggesting that N and P interacts (**Figure, 41A**) but in these conditions did not induce LLPS.

B. Under condition where P alone did not induce LLPS (4°C or 200mM NaCl), the addition of the nucleoprotein to the phosphoprotein did not cause any turbidity or appearance of droplets (**Figure, 41B**). Light scattering measurements did not show any drop in absorbance, upon addition of P to N in the tube.

C. When fluorescently labelled polyA RNA was added at different concentrations to a solution of non-fluorescent P (not phase separating), it induces droplets formation

(**Figure, 41C**). Fluorescence inside the droplets indicates the concentration of RNA with P in the droplets.

D. After addition of N to this P-RNA$_{LLPS}$ turbid solution (sample from C), the droplets started to disappear (**Figure, 41D**).

E. Upon addition of fluorescent peptide P$_{68}$ (68 first aa of phosphoprotein) to P$_{LLPS}$ turbid solution, the fluorescence appeared to concentrate into the droplets, showing that the peptide penetrates inside the droplets. (**Figure, 41E**).

F. On the other hand, by using N-mcherry and non-fluorescent P$_{LLPS}$ in solution we could not see any red fluorescence inside the droplets after adding both proteins to the solution (**Figure, 41F**).

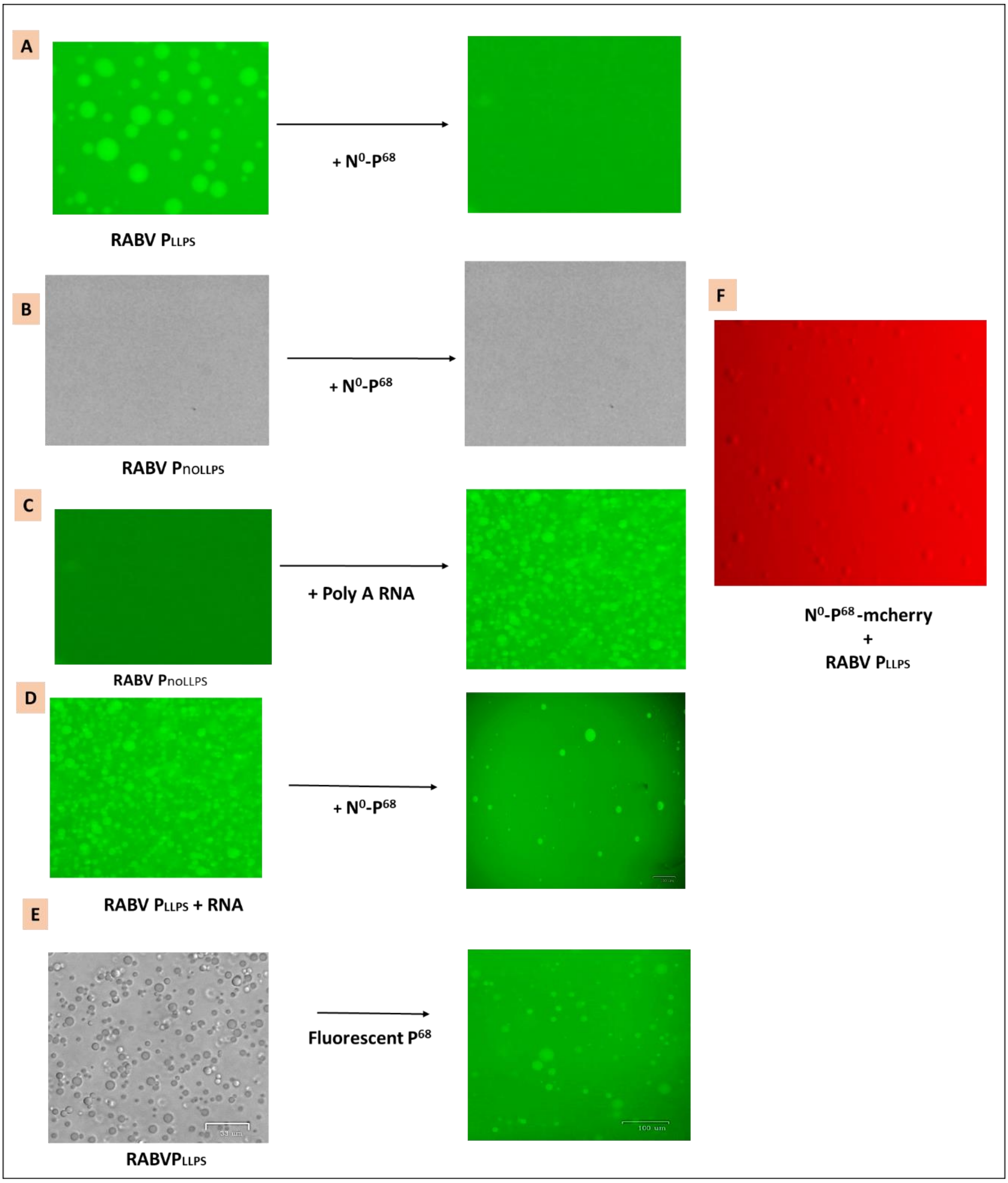

*Figure 41. Appearance and disappearance of liquid droplets apon addition of proteins and RNA using fluorescent molecules*

To summarize, we did not succeed inducing phase separation in the presence of N and P in the solution, even in the presence of RNA (solution containing rings).

### (b) Deuterated RABV P and effect of $D_2O$ in LLPS

We performed a preliminary experiment with the sample of $P_D$ (85% deuteration), but could not find conditions where LLPS occurred in buffer containing 100% $D_2O$. By contrast, using the same protein we were able to induce LLPS in a buffer made with 100% H2O (120mM NaCl at 20°C). Some of these samples were used in the SANS experiments. Deuteration and $D_2O$ buffer effect can modify the solution behavior of the protein. Our results show that the LLPS phenomenon induced by RABV P depends on various electrostatic and other inter and intra-molecular interactions. Differences between hydrogen and deuterium include differences in bond lengths and polarizability (which could modify the strength of H-bonds and van der Waals interactions). However, $P_D$ used in our project was produced 15 years ago, and thus this experiment may not be indicative.

### (c) Preliminary data of P+N with SANS:

To observe the interactions at the bio macromolecular level, we used SANS on the mixture of P and $N^0$-$P_{68\text{-mCherry}}$, varying $H_2O/D_2O$ ratio to match out selectively the hydrogenated N (matched-out at 42 % $D_2O$) or $P_D$ (matched-out at 100 % $D_2O$). We used same molarity of P and N in the solution: 200uM (6 mg/mL for P and 3.6 mg/mL for N). As a reference, we measured the $P_D$ alone in 100% $H_2O$ (under conditions where it undergoes LLPS). This is necessary to check whether deuteration of the protein has an effect on the protein conformation. We also prepared samples of $P_D$ in $D_2O$ but the sample was aggregated; we did not investigate further whether this is due to an isotopic solvent effect or was simply a fluke. Both experiments were set up in 130mM ionic strength.

The Figure (**Figure, 42**) shows a big difference of scattering between $P_D$, which makes LLPS in $H_2O$ and the complex $P_D$ + N-mCherry in 42 % $D_2O$, the intensity of $P_D$ alone, is 16 times more important than P in the complex.
When we consider the difference due to the concentration of P between both samples (x2) and the one due to the contrast between $D_2O$ and $H_2O$ ($x2^2$), there is still a factor 2 remaining, which might come from the presence of bigger species in the solution of P alone, as also seen from the shape of the curve (steep increase at low q for P alone, close to a plateau for P in the

mixture) and consequently the $R_g$.

P and N are clearly interacting, and the GUINIER region of the complex curve indicates an $R_g$ for the complex P+N at least 2 times smaller ($R_g$ = 12 ± 1.9 nm ) than the $R_g$ of P alone ($R_g$ = 21 ± 1.2 nm), which confirm smaller forms present in the solution.

The macroscopic scale confirms what is observed visually at the microscopic scale. Since N causes the droplets to dissolve by visual observation.

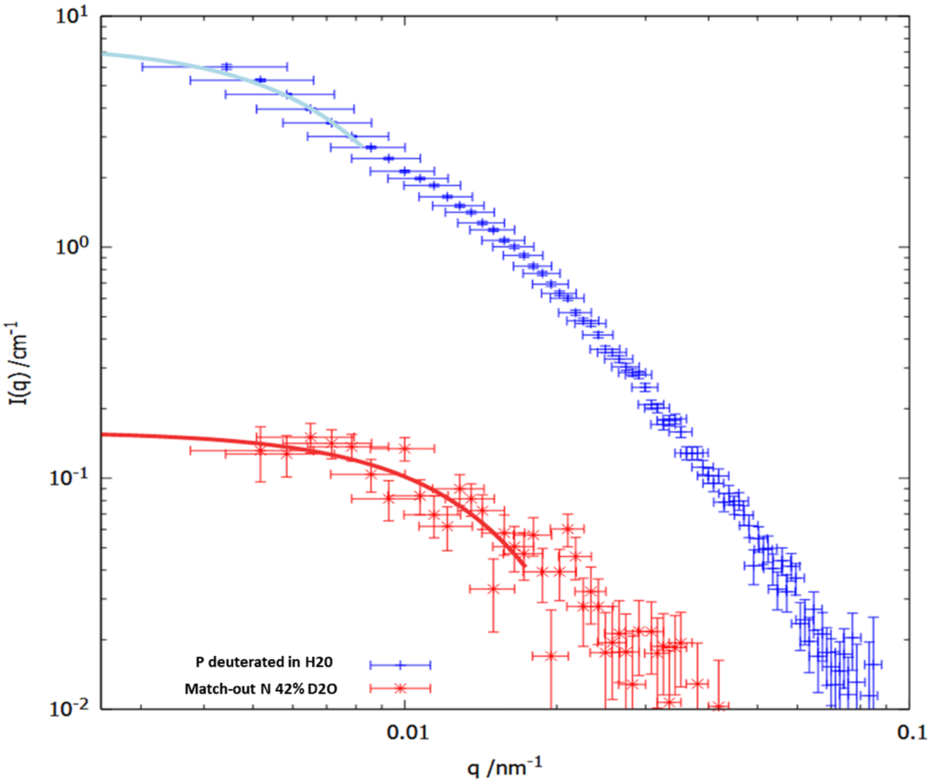

*Figure 42. SANS intensity plot of $P_D$ in 100% H20, compared to $P_D$ complexed with $N^0$-P68 in 42% D20. Lines correspond to the Guinier fit region*

However, these results can be used as a template for the rest of the project, but should be taken with caution because the P protein was produced several years ago. Even if it has been frozen at very low temperatures, we know the importance of fresh production of protein in the reproducibility and proper functioning of the experiments. P proved to be very responsive to several factor such as temperature or concentration.

# IV. Discussion

Our initial hypothesis was that phase separation would be induced by the mixing of RABV phosphoprotein (P) and nucleoprotein (N). However, we discovered that RABV P alone was able to induce reversible phase separation alone. We found that the transition depends on salt concentration, temperature and protein concentration, and we showed that $P_{\Delta MD}$ was unable to induce phase separation at least in similar conditions. This last result confirmed results obtained in cultured cells demonstrating that the dimerization domain is essential for the phase separation process of RABV P (Nikolic et al., 2017b).

In the meantime, the GAUDIN group in Paris had shown that RABV P could induce phase separation in aqueous solution but in the presence of 5% PEG (Nevers et al., 2022) . They used fairly similar salt concentration and slightly lower protein concentrations in agreement with the action of PEG as a crowding agent that increases the apparent protein concentration.

The novelties in our study are: (1) the dependence on temperature. We clearly demonstrated that the phase separation induced by RABV P is thermosensitive and is characterized by an LCST. This has consequences on the mechanism and forces involved in this process.

(2) The fine-tuning of the process by ionic strength (salt concentration). We showed that phase separation is induced in a rather limited range of ionic strength. At low (< 50 mM) or high (>150 mM), the phase separation did not occurred, at least in the protein concentration range that we used. This is also giving indications about the forces involved.

RABV P is a negatively charged protein with different distribution of charges (**Figure, 43**)

- **N-terminal domain $P_{NTD}$ (1-86 AA):** Highly acidic, and contain intrinsically disordered domain with a global negative charge (-13).

- **dimerization domain $P_{\Delta MD}$** (91-132) : The core of $P_{MD}$ has a neutral charge, and represent the template from which emerges the $P_{NTD}$ and $P_{CTD}$

- **C-terminal domain $P_{CTD}$ (188-297AA)** consisting of two folded domains, positively charged (+3) with an asymmetric distribution of positive and negative charges on the surface.

-

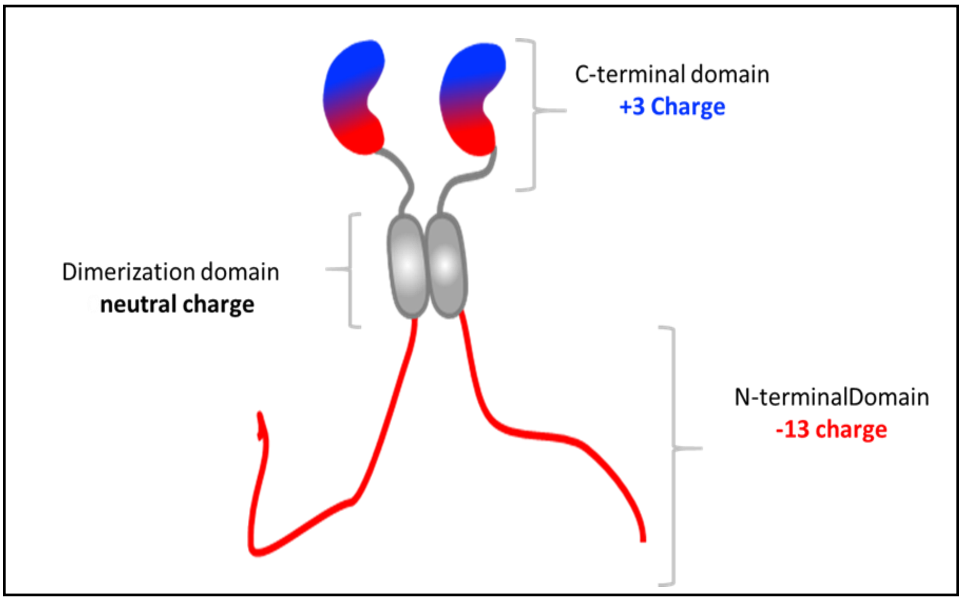

Figure 43. Schematic representation of the structure of RABV phosphoprotein with distribution of charges

The ampholytic properties of RABV P and the tight controls of LLPS by ionic strength, suggests that electrostatic interactions play a key role in the assembly of soluble complex and in triggering the LLPS and the formation of droplets in our system. Starting from a free dimer, different models of RABV P can be proposed according to the conditions of ionic strength:

At low ionic strength, the protein is globally negatively charged and repulsive electrostatic interactions prevent the phase separation, although they do not prevent the formation of soluble complexes. The simplest option that can be envisioned is the following: In the absence of medium-range electrostatic screening, the long-range repulsive forces between identically charged dimers takes over.

At high salt concentration or in diluted solution, the protein is simply a free dimer (State $A_0$) in the solution (**Figure, 44**); when decreasing ionic strength, at intermediate salt concentrations, the increase in oligomeric mass is due to dominant electrostatic attractions. Certain interactions seem to be favored, inter-molecular between a P dimer and its neighbor or intra-molecular bonds within a dimer itself. Indeed this hypothesis is supported by the fact that the C-terminal and the N-terminal of a monomer have an opposite charges (**Figure, 43**). These inter-molecular interactions between different molecules of P end up forming larger clusters in the solution, which coexist with other forms ($A_0$, $A_{S\text{-}N}$ or $A_{S\text{-}S}$) at different proportions (**Figure, 44**). However, these larger forms are not sufficient to drive LLPS since in the absence of salt bigger forms are present, but the solution does not undergoe phase separation.

Above 200mM of NaCl, the protein is a dimer and interactions do not evolve anymore. Salt seems to therefore play a screening role against attractive electrostatic interaction, which prevents the coacervation. Only in an intermediate range of ionic strength are the intermolecular or intramolecular interactions tuned for allowing the coacervation.

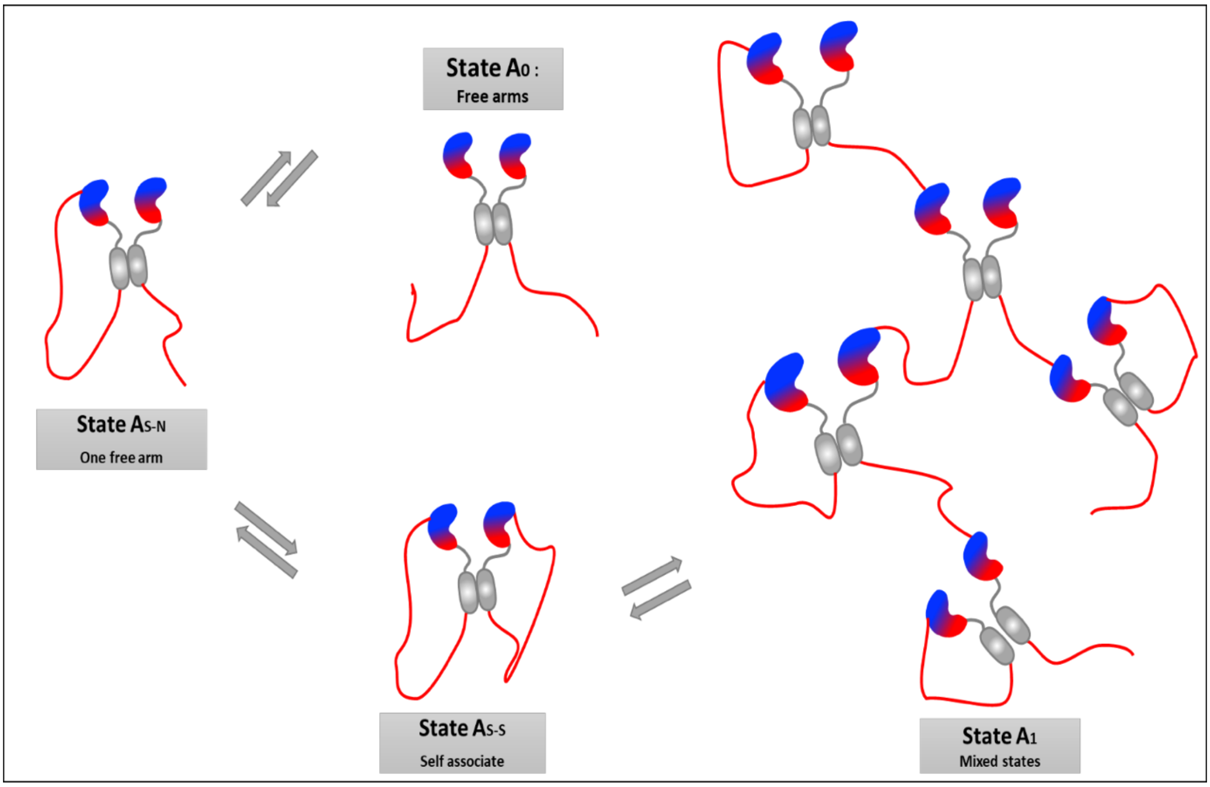

Figure 44. Proposed models and conformations of RAVB P

To explain an LCST behavior we can consider that some segments of the protein are cooperatively hydrated. Increasing the temperature induces the release of these water molecules, which favors interactions. The mechanism of the phase diagram does not follow a simple binary model, but probably a nucleation-condensation model starting from the dimer of P. However, to find explanation on why the diluted phase after centrifugation failed to trigger phase separation even above the critical temperature and concentration suggests that the mechanism is more complicated. In the diluted phase, the two scattering decays observed using USAXS and SAXS at two different length scales (Article, **Figure, 9**) could originate from two different populations of particles or from one populations of larger clusters composed of the small complexes. For the dense phase, Rg (8 times bigger than Rg of the light phase) shows that the volume can be 450 times bigger in the coacervate than the upper phase, so maybe forms allowing phase separation get trapped in the gel (dense phase).

During phase separation, one could imagine that arms of P are involved in interactions with other P partners, thus less free arms are available to allow new interactions, which blocks the interaction of the whole cluster, and stabilizes the droplet by preventing it from growing further. P can also exist in a form that blocks itself by making a self-association (As-s form), which prevent further interaction with neighbors.

This would be an interesting path to explore, in order to better understand the cluster composition in the liquid phase. Transferring the light phase sample after centrifugation from 120mM NaCl ( 130mM ionic strength) to a very low salt concentration would allow us to see if we revert to a dimer in solution or not.

We could not find conditions where LLPS occurred, in buffer containing 100% $D_2O$. Deuteration and $D_2O$ buffer can modify the solution behavior of the protein, the difference between hydrogen and deuterium include difference in bond lengths, and polarizability (which could play on H-bonds and Van der Waals interactions). We demonstrated that ionic strength determines the coexistence line or binodal and control LLPS through different interactions, which might explain why deuteration prevent LLPS to occur and how charged molecules like RNA or peptides can enter the liquid droplets during phase separation.

More elaborate neutron experiments with $P_D$ and nucleoprotein are planned for the future of the project; they will provide a better understanding of the effect of deuteration on P and on the P+N interaction in phase separation conditions.

# V. Materiel and methods

Proteins used in this work were produced using two different protein production systems. The phosphoprotein constructions including the full-length protein and PΔ91-131 ($P_{MD}$) were produced using a prokaryotic system (*E. coli*), while $N_0$-$P_{68}$ and $N_0$-$P_{68}$-mCherry were produced using a (baculovirus/insect cells) system.

## 1. Expression and purification of proteins

- ***RABV P constructs:***

We started by expressing RABV P protein using a bacterial expression system. The DNA coding for the protein was inserted into an expression plasmid (pET22b) (containing the full-length gene with a His-Tag at its C-terminal end), NdeI restriction site and a methionine codon were introduced downstream of the coding sequence and an XhoI restriction site was introduced up stream. The PCR product were cloned into pET22b between the NdeI and XhoI sites, thus introducing a His6-tag at the C-terminal extremity of the coding sequence. The constructions were verified by DNA sequencing.

The plasmid was then transformed into a bacterial cell (*E. coli* BL21 DE3). The bacteria were grown at 37°C in LB containing 100µg/mL ampicillin until the O.D. at 600 nm reached 0.6-0.8 and were subsequently induced with 500µM IPTG and incubated overnight at 18C. The pellets were collected by centrifugation at 4000 rpm (JLA8.1) at 4 C for 20 minutes. The supernatant was obtained by centrifuging at 18 000 rpm (JA25-50) for 45 minutes at 4°C.

Pellets were suspended in lysis buffer [20 mM Tris-HCl pH 7.5, 200 mM NaCl, 0.2 mM TCEP,5 mM imidazole] supplemented by EDTA-free complete protease inhibitor and lysed by sonication the sample on ice using three 5-second bursts at 70 intensity and let the mixture cool down for 5 seconds on ice between each burst. Lysate was then cleared from debris by centrifugation (6000g for 40 min),

The supernatant was than purified in two steps, first by affinity chromatography on a nickel (Ni2+) column, using the 6-histidine tag at C terminus of the RABV P, and second by size exclusion chromatography (SEC). The supernatant was incubated with Ni-NTA agarose Qiagen, equilibrated in buffer A (20 mM tris-HCl pH 7.5, 200 mM NaCl, 0,2 mM TCEP) and washed extensively with buffer B (20 mM Tris-HCl pH 7.5, 200 mM NaCl, 0.2 mM TCEP, 10 mM imidazole). Buffer C (20 mM Tris-HCl pH 7.5, 200 mM NaCl, 0.2 mM TCEP, and 250 mM imidazole) eluted the protein. In order to verify the purity of the sample, and the absence of contaminant; the purified sample was loaded on an SDS-PAGE under denaturing conditions, then loaded into a size exclusion chromatography, without concentration. The final concentration and molecular mass of proteins were measure by SEC-MALLS. $P_{MD}$ was produced and purified following the same protocol as $P_{FL}$.

- ***RABV $N_0$-$P_{68}$ proteins:***

Eukaryotic baculovirus-insect cell (baculo) expression system was used to produce the rabies virus $N_0$-$P_{68}$ complex and $N_0$-$P_{68}$- mCherry. Prior to expression in cells, a recombinant baculovirus is generated containing the gene coding for the protein of interest. The elaboration of the recombinant baculovirus requires the subcloning of the gene coding for the protein of interest in an "acceptor" vector, pFastBacHTA. This vector has a multiple cloning site (MCS) where the gene of interest is inserted as well as transposition elements (Tn7L, Tn7R). These elements allow its insertion by transposition into the genome of E. coli DH10EMBacY bacteria composed of the DNA of the baculovirus known as bacmid possessing the same transposition elements as well as a helper plasmid coding for a transposase. The transformation of the acceptor plasmid into DH10EMBacY allows the transposition of the gene of interest within the bacmid. After transposition, cells containing the bacmid coding for the protein of interest are discriminated by blue/white screening. Successful transposition of Tn7 results in the loss of α-complementation of β-galactosidase. Therefore, colonies with correct Tn7 transposition remain white on selective agar plates containing X-gal. The bacmid is then purified by alkaline lysis and ethanol/isopropanol precipitation.

This bacmid is then transfected into Sf21 insect cells. The EMBacY bacmid also contains an expression cassette for the fluorescent protein YFP allowing the monitoring of viral titers by fluorescence reading. The supernatant containing baculoviruses is collected 48h to 60h after transfection and constitutes the $V_0$ virus (high quality virus but low viral titer) which will be amplified to generate baculoviruses with high viral titer. These viruses are then used for larger scale production in Sf21 or Hi5 cells at low MOI. The cells will be collected 48 to 72h after infection by centrifugation at 1000g. The cell pellets are stored at -20°C before being lysed.

Pellets were suspended in lysis buffer [20 mM Tris-HCl pH 7.5, 150 mM NaCl, 0.2 mM TCEP,5 mM imidazole] supplemented by EDTA-free complete protease inhibitor and lysed. Lysate was cleared from debris by centrifugation (6000g for 40 min), and the cleared supernatant was incubated with Ni-NTA agarose Qiagen, equilibrated in buffer A (20 mM tris-HCl pH 7.5, 200 mM NaCl, 0,2 mM TCEP) and washed extensively with buffer B (20 mM Tris-HCl pH 7.5, 200 mM NaCl, 0.2 mM TCEP,10 mM imidazole). Buffer C (20 mM Tris-HCl pH 7.5, 200 mM NaCl, 0.2 mM TCEP, and 250 mM imidazole) eluted the protein. In order to verify the purity of the sample, and the absence of contaminant; the purified sample was loaded on an SDS-PAGE under denaturing conditions. $N_0$-$P_{68}$ was then cleaved using TEV by shaking overnight, then loaded into a size-exclusion chromatography to separate nucleoprotein from the peptide $P_{68.}$ The final concentration and molecular mass of the protein was measured by SEC-MALLS.

- ***RABV P-FAM Maleimide labeling:***

The reaction of thiols with maleimides is a widely used process for conjugating and labeling biomolecules, including proteins and peptides. The reaction proceeds according to the following scheme:

*Figure 45. Scheme of thiols reaction with maleimides*

Maleimides are electrophilic compounds that selectively react with thiols. Thiols are found in proteins and peptides as cysteine residues and can also be incorporated into synthetic oligonucleotides. In our experiment, P protein has a cysteine in the C-terminal domain. However, thiols are prone to oxidative dimerization, leading to the formation of disulfide bonds, which stabilize protein tertiary structures. Therefore, it is necessary to reduce disulfide bonds prior to conjugation, and to exclude oxygen from the reaction.

For the conjugation, we used the following protocol:

We Dissolved P protein at concentration around 1mg/mL in degassed buffer by inert gas (20 mM Tris-HCl PH=7.5, 200mM NaCl). Then we add an excess of TCEP (tris-carboxyethylphosphine) reagent to reduce disulfide bonds (X10), flush with inert gas, and close. The dye was then added to the thiol solution (15x fold excess of dye), and left agitating overnight at 4°C, then size exclusion chromatography and concentration by centrifugation were used to eliminate the excess of dye in P solution.

## 2. Protein characterization methods:

### (a) Electrophoresis gel under denaturing conditions:

The SDS is a compound capable of binding to the periphery of protein chains to give them a negative charge. Thus, the proteins covered by SDS will have a negative charge, Influenced by the SDS, they will all migrate along the gel. 12 and 15% denaturing electrophoresis gels (SDS-PAGE) with Tris-Glycine (TG) buffer were used to analyze the fractions containing the different proteins. Protein detection was performed by Coomassie blue staining.

### (b) Absorbance spectroscopy

The concentration of the protein solutions was determined by measuring the absorbance spectrum. The molar extinction coefficient at 280 nm of the proteins is calculated from their 62content of Trp, Tyr, and Cys residues using the molar extinction coefficient of these residues at this wavelength (Pace & al., 1995). For a given wavelength, the absorbance ***A*** of a dilute solution of concentration C is given by the Beer-lambert method:

$$A = \varepsilon . l . C$$

$\varepsilon$= the molar extinction coefficient

$l$= the length of the light path in the considered medium

C = Concentration of the adsorbing chemical entity.

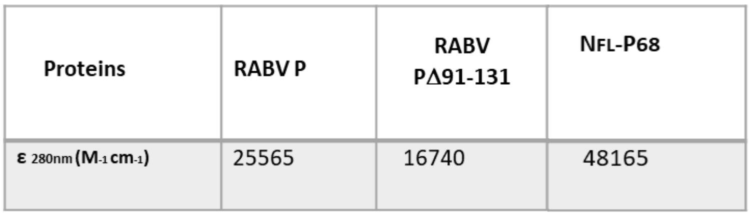

| **Proteins** | **RABV P** | **RABV PΔ91-131** | **NFL-P68** |
|---|---|---|---|
| **$\varepsilon_{280nm}$ ($M^{-1} cm^{-1}$)** | 25565 | 16740 | 48165 |

**Table.** Summary of the molar extinction c studied

The measurement of light scattering at 350nm was used to monitor the appearance of turbidity in the protein solution, which undergoes liquid-liquid phase separation.

### (c) Size exclusion chromatography (SEC)

- Introduction:

Size exclusion chromatography (SEC) uses gel filtration to separate molecules according to their size. The gel consists of spherical beads containing pores of a specific size distribution. Separation occurs when molecules of different sizes are trapped or excluded from pores within the matrix. Small molecules diffuse into the pores and their flow through the column is delayed according to their size, while large molecules do not enter the pores but are eluted into the column dead volume (**Figure, 46**). Thus, molecules are separated according to their size as they pass through the column and elute in descending order of molecular mass (MM).

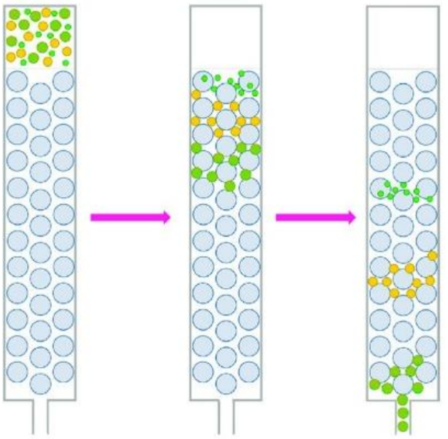

*Figure 46.Principle of size-exclusion chromatography (Majeed et al., 2020)*

- Experiment:

For our experiments, the SEC column was equilibrated overnight in buffer A (20 mM Tris pH = 7.5, 200 mM NaCl, 0.2 mM TCEP), $P_{FL}$ Protein was loaded into a BIG S200 26/600 Superdex (GE Healthcare) column without previous concentration, whereas for the rest of the proteins S200 16/600 Superdex column was used. Fractions were then pooled, concentrated, and leaded into a 15% SDS-page gel to verify the purity.

### (d) **Size exclusion chromatography coupled with multi-angle laser light scattering and refractometry**

- Introduction :

The size exclusion chromatography (SEC) technique coupled with multi-angle laser light scattering (MALLS) and refractometry (RI) (SEC-MALLS-RI) provides an absolute measurement of the molecular mass of particles. In addition, by calibrating the Size exclusion Chromatography (SEC) column with proteins of known hydrodynamic radius (Uversky, 1993), this technique also provides a measurement of the hydrodynamic radius of the particles.

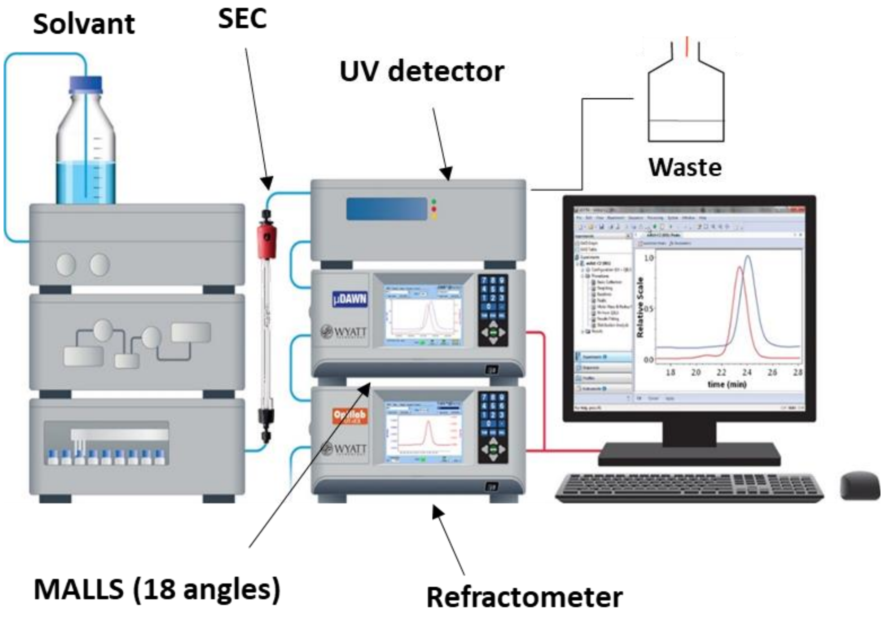

*Figure 47.MALLS system*

The intensity of scattered light that a macromolecule produces is proportional to the product of the weight-average molar mass and the concentration of the macromolecule.

$$Is,q\sim Mw.C$$

Combining Size Exclusion Chromatography with on-line detection by light scattering allow to use the column as a filter, which can separate different components present in the sample according to the elution volume and thus, facilitate the measurement the homogeneity and the disparity of the samples.

Separation is based on the molecular mass, larger species elute at the head of the peak and smaller species elute at the end of the peak (**Figure, 48**). The molecular mass of a polydisperse species varies across the peak, whereas for a mono-disperse species it remains invariable

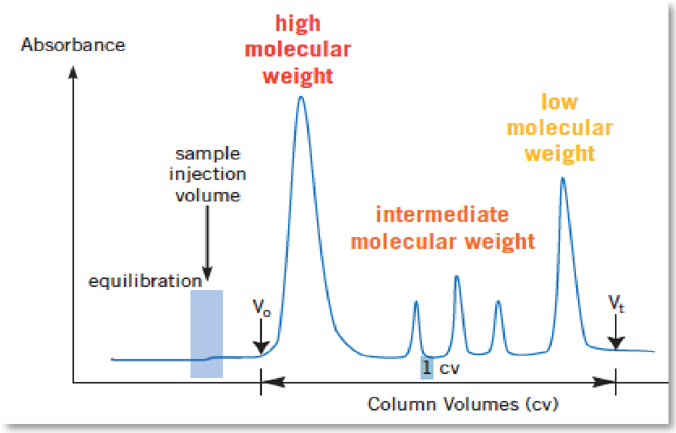

*Figure 48. SEC elution volumes based on the molecular mass*

MALLS measures the time-average intensity (Static Light Scattering – SLS) of scattered light at each angle detected. The intensity of light scattering of a solution is directly proportional to the average molecular mass and to the concentration of its components.

The RI detector measures the difference of refractive index between sample and reference:

$$\boxed{\Delta LS} = \left(\frac{I_\theta}{I_0}\right)_{\text{solution}} - \left(\frac{I_\theta}{I_0}\right)_{\text{buffer}} = K(\mathrm{dn}/\mathrm{dc})^2 \boxed{M_W}\boxed{C}$$

$$DRI = n_s - n_r = (dn/dc).\ C$$

- Experiment :

The data were analyzed with ASTRA V software (Wyatt Technology Corp.). Measurements were made with different columns S200 10/300 increase (GE Healthcare), at 20°C and 4°C using 20 mM Tris-HCl, 150mM/200mM NaCl, pH 7.5, and 0.5mM TCEP buffer.
The calibration were performed using known concentration and molecular mass of bovine serum albumin (BSA) protein. Samples of 50µL were injected at concentrations ranging from 0.5 to 10 mg/mL and MALLS detection was done with a DAWN-EOS detector using a laser emitting 690 nm. The analysis of data and weight averaged molar masses (MM) were calculated using ASTRA software (Wyatt Technology Corp., Santa Barbara, CA).

### (e) Mass spectrometry

Mass spectrometry is a sensitive technique used to detect, and quantify different molecules based on their mass-to-charge ratio (m/z). It helps determine the protein structure, function and folding, moreover, it can identify a possible post-translational modification such as methylation, disulfide bridging or a loss of one or more amino acids.
The molecular massdetermination of intact RABV P protein has been carried via ESI mass spectrometry by the proteomics Core Facility at EMBL Heidelberg, Germany.

### (f) Small angle X-RAY/neutrons scattering

- Introduction :

Small-angle scattering is a structural characterization tool for materials used to determine the structure of particle systems based on average particle size or shape. Materials can be solid or liquid. X-rays, it remains one of the most used methods for structural characterization, which can be performed on solids, liquids, gases, amorphous, crystalline or almost any type of device. SAXS and SANS are extremely useful in polymer and colloid science because they measure size scales (1-1000 nm.). In addition, both SANS and SAXS are useful for the following reasons:

- Information about the size, shape, and spatial relationship of the analyte can be resolved.
- With sufficiently large neutron and x-ray beams, information can be obtained in real time. Thus, it is possible to measure the size, shape and spatial association of macromolecules and

assemblies by changing different experimental conditions (such as temperature, pH and salinity).

## Neutrons:

Neutrons are subatomic particles that have no electrical charge, unlike other particles such as protons and electrons that have an internal electrical charge. This difference makes neutron-matter interactions particularly interesting compared to proton-matter or electron-matter interactions. Uncharged neutrons can travel through matter and penetrate matter more deeply than other subatomic particles.

## Where Do the Neutrons Come From?

Currently, there are approximately 30 active neutron research facilities scattered around the world, including the Institut Laue-Langevin (ILL) high-flux reactor, which operates continuously in 50-day cycles. It typically operates in four 50-day cycles per year, providing researchers with 200 days of peak time. Each facility has facilities for the production of thermal neutrons for experimental research. These neutrons are usually produced either in research reactors specially designed to release neutrons or by a process known as spallation.

## Fission process:

The nucleus, usually uranium 235 or Pu-239, captures a neutron and then decays into fragments, including neutrons with kinetic energy, beta radiation and photons. Each fission reaction produces an average of 2.5 neutrons (Weinherg, 1959) one of which is used to accelerate further fission, half of which are produced with a delay and the instructions necessary for the reactor and the latter actually collected for an experimental study. The large thermal neutron flux of ILL produces approximately 1.5.1015 neutrons per cm2 per second

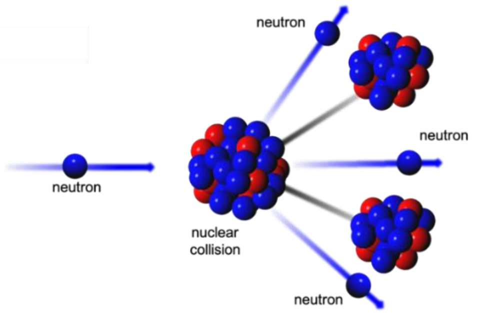

Elena-neutron

## Spallation process:

As an alternative to using research reactors, some neutron research facilities with high-powered particle accelerators can produce neutrons in a process called nuclear spalling. Here, accelerated high-energy protons are directed at a dense, high-mass target such as tungsten, uranium, tantalum or mercury, and the collision leaves the target's nuclei in a highly excited state. The products of this interaction include various high-energy neutrons and protons that collide with other, still unexcited target nuclei, as well as low-energy evaporation neutrons (Weisskopf, 1937) that is finally collected for scattered experiments. In terms of yield, an average of 20 neutrons are produced from each proton-target nucleocollision (Weinherg, 1959), most of which are variable.

For neutron production in both research reactors and spallation, there is still too much energy for instantaneous low-energy neutrons for practical experimental use. Thus, a moderate step is required to slow them down into so-called thermal neutrons. This usually involves surrounding the neutron source with a large amount of a suitable moderator such as heavy water, water or beryllium (Lamarsh & Melkonian, 1977)in which fast neutrons enter and gradually lose their energy in a series of collisions with moderating nuclei.

It is worth mentioning that many neutron research facilities today also have cold neutron sources that use liquid hydrogen as a moderator, which allows neutrons to be cooled to cryogenic temperatures for sub-temperature experiments. After dozens of collisions with a neutron (Lamarsh & Melkonian, 1977), the resulting thermal neutrons leak from the moderator through a dedicated radiation tube and are ready for use in propagation experiments.

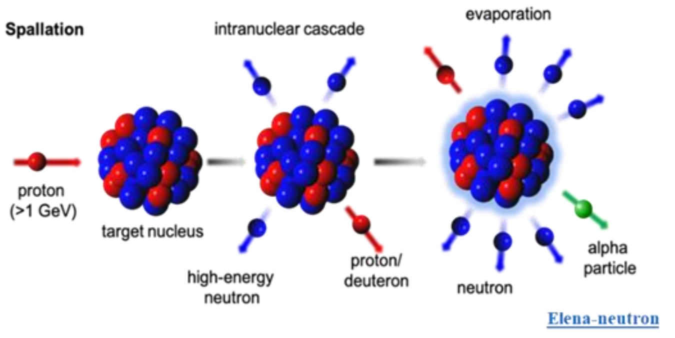

## X-rays:

X-rays are electro-magnetic waves just like “ordinary “visible light, with a much shorter wavelength (< 0.3 nm). The wave propagate, because an alternating electric field (E) cause an alternating magnetic field (H) and vice versa.

When X-ray interacts with matter, we speak about two main type of interaction, absorption and scattering. Upon encounter of X-rays with a material, a part will be absorbed which occurs at all wavelengths at with various efficiencies. The absorbed fraction is converted into other forms of energy (heat, fluorescence radiation…etc.) and the second part will be scattered into other directions and propagations.

## Where Do X-ray Come From?

X-rays are usually produced in x-ray tubes by accelerating electrons through a potential difference (voltage drop) and directing them into a target material (ie tungsten). Synchrotrons and storage rings are commonly used as X-ray sources worldwide. A synchrotron is a very powerful source of X-rays, where high-energy electrons orbit the synchrotron to produce X-rays. Its purpose is to accelerate the electrons to a very high energy and make them change direction periodically. The resulting X-rays are emitted as dozens of thin beams, each directed toward the beamline closest to the accelerator. The machine works day and night, with short and long maintenance at regular intervals. The European Synchrotron Radiation Facility (ESRF) is the most powerful light source produced by synchrotrons, producing X-rays 100 billion times brighter than X-rays used in hospitals. At the ESRF, these x-rays with exceptional properties produce high-energy electrons that orbit the storage ring, a circular tunnel with a circumference of 8 meters. Two types of X-rays are produced: characteristic radiation and bremsstrahlung radiation.

## Characteristic X-ray generation

Pictured: When a high-energy electron, collides with an inner shell electron, both are ejected from the tungsten atom, leaving a "hole" in the inner shell. It is filled with an outer shell electron, whose energy loss is emitted as an X-ray photon.

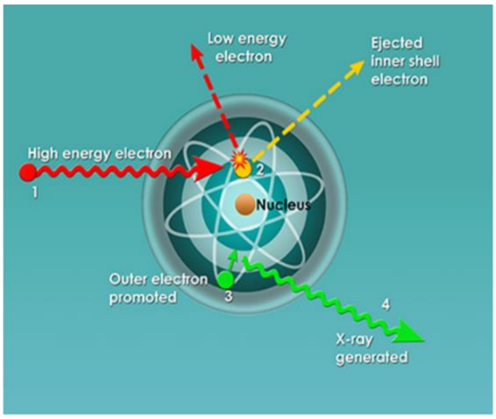

Dr Graham Lloyd-Jones

## Bremsstrahlung/Braking X-ray generation

When an electron passes near the nucleus, it slows down and its path deviates. The lost energy is released as bremsstrahlung X-ray photons. About 80% of the X-rays in the X-ray system are X-rays produced in this way.

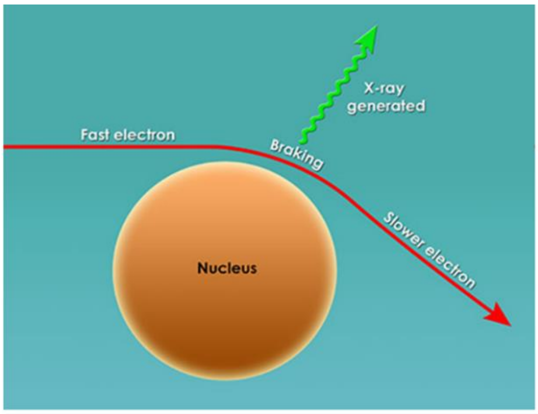

Dr Graham Lloyd-Jones

- **Experiment :**

**SAS beams times:**

## Small angle neutron scattering (SANS) D11:

SANS data were acquired on the SANS instrument D11 at the ILL, on a multi-tube ^3He detector, at up to 3 configurations, with sample-to-detector distances (and collimation distances) of 1.7 m (2.5 m), 10.5 m (10.5 m) and 20.5 m (20.5 m) at a fixed wavelength of 6.0 A (relative fwhm 10 %), covering a maximum q-range of $2e^{-3}$ to $5e^{-1}$ $A^{-1.}$ Samples were measured in a thermalized Peltier sample-changer at varying temperatures between 4 and 20 °C. Data were analyzed using Primus, JScatter and SAS plot software.

## Small angle X-ray scattering (SAXS) BM29:

SAXS data were performed on the BM29 BioSAXS beamline at ESRF, at 1 configuration with sample-to-detector ( Pilatus 3 2M detector) distances of 2.87m using a sample environment quartz glass capillary of 1mm diameter, covering a q-range of 0.025-6 $nm^{-1}$ . Samples were filed in a 500uL tubes and stored in an automated sample changer allowing temperature variations (from 4 to 60°C).

For temperature measurement, sample changer were kept at 4°C for the storage of proteins, but the capillary were thermalized at the wished temperature

## Time-Resolved Ultra Small-Angle X-Ray Scattering (USAXS) ID02:

USAXS data were performed on the ID02 beamline at ESRF, at 3 configuration with sample-to-detector (Eiger detector) distances of 0.8m, 10m and 30.5m. The beamline is optimised for experiments using a fixed wavelength around 0.1 nm (12.2 keV), covering a q-range (0.001 $nm^{-1}$ to 50 $nm^{-1}$). Samples were loaded in a 1mm, 2 mm capillaries, measurement were done at room temperature, and data were analyzed using SAXS utilities software.

### Size exclusion chromatography combined with small angle X-ray scattering (SEC-SAXS)

SEC-SAXS was performed at the BioSAXS beamline (SWING) of the Synchrotron Soleil, Paris with a sample to detector distance of 2m (EigerX4M detector ). The beamline is optimized for experiments using a fixed wavelength around 0.1 nm (16 keV) covering q range (0.0032–0.52 A $^{-1}$).

Samples were analyzed on a Superdex Increase 200 5/150 GL (Cytiva). The scattering from the buffer alone was measured before each sample measurement and used for background subtraction. SAXS data reduction to sample solvent scattering, were made using Foxtrot (SOLEIL software). All data analyses were performed using the program PRIMUS from the ATSAS package (Emsley & Cowtan, 2004).

## (g) Flow-induced dispersion analysis (FIDA)

- Introduction:

The FIDA instrument (flow-induced dispersion analysis) consists of a temperature-controlled tray within a sample-handling robot that can be maintained above any temperature, and samples are loaded into capillaries stored in a temperature-controlled chamber.

Different mode of operation can be used for FIDA : Standard Capflex (i.e. slow continuous injection of sample), rapid filling of the capillary followed by slow continued injection of the sample for the study of LLPS kinetics for example or a standard FIDA for affinity determination.

For the standard Capflex experiment, the method measures fluorescence compatible with the Alexa488 dye, the labeled protein concentration represents less than 1% of the total protein in the sample.

When injected into a capillary, a sample undergoing LLPS reaches the detector after a flow- and pressure-controlled time delay; signal peaks are then recorded as each droplet passes in front of the light beam (**Figure, 49**). The baseline intensity level of the signal allows determination of protein concentration in the light/dilute phase (Poulsen et al., 2015).

It is necessary to perform a standard curve calibration to extrapolate the dilute phase concentrations. Generally, a known set of increasing protein concentrations with a constant proportion of labeled protein can be injected into the capillary while making sure the sample is not phase separated. This can be achieved by using a concentration range lower than the critical concentration of the protein (Stender et al., 2021).

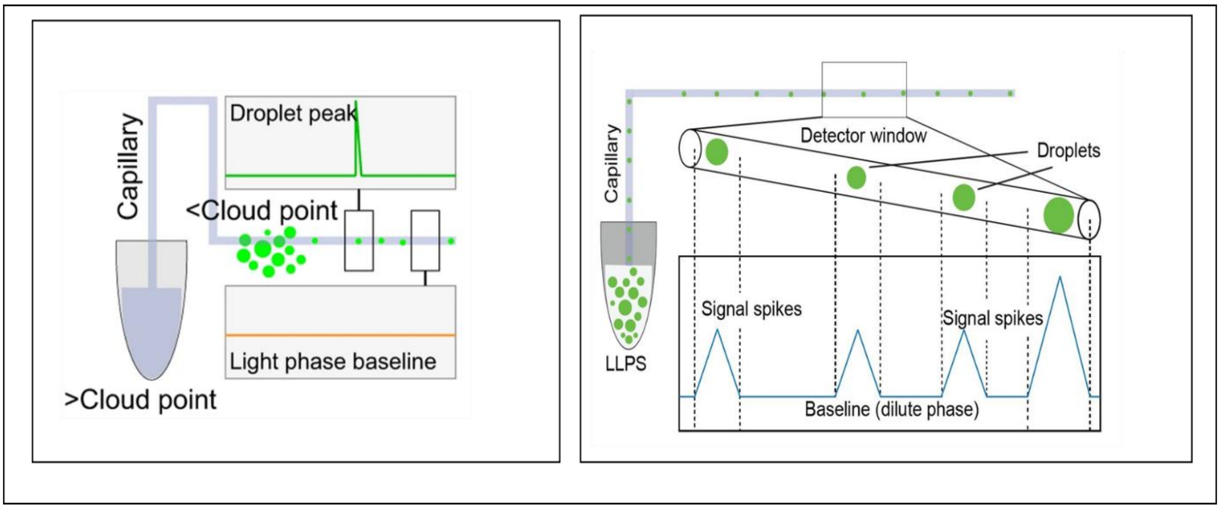

*Figure 49.* ***Schematic representation of flow-induced dispersion analysis principle:*** *After flowing through the capillary, injected sample reaches a detector where a droplet causes a spike in the signal. The baseline between spikes corresponds to the dilute phase concentration.*(Poulsen et al., 2015)

The dead time after the injection, (time taken for the solution front to reach the detector window) can be controlled by the applied pressure. This time depends on the viscosity and the pressure of the injected sample. If the sample injected undergoe LLPS, it may lead to an increase in viscosity, also results in an increased dead time for a given injection pressure. Therefore, this time should preferably be long enough that a pseudo-equilibrium for LLPS has been achieved, i.e. that the dilute phase concentration has reached its equilibrium value and can be read from the fluorescence baseline.

- <u>Experiment:</u>

FIDA measurements were made in IGBMC, Strasbourg. The FIDA experiments were conducted using standard fused silica capillaries (75 µm inner diameter, 360 µm outer diameter) with laser-induced fluorescence detection (ZETALIF Evolution, Picometrics). A 488 nm laser was used for fluorophore excitation. Initially, the capillary is rinsed to remove contaminants prior to analysis. Then the capillary is equilibrated with sample buffer (20mM Tris-HCL PH=7.5, 120mM NaCl for LLPS samples); then the sample is loaded directly into 1m capillary housed in a thermostatted chamber by automated pipetting. The entire samples measured, came from the same stock solution to which we added a certain concentration of labeled protein. Data were analyzed using FIDA software V2.

## (h) **Dynamic light scattering (DLS):**

- Introduction :

Dynamic light scattering (DLS) is based on the Brownian motion of dispersed particles. Particles move randomly in all directions, particles are constantly colliding with solvent molecules. These collisions cause a certain amount of energy to be transferred, which induces particle movement. The energy transfer is more or less constant, this have a big effect on smaller particles. As a result, smaller particles are moving more rapidly than larger particles. If the parameters, which influence the movement of the particle, are known, we can determine the hydrodynamic diameter can be measured by knowing the speed of the particles.

The relation between the speed of the particles and the particle size is given by the Stokes-Einstein equation (below). The speed of the particles is given by the translational diffusion coefficient D.

Further, the equation includes the viscosity of the dispersant and the temperature because both parameters directly influence particle movement.

DLS has a lower size limit, defined by the signal-to-noise ratio. Small particles do not scatter much light, which leads to an insufficient measurement signal.

### **The Stokes-Einstein equation:**

$$D = \frac{k_B T}{6\pi\eta R_H}$$

| | |
|---|---|
| D | Translational diffusion coefficient [$m^2/s$] – “speed of the particles” |
| KB | Boltzmann constant [$m^2kg/Ks^2$] |
| T | Temperature [K] |
| H | Viscosity [Pa.s] |

RH Hydrodynamic radius [m]

This equation is correct in the case where we assume that, the motion is purely Brownian and the particles are spherical. The value Rh represent hydrodynamic radius of a hypothetical spherical particle.

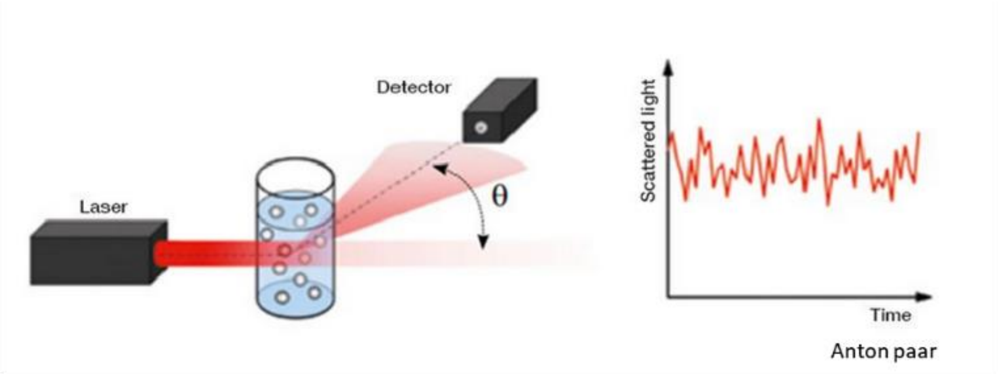

*Figure 50. Basic setup of DLS measurement system. Credit to Anton paar*

Scattered light is detected over a period to monitor particle motion. The intensity of scattered light is not constant and changes over time. Fast-moving small particles exhibit faster fluctuations than large particles (**Figure, 51**). On the other hand, the larger the particle, the greater the amplitude between the maximum and minimum scattering intensity.

This initial intensity trace is further used to generate a correlation function (**Figure, 51**). In general, the correlation function represents the time that particles are at the same location in the sample. Initially, the correlation function is linear and nearly constant, indicating that the particle is still in the same position as it was a moment ago. Later we can see the exponential decay of the correlation function. This means the particles are moving. This part of the correlation function is called the baseline. The baseline gives Information about size-dependent motion, which is contained in the decay of the correlation function. Attenuation provides an indirect measure of how long it takes a particle to change its relative position: smaller particles move faster, so they decay faster. Larger particles move more slowly, so the correlation function decays later. Changes in light intensity can provide information on the molecular diffusion and can be used to extract the diffusion coefficient, which in turn can be used to calculate the particle size.

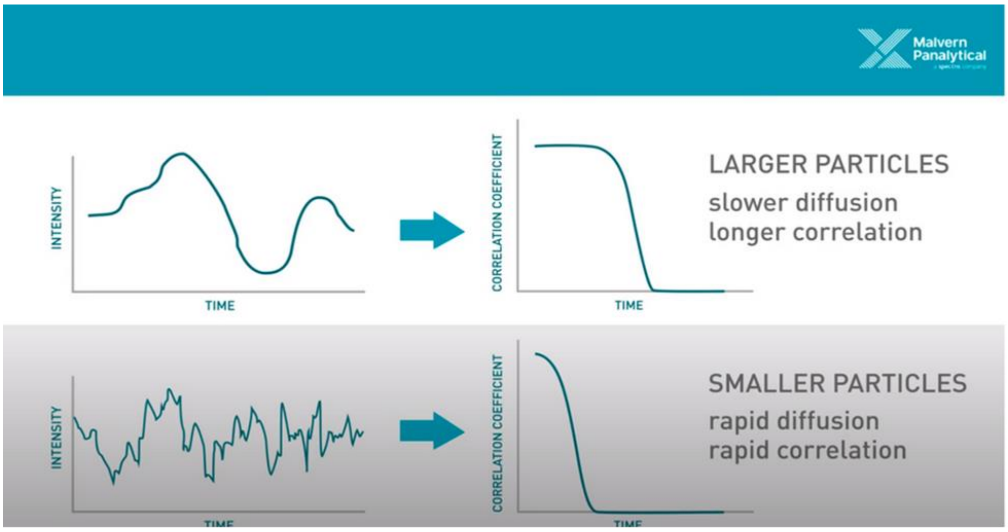

Dynamic Light Scattering (DLS)." Malvern Panalytical

*Figure 51. Correlation function generated from initial recorded intensity of a sample.*

- Experiment**:**

Measures were performed with a Zetasizer Ultra in the ISBG biophysical platform, Grenoble. In order to eliminate dust and large aggregates, our samples were filtered through a 0.2 µm cutoff membrane filter. Dynamic light scattering was then measured at a 173-degree scattering angle using a 45-µL cuvette and a laser emitting at 633 nm. Data were analyzed using the Malvern zetasizer software.

### (i) **Analytic ultra-centrifugation (AUC):**

- Introduction :

Analytical ultracentrifugation (AUC) is a method for characterizing solutions of macromolecules and quantitative analysis of macromolecular interactions ((Cole & Hansen, 1999); (HOWLETT et al., 2006)). Because AUC is based on the primary properties of mass and the fundamental laws of gravity, it has wide applicability and can be used to analyze the dissolution behavior of different molecules of various concentration, in different solvent. In contrast to many common methods, analytical ultracentrifugation samples are characterized in their native state under biologically relevant solution conditions. Since experiments are performed in free solution, there are no complications due to interactions with matrices or surfaces.

AUC is based on two different principles:

- Sedimentation velocity provides fundamental hydrodynamic information about molecular size and shape (HOWLETT et al., 2006) .
- Sedimentation equilibria provide fundamental thermodynamic information about molar masses, stoichiometry, binding constants, and solution non-idealities (Cole et al., 2008; HOWLETT et al., 2006).

## 1. Sedimentation velocity (SV):

Series of scans of the protein are taken every two or 3 minutes, protein is analyzed moving all the way through the cell. In general, characteristics of SV is the use of high rotor speed. Centrifugal force are applied on the protein and the rate of sedimentation and transport of the protein or other molecules through solution is measured. In the SV, sedimentation is considered as the dominant process, and diffusion against this gradient is minimal. Ole Lamm's 1929 description of sedimentation and diffusion of particles in a sector-shaped cell, or the Lamm equation, forms the basis for SV analysis:

$$\frac{\partial c}{\partial t} = D\left[\frac{\partial^2 c}{\partial r^2} + \frac{1}{r}\frac{\partial c}{\partial r}\right] - s\omega^2\left[r\frac{\partial c}{\partial r} + 2c\right],$$

D : Diffusion coefficient
S : sedimentation coefficient
R : radial position
C : particule concentration along the radius of the cell at any given time *t.*

SV gives informations about:

- **Sedimentation coefficient (s):** is proportional to the mass, the larger the molecule; the larger the sedimentation coefficient will be. The relationship between solvent and physical properties of sedimenting particles is defined by the Svedberg equation:

$$\frac{M(1-\bar{v}\rho)}{N_A f} = \frac{v}{\omega^2 r} \equiv s,$$

In which:

- $s$ is the sedimentation coefficient
- $v$ is the solute velocity
- $r$ is the radial distance from the axis of rotation
- $\omega$ is the angular (rotor) velocity,
- $M$ is the molecular weight
- $N_A$ is Avogadro's number
- $f$ is the frictional coefficient
- $V$ is the partial specific volume of the solute
- $\rho$ is the density of the solvent.
-

➢ **Frictional ratio (f/f0):**

This factor is inversely proportional to the sedimentation coefficient, and highly dependent on themass. It can be bescribed by stokes law:

$$\frac{f}{f_0} = \frac{M_w(1-\bar{v}\rho_0)}{N_A 6\pi\eta_0 s\left(\frac{3M_w\bar{v}}{4\pi N_A}\right)^{1/3}}$$

$$\frac{f}{f_0} = \frac{RT}{N_A 6\pi\eta_0 D\left(\frac{3M_w\bar{v}}{4\pi N_A}\right)^{1/3}}$$

$f = RT/D$ $\quad$ $f = 6\pi\eta Rs$ $\quad$ $s \propto 1/f$ $\quad$ $s \propto D$

η : is the dynamic viscosity
R: is the radius of spherical objects

➢ **Estimate MM :** calculated from the Svedberg equation.

## 2. Sedimentation equilibrium :

In this type of experiment, diffusion will oppose sedimentation, with time the force due to sedimentation and force due to diffusion will equilibrate to attend a concentration equilibrium gradient. By fitting the exponential curves obtained by the measure, we can directly have the molecular massof the sample without any effect of shape, or need to standards.

For an ideal single non-interacting species, the equilibrium radial concentration gradient, c(r), is given by :

$$c(r) = c_0 \exp\left[\frac{M_b\omega^2}{RT}\left(\frac{r^2 - r_0^2}{2}\right)\right] = c_0 \exp\left[\sigma\left(\frac{r^2 - r_0^2}{2}\right)\right]$$

$c_0$: is the concentration at an arbitrary reference distance $r_0$.
$M_b\omega^2/RT$: refer to as the reduced molecular weight, σ.

Sedimentation equilibrium experiments provide a highly accurate method of determining M and, consequently, the oligomeric state of biomolecules in solution. Deviations from the simple exponential behavior described by the above equation can result from the presence of multiple non-interacting or interacting macromolecular species, or thermodynamic non-idealities.

- Experiment:

Sedimentation velocity experiments were conducted at the the protein analysis plateform of the institute de biochimie structural (IBS) using a Beckman XL1 ultracentrifuge at a rotor speed of 42,000 rpm and at temperatures of 5°C and 20°C using Epon charcoal-filled 12 or 3 mm double-sector centerpieces. Radial absorbance scans at 280 nm were acquired every 3 or 10 minutes. The program SEDFIT (38) (available from the RASMB Web site, http://www.bbri.org/rasmb/rasmb.html) was used to analyze the sedimentation profiles by applying the solutions of the integrated Lamm equation.
Sedimentation coefficient values between 0.5 and 20 S were resolved using maximum entropy regularization with a 0.68 confidence level. Intrinsic sedimentation (S20w) corrected

to water at 20 °C were calculated from the experimental values obtained in the experimental solvent and temperature conditions according to:

$$s^{0}_{20,\mathrm{w}} = s_{\mathrm{mes}}\left(\frac{\eta_{20,\mathrm{w}}}{\eta_{T,\mathrm{b}}}\right)\left(\frac{1-\bar{v}\rho_{T,\mathrm{b}}}{1-\bar{v}\rho_{20,\mathrm{w}}}\right)$$

$$D^{0}_{20,\mathrm{w}} = D_{\mathrm{mes}}\left(\frac{\eta_{20,\mathrm{w}}}{\eta_{T,\mathrm{b}}}\right)$$

Where $\eta_{20,}$ w and ηT,b are the water viscosity at 20 °C and buffer viscosity at the experimental temperature.

# References:

Alberti, S. (2017). Phase separation in biology. *Current Biology*, *27*, R1097–R1102. https://doi.org/10.1111/pbi.1280

Albertini, A. A. V., Ruigrok, R. W. H., & Blondel, D. (2011). *Rabies Virus Transcription and Replication* (pp. 1–22). https://doi.org/10.1016/B978-0-12-387040-7.00001-9

Albertini, A. A. V., Wernimont, A. K., Muziol, T., Ravelli, R. B. G., Clapier, C. R., Schoehn, G., Weissenhorn, W., & Ruigrok, R. W. H. (2006). Crystal structure of the rabies virus nucleoprotein-RNA complex. *Science*, *313*(5785). https://doi.org/10.1126/science.1125280

Amarasinghe, G. K., Ayllón, M. A., Bào, Y., Basler, C. F., Bavari, S., Blasdell, K. R., Briese, T., Brown, P. A., Bukreyev, A., Balkema-Buschmann, A., Buchholz, U. J., Chabi-Jesus, C., Chandran, K., Chiapponi, C., Crozier, I., de Swart, R. L., Dietzgen, R. G., Dolnik, O., Drexler, J. F., … Kuhn, J. H. (2019). Taxonomy of the order Mononegavirales: update 2019. *Archives of Virology*, *164*(7), 1967–1980. https://doi.org/10.1007/s00705-019-04247-4

Baltimore, D. (1971). Expression of animal virus genomes. *Bacteriological Reviews*, *35*(3), 235–241. https://doi.org/10.1128/MMBR.35.3.235-241.1971

Banani, S. F., Lee, H. O., Hyman, A. A., & Rosen, M. K. (2017). Biomolecular condensates: organizers of cellular biochemistry. *Nature Reviews Molecular Cell Biology*, *18*(5), 285–298. https://doi.org/10.1038/nrm.2017.7

Bates, F. S. (1991). Polymer-Polymer Phase Behavior. *Science*, *251*(4996), 898–905. https://doi.org/10.1126/science.251.4996.898

Baudin, F., Bach, C., Cusack, S., & Ruigrok, R. W. H. (1994). Structure of influenza virus RNP. I. Influenza virus nucleoprotein melts secondary structure in panhandle RNA and exposes the bases to the solvent. *EMBO Journal*, *13*(13). https://doi.org/10.1002/j.1460-2075.1994.tb06614.x

Biamonti, G., & Vourc'h, C. (2010). Nuclear Stress Bodies. *Cold Spring Harbor Perspectives in Biology*, *2*(6), a000695–a000695. https://doi.org/10.1101/cshperspect.a000695

Blondel, D., Maarifi, G., Nisole, S., & Chelbi-Alix, M. (2015). Resistance to Rhabdoviridae Infection and Subversion of Antiviral Responses. *Viruses*, *7*(7), 3675–3702. https://doi.org/10.3390/v7072794

Blondel, D., Regad, T., Poisson, N., Pavie, B., Harper, F., Pandolfi, P. P., de Thé, H., & Chelbi-Alix, M. K. (2002). Rabies virus P and small P products interact directly with PML and reorganize PML nuclear bodies. *Oncogene*, *21*(52), 7957–7970. https://doi.org/10.1038/sj.onc.1205931

Boija, A., Klein, I. A., & Young, R. A. (2021). Biomolecular Condensates and Cancer. *Cancer Cell*, *39*(2), 174–192. https://doi.org/10.1016/j.ccell.2020.12.003

Brangwynne, C. P., Tompa, P., & Pappu, R. V. (2015a). Polymer physics of intracellular phase transitions. *Nature Physics*, *11*(11), 899–904. https://doi.org/10.1038/nphys3532

Brangwynne, C. P., Tompa, P., & Pappu, R. V. (2015b). Polymer physics of intracellular phase transitions. *Nature Physics*, *11*(11). https://doi.org/10.1038/nphys3532

Brown, J. C., Newcomb, W. W., & Wertz, G. W. (2010). Helical Virus Structure: The Case of the Rhabdovirus Bullet. *Viruses*, *2*(4), 995–1001. https://doi.org/10.3390/v2040995

Charlier, C. M., Wu, Y.-J., Allart, S., Malnou, C. E., Schwemmle, M., & Gonzalez-Dunia, D. (2013). Analysis of Borna Disease Virus Trafficking in Live Infected Cells by Using a Virus

Encoding a Tetracysteine-Tagged P Protein. *Journal of Virology*, *87*(22). https://doi.org/10.1128/jvi.01127-13

Chelbi-Alix, M. K., Vidy, A., Bougrini, J. El, & Blondel, D. (2006). Rabies Viral Mechanisms to Escape the IFN System: The Viral Protein P Interferes with IRF-3, Stat1, and PML Nuclear Bodies. *Journal of Interferon & Cytokine Research*, *26*(5), 271–280. https://doi.org/10.1089/jir.2006.26.271

Cole, J. L., & Hansen, J. C. (1999). Analytical ultracentrifugation as a contemporary biomolecular research tool. In *Journal of Biomolecular Techniques* (Vol. 10, Issue 4).

Cole, J. L., Lary, J. W., P. Moody, T., & Laue, T. M. (2008). Analytical Ultracentrifugation: Sedimentation Velocity and Sedimentation Equilibrium. In *Methods in Cell Biology* (Vol. 84). https://doi.org/10.1016/S0091-679X(07)84006-4

Da Vela, S., Braun, M. K., Dörr, A., Greco, A., Möller, J., Fu, Z., Zhang, F., & Schreiber, F. (2016). Kinetics of liquid–liquid phase separation in protein solutions exhibiting LCST phase behavior studied by time-resolved USAXS and VSANS. *Soft Matter*, *12*(46), 9334–9341. https://doi.org/10.1039/C6SM01837H

Davis, B. M., Rall, G. F., & Schnell, M. J. (2015a). Everything You Always Wanted to Know about Rabies Virus (But Were Afraid to Ask). In *Annual Review of Virology* (Vol. 2). https://doi.org/10.1146/annurev-virology-100114-055157

Davis, B. M., Rall, G. F., & Schnell, M. J. (2015b). Everything You Always Wanted to Know about Rabies Virus (But Were Afraid to Ask). In *Annual Review of Virology* (Vol. 2, pp. 451–471). Annual Reviews Inc. https://doi.org/10.1146/annurev-virology-100114-055157

de Castro Martin, I. F., Fournier, G., Sachse, M., Pizarro-Cerda, J., Risco, C., & Naffakh, N. (2017). Influenza virus genome reaches the plasma membrane via a modified endoplasmic reticulum and Rab11-dependent vesicles. *Nature Communications*, *8*(1), 1396. https://doi.org/10.1038/s41467-017-01557-6

de Jong Bungenberg, H. G., & Kruyt, H. R. (1929). Chemistry—Coacervation (Partial miscibility in colloid systems). *Proc. K. Ned. Akad. Wet.*, *32*.

Derdowski, A., Peters, T. R., Glover, N., Qian, R., Utley, T. J., Burnett, A., Williams, J. V., Spearman, P., & Crowe, J. E. (2008). Human metapneumovirus nucleoprotein and phosphoprotein interact and provide the minimal requirements for inclusion body formation. *Journal of General Virology*, *89*(11), 2698–2708. https://doi.org/10.1099/vir.0.2008/004051-0

Dhulipala, S., & Uversky, V. N. (2022). uvesk. *Biomolecules*, *12*(10), 1436. https://doi.org/10.3390/biom12101436

Dietzschold, B., Li, J., Faber, M., & Schnell, M. (2008). Concepts in the pathogenesis of rabies. *Future Virology*, *3*(5), 481–490. https://doi.org/10.2217/17460794.3.5.481

Dietzschold, B., Schnell, M., & Koprowski, H. (n.d.). Pathogenesis of Rabies. In *The World of Rhabdoviruses* (pp. 45–56). Springer-Verlag. https://doi.org/10.1007/3-540-27485-5_3

Dinh, P. X., Beura, L. K., Das, P. B., Panda, D., Das, A., & Pattnaik, A. K. (2013). Induction of Stress Granule-Like Structures in Vesicular Stomatitis Virus-Infected Cells. *Journal of Virology*, *87*(1), 372–383. https://doi.org/10.1128/JVI.02305-12

Du, M., & Chen, Z. J. (2018). DNA-induced liquid phase condensation of cGAS activates innate immune signaling. *Science*, *361*(6403), 704–709. https://doi.org/10.1126/science.aat1022

Dunker, A. K., Lawson, J. D., Brown, C. J., Williams, R. M., Romero, P., Oh, J. S., Oldfield, C. J., Campen, A. M., Ratliff, C. M., Hipps, K. W., Ausio, J., Nissen, M. S., Reeves, R., Kang, C., Kissinger, C. R., Bailey, R. W., Griswold, M. D., Chiu, W., Garner, E. C., & Obradovic, Z.

(2001). Intrinsically disordered protein. *Journal of Molecular Graphics & Modelling*, *19*(1), 26–59. https://doi.org/10.1016/s1093-3263(00)00138-8

Dyson, H. J., & Wright, P. E. (2005). Intrinsically unstructured proteins and their functions. *Nature Reviews Molecular Cell Biology*, *6*(3), 197–208. https://doi.org/10.1038/nrm1589

El Asmi, F., Brantis-De-carvalho, C. E., Blondel, D., & Chelbi-Alix, M. K. (2018). Rhabdoviruses, antiviral defense, and sumo pathway. In *Viruses* (Vol. 10, Issue 12). https://doi.org/10.3390/v10120686

Elbaum-Garfinkle, S., Kim, Y., Szczepaniak, K., Chen, C. C.-H., Eckmann, C. R., Myong, S., & Brangwynne, C. P. (2015). The disordered P granule protein LAF-1 drives phase separation into droplets with tunable viscosity and dynamics. *Proceedings of the National Academy of Sciences*, *112*(23), 7189–7194. https://doi.org/10.1073/pnas.1504822112

Emerson, S. U., & Yu, Y. (1975). Both NS and L proteins are required for in vitro RNA synthesis by vesicular stomatitis virus. *Journal of Virology*, *15*(6). https://doi.org/10.1128/jvi.15.6.1348-1356.1975

Emsley, P., & Cowtan, K. (2004). Coot : model-building tools for molecular graphics. *Acta Crystallographica Section D Biological Crystallography*, *60*(12), 2126–2132. https://doi.org/10.1107/S0907444904019158

Flory, P. J. (1942). Thermodynamics of High Polymer Solutions. *The Journal of Chemical Physics*, *10*(1), 51–61. https://doi.org/10.1063/1.1723621

Follett, E. A. C., Pringle, C. R., Wunner, W. H., & Skehel, J. J. (1974). Virus Replication in Enucleate Cells: Vesicular Stomatitis Virus and Influenza Virus. *Journal of Virology*, *13*(2), 394–399. https://doi.org/10.1128/jvi.13.2.394-399.1974

Fouquet, B., Nikolic, J., Larrous, F., Bourhy, H., Wirblich, C., Lagaudrière-Gesbert, C., & Blondel, D. (2015). Focal Adhesion Kinase Is Involved in Rabies Virus Infection through Its Interaction with Viral Phosphoprotein P. *Journal of Virology*, *89*(3), 1640–1651. https://doi.org/10.1128/JVI.02602-14

Gaudin, Y., Tuffereau, C., Durrer, P., Brunner, J., Flamand, A., & Ruigrok, R. (1999). Rabies virus-induced membrane fusion. *Molecular Membrane Biology*, *16*(1), 21–31. https://doi.org/10.1080/096876899294724

Ge, P., Tsao, J., Schein, S., Green, T. J., Luo, M., & Zhou, Z. H. (2010). Cryo-EM Model of the Bullet-Shaped Vesicular Stomatitis Virus. *Science*, *327*(5966), 689–693. https://doi.org/10.1126/science.1181766

Gérard, F. C. A., Bourhis, J. M., Mas, C., Branchard, A., Vu, D. D., Varhoshkova, S., Leyrat, C., & Jamin, M. (2022). Structure and Dynamics of the Unassembled Nucleoprotein of Rabies Virus in Complex with Its Phosphoprotein Chaperone Module. *Viruses*, *14*(12). https://doi.org/10.3390/v14122813

Gerard, F. C. A., Ribeiro, E. D. A., Albertini, A. A. V., Gutsche, I., Zaccai, G., Ruigrok, R. W. H., & Jamin, M. (2007). Unphosphorylated Rhabdoviridae phosphoproteins form elongated dimers in solution. *Biochemistry*, *46*(36), 10328–10338. https://doi.org/10.1021/bi7007799

Gerard, F. C. A., Ribeiro, E. de A., Leyrat, C., Ivanov, I., Blondel, D., Longhi, S., Ruigrok, R. W. H., & Jamin, M. (2009). Modular Organization of Rabies Virus Phosphoprotein. *Journal of Molecular Biology*, *388*(5), 978–996. https://doi.org/10.1016/j.jmb.2009.03.061

Greninger, A. L. (2018). The challenge of diagnostic metagenomics. *Expert Review of Molecular Diagnostics*, *18*(7), 605–615. https://doi.org/10.1080/14737159.2018.1487292

Harty, R. N., Paragas, J., Sudol, M., & Palese, P. (1999). A Proline-Rich Motif within the Matrix Protein of Vesicular Stomatitis Virus and Rabies Virus Interacts with WW Domains of Cellular Proteins: Implications for Viral Budding. *Journal of Virology*, *73*(4), 2921–2929. https://doi.org/10.1128/JVI.73.4.2921-2929.1999

HEENEY, J. L. (2006). Zoonotic viral diseases and the frontier of early diagnosis, control and prevention. *Journal of Internal Medicine*, *260*(5), 399–408. https://doi.org/10.1111/j.1365-2796.2006.01711.x

Hidaka, Y., Lim, C.-K., Takayama-Ito, M., Park, C.-H., Kimitsuki, K., Shiwa, N., Inoue, K., & Itou, T. (2018). Segmentation of the rabies virus genome. *Virus Research*, *252*, 68–75. https://doi.org/10.1016/j.virusres.2018.05.017

Hirel, P. H., Schmitter, J. M., Dessen, P., Fayat, G., & Blanquet, S. (1989). Extent of N-terminal methionine excision from Escherichia coli proteins is governed by the side-chain length of the penultimate amino acid. *Proceedings of the National Academy of Sciences of the United States of America*, *86*(21). https://doi.org/10.1073/pnas.86.21.8247

Horwitz, J. A., Jenni, S., Harrison, S. C., & Whelan, S. P. J. (2020). Structure of a rabies virus polymerase complex from electron cryo-microscopy. *Proceedings of the National Academy of Sciences of the United States of America*, *117*(4). https://doi.org/10.1073/pnas.1918809117

HOWLETT, G., MINTON, A., & RIVAS, G. (2006). Analytical ultracentrifugation for the study of protein association and assembly. *Current Opinion in Chemical Biology*, *10*(5), 430–436. https://doi.org/10.1016/j.cbpa.2006.08.017

Huggins, M. L. (1942). Some Properties of Solutions of Long-chain Compounds. *The Journal of Physical Chemistry*, *46*(1), 151–158. https://doi.org/10.1021/j150415a018

Hyman, A. A., Weber, C. A., & Jülicher, F. (2014). Liquid-liquid phase separation in biology. In *Annual review of cell and developmental biology* (Vol. 30, pp. 39–58). https://doi.org/10.1146/annurev-cellbio-100913-013325

Inoue, T., & Tsai, B. (2013). How Viruses Use the Endoplasmic Reticulum for Entry, Replication, and Assembly. *Cold Spring Harbor Perspectives in Biology*, *5*(1), a013250–a013250. https://doi.org/10.1101/cshperspect.a013250

Irie, T., Licata, J. M., Jayakar, H. R., Whitt, M. A., Bell, P., & Harty, R. N. (2004). Functional Analysis of Late-Budding Domain Activity Associated with the PSAP Motif within the Vesicular Stomatitis Virus M Protein. *Journal of Virology*, *78*(14), 7823–7827. https://doi.org/10.1128/JVI.78.14.7823-7827.2004

Iseni, F., Barge, A., Baudin, F., Blondel, D., & Ruigrok, R. W. H. (1998). Characterization of rabies virus nucleocapsids and recombinant nucleocapsid-like structures. *Journal of General Virology*, *79*(12). https://doi.org/10.1099/0022-1317-79-12-2909

Ivanov, I., Crépin, T., Jamin, M., & Ruigrok, R. W. H. (2010). Structure of the Dimerization Domain of the Rabies Virus Phosphoprotein. *Journal of Virology*, *84*(7). https://doi.org/10.1128/jvi.02557-09

Jespersen, N. E., Leyrat, C., Gérard, F. C., Bourhis, J. M., Blondel, D., Jamin, M., & Barbar, E. (2019). The LC8-RavP ensemble Structure Evinces A Role for LC8 in Regulating Lyssavirus Polymerase Functionality. *Journal of Molecular Biology*, *431*(24). https://doi.org/10.1016/j.jmb.2019.10.011

Kammouni, W., Wood, H., Saleh, A., Appolinario, C. M., Fernyhough, P., & Jackson, A. C. (2015). Rabies virus phosphoprotein interacts with mitochondrial Complex I and induces mitochondrial dysfunction and oxidative stress. *Journal of NeuroVirology*, *21*(4), 370–382. https://doi.org/10.1007/s13365-015-0320-8

Kim, S., Huang, J., Lee, Y., Dutta, S., Yoo, H. Y., Jung, Y. M., Jho, Y., Zeng, H., & Hwang, D. S. (2016). Complexation and coacervation of like-charged polyelectrolytes inspired by mussels. *Proceedings of the National Academy of Sciences*, *113*(7). https://doi.org/10.1073/pnas.1521521113

Koonin, E. V., Krupovic, M., & Agol, V. I. (2021). The Baltimore Classification of Viruses 50 Years Later: How Does It Stand in the Light of Virus Evolution? *Microbiology and Molecular Biology Reviews*, *85*(3). https://doi.org/10.1128/MMBR.00053-21

Koonin, E. V, Senkevich, T. G., & Dolja, V. V. (2006). The ancient Virus World and evolution of cells. *Biology Direct*, *1*(1), 29. https://doi.org/10.1186/1745-6150-1-29

Kuhn, J. H., Adkins, S., Alioto, D., Alkhovsky, S. V., Amarasinghe, G. K., Anthony, S. J., Avšič-Županc, T., Ayllón, M. A., Bahl, J., Balkema-Buschmann, A., Ballinger, M. J., Bartonička, T., Basler, C., Bavari, S., Beer, M., Bente, D. A., Bergeron, É., Bird, B. H., Blair, C., … Zhou, X. (2020). 2020 taxonomic update for phylum Negarnaviricota (Riboviria: Orthornavirae), including the large orders Bunyavirales and Mononegavirales. *Archives of Virology*, *165*(12). https://doi.org/10.1007/s00705-020-04731-2

Lahaye, X., Vidy, A., Pomier, C., Obiang, L., Harper, F., Gaudin, Y., & Blondel, D. (2009). Functional Characterization of Negri Bodies (NBs) in Rabies Virus-Infected Cells: Evidence that NBs Are Sites of Viral Transcription and Replication. *Journal of Virology*, *83*(16), 7948–7958. https://doi.org/10.1128/jvi.00554-09

Lamarsh, J. R., & Melkonian, E. (1977). Introduction to Nuclear Engineering. *Physics Today*, *30*(6). https://doi.org/10.1063/1.3037597

Leabu, M. (2006). Membrane fusion in cells: molecular machinery and mechanisms. *Journal of Cellular and Molecular Medicine*, *10*(2), 423–427. https://doi.org/10.1111/j.1582-4934.2006.tb00409.x

Leyrat, C., C.A. Gerard, F., de Almeida Ribeiro Jr., E., Ivanov, I., W.H. Ruigrok, R., & Jamin, M. (2010). Structural Disorder in Proteins of the Rhabdoviridae Replication Complex. *Protein & Peptide Letters*, *17*(8), 979–987. https://doi.org/10.2174/092986610791498939

Leyrat, C., Ribeiro, E. A., Gérard, F. C. A., Ivanov, I., Ruigrok, R. W. H., & Jamin, M. (2011). Structure, interactions with host cell and functions of rhabdovirus phosphoprotein. In *Future Virology* (Vol. 6, Issue 4, pp. 465–481). https://doi.org/10.2217/fvl.11.10

Leyrat, C., Schneider, R., Ribeiro, E. A., Yabukarski, F., Yao, M., Gérard, F. C. A., Jensen, M. R., Ruigrok, R. W. H., Blackledge, M., & Jamin, M. (2012). Ensemble Structure of the Modular and Flexible Full-Length Vesicular Stomatitis Virus Phosphoprotein. *Journal of Molecular Biology*, *423*(2), 182–197. https://doi.org/10.1016/j.jmb.2012.07.003

Li, Y., Dong, W., Shi, Y., Deng, F., Chen, X., Wan, C., Zhou, M., Zhao, L., Fu, Z. F., & Peng, G. (2016). Rabies virus phosphoprotein interacts with ribosomal protein L9 and affects rabies virus replication. *Virology*, *488*, 216–224. https://doi.org/10.1016/j.virol.2015.11.018

Liang, B. (2020). Structures of the Mononegavirales Polymerases. *Journal of Virology*, *94*(22). https://doi.org/10.1128/JVI.00175-20

Liu, J., Wang, H., Gu, J., Deng, T., Yuan, Z., Hu, B., Xu, Y., Yan, Y., Zan, J., Liao, M., DiCaprio, E., Li, J., Su, S., & Zhou, J. (2017). BECN1-dependent CASP2 incomplete autophagy induction by binding to rabies virus phosphoprotein. *Autophagy*, *13*(4), 739–753. https://doi.org/10.1080/15548627.2017.1280220

Majeed, S. A., Sekhosana, K. E., & Tuhl, A. (2020). Progress on phthalocyanine-conjugated Ag and Au nanoparticles: Synthesis, characterization, and photo-physicochemical properties. *Arabian Journal of Chemistry*, *13*(12), 8848–8887.

https://doi.org/10.1016/j.arabjc.2020.10.014

Mavrakis, M., McCarthy, A. A., Roche, S., Blondel, D., & Ruigrok, R. W. H. (2004). Structure and function of the C-terminal domain of the polymerase cofactor of rabies virus. *Journal of Molecular Biology*, *343*(4). https://doi.org/10.1016/j.jmb.2004.08.071

Milkovic, N. M., & Mittag, T. (2020). Determination of protein phase diagrams by centrifugation. In *Methods in Molecular Biology* (Vol. 2141). https://doi.org/10.1007/978-1-0716-0524-0_35

Najafi, S., Lin, Y., Longhini, A. P., Zhang, X., Delaney, K. T., Kosik, K. S., Fredrickson, G. H., Shea, J., & Han, S. (2021). Liquid–liquid phase separation of Tau by self and complex coacervation. *Protein Science*, *30*(7), 1393–1407. https://doi.org/10.1002/pro.4101

Neil, S. J. D., Eastman, S. W., Jouvenet, N., & Bieniasz, P. D. (2006). HIV-1 Vpu Promotes Release and Prevents Endocytosis of Nascent Retrovirus Particles from the Plasma Membrane. *PLoS Pathogens*, *2*(5), e39. https://doi.org/10.1371/journal.ppat.0020039

Nevers, Q., Scrima, N., Glon, D., Le Bars, R., Decombe, A., Garnier, N., Ouldali, M., Lagaudrière-Gesbert, C., Blondel, D., Albertini, A., & Gaudin, Y. (2022). Properties of rabies virus phosphoprotein and nucleoprotein biocondensates formed in vitro and in cellulo. *PLOS Pathogens*, *18*(12), e1011022. https://doi.org/10.1371/journal.ppat.1011022

Nikolic, J., Lagaudrière-Gesbert, C., Scrima, N., Blondel, D., & Gaudin, Y. (2019). Structure and Function of Negri Bodies. In *Advances in Experimental Medicine and Biology* (Vol. 1140, pp. 111–127). Springer New York LLC. https://doi.org/10.1007/978-3-030-14741-9_6

Nikolic, J., Le Bars, R., Lama, Z., Scrima, N., Lagaudrière-Gesbert, C., Gaudin, Y., & Blondel, D. (2017a). Negri bodies are viral factories with properties of liquid organelles. *Nature Communications*, *8*(1), 1–13. https://doi.org/10.1038/s41467-017-00102-9

Nikolic, J., Le Bars, R., Lama, Z., Scrima, N., Lagaudrière-Gesbert, C., Gaudin, Y., & Blondel, D. (2017b). Negri bodies are viral factories with properties of liquid organelles. *Nature Communications*, *8*(1). https://doi.org/10.1038/s41467-017-00102-9

Nott, T. J., Petsalaki, E., Farber, P., Jervis, D., Fussner, E., Plochowietz, A., Craggs, T. D., Bazett-Jones, D. P., Pawson, T., Forman-Kay, J. D., & Baldwin, A. J. (2015). Phase transition of a disordered nuage protein generates environmentally responsive membraneless organelles. *Molecular Cell*, *57*(5), 936–947. https://doi.org/10.1016/j.molcel.2015.01.013

Nozawa, R., Yamamoto, T., Takahashi, M., Tachiwana, H., Maruyama, R., Hirota, T., & Saitoh, N. (2020). Nuclear microenvironment in cancer: Control through liquid-liquid phase separation. *Cancer Science*, *111*(9), 3155–3163. https://doi.org/10.1111/cas.14551

Ohki, S. (Ed.). (1991). *Cell and Model Membrane Interactions*. Springer US. https://doi.org/10.1007/978-1-4615-3854-7

Oksayan, S., Wiltzer, L., Rowe, C. L., Blondel, D., Jans, D. A., & Moseley, G. W. (2012). A Novel Nuclear Trafficking Module Regulates the Nucleocytoplasmic Localization of the Rabies Virus Interferon Antagonist, P Protein. *Journal of Biological Chemistry*, *287*(33), 28112–28121. https://doi.org/10.1074/jbc.M112.374694

Pearce, J. (2002). Louis Pasteur and Rabies: a brief note. *Journal of Neurology, Neurosurgery & Psychiatry*, *73*(1), 82–82. https://doi.org/10.1136/jnnp.73.1.82

Pellett, P. E., Mitra, S., & Holland, T. C. (2014). *Basics of virology* (pp. 45–66). https://doi.org/10.1016/B978-0-444-53488-0.00002-X

Poch, O., Sauvaget, I., Delarue, M., & Tordo, N. (1989). Identification of four conserved motifs among the RNA-dependent polymerase encoding elements. *EMBO Journal*, *8*(12). https://doi.org/10.1002/j.1460-2075.1989.tb08565.x

Poulsen, N. N., Andersen, N. Z., Østergaard, J., Zhuang, G., Petersen, N. J., & Jensen, H. (2015). Flow induced dispersion analysis rapidly quantifies proteins in human plasma samples. *The Analyst*, *140*(13), 4365–4369. https://doi.org/10.1039/C5AN00697J

Prabhu, V. M., Ali, S., Bleuel, M., Mao, Y., & Ma, Y. (2021). *Ultra-small angle neutron scattering to study droplet formation in polyelectrolyte complex coacervates* (pp. 261–276). https://doi.org/10.1016/bs.mie.2020.07.001

Pringle, C. R. (1997). The order Mononegavirales--current status. *Archives of Virology*, *142*(11).

Putnam, C. D., Hammel, M., Hura, G. L., & Tainer, J. A. (2007). X-ray solution scattering (SAXS) combined with crystallography and computation: defining accurate macromolecular structures, conformations and assemblies in solution. *Quarterly Reviews of Biophysics*, *40*(3), 191–285. https://doi.org/10.1017/S0033583507004635

Rabouille, C. (2019). Membraneless organelles in cell biology. *Traffic*, *20*(12), 885–886. https://doi.org/10.1111/tra.12686

Ranganathan, S., & Shakhnovich, E. (2019). Liquid-liquid microphase separation leads to formation of membraneless organelles. *BioRxiv*, 2019.12.18.881565. https://doi.org/10.1101/2019.12.18.881565

Redondo-Morata, L., Losada-Pérez, P., & Giannotti, M. I. (2020). *Lipid bilayers: Phase behavior and nanomechanics* (pp. 1–55). https://doi.org/10.1016/bs.ctm.2020.08.005

Ribeiro, E. A., Favier, A., Gerard, F. C. A., Leyrat, C., Brutscher, B., Blondel, D., Ruigrok, R. W. H., Blackledge, M., & Jamin, M. (2008). Solution Structure of the C-Terminal Nucleoprotein–RNA Binding Domain of the Vesicular Stomatitis Virus Phosphoprotein. *Journal of Molecular Biology*, *382*(2), 525–538. https://doi.org/10.1016/j.jmb.2008.07.028

Ribeiro, E. de A., Leyrat, C., Gérard, F. C. A., Albertini, A. A. V., Falk, C., Ruigrok, R. W. H., & Jamin, M. (2009). Binding of Rabies Virus Polymerase Cofactor to Recombinant Circular Nucleoprotein–RNA Complexes. *Journal of Molecular Biology*, *394*(3), 558–575. https://doi.org/10.1016/j.jmb.2009.09.042

Riggs, C. L., Kedersha, N., Ivanov, P., & Anderson, P. (2020). Mammalian stress granules and P bodies at a glance. *Journal of Cell Science*, *133*(16). https://doi.org/10.1242/jcs.242487

Rincheval, V., Lelek, M., Gault, E., Bouillier, C., Sitterlin, D., Blouquit-Laye, S., Galloux, M., Zimmer, C., Eleouet, J.-F., & Rameix-Welti, M.-A. (2017). Functional organization of cytoplasmic inclusion bodies in cells infected by respiratory syncytial virus. *Nature Communications*, *8*(1), 563. https://doi.org/10.1038/s41467-017-00655-9

Robert J. Silbey, R. A. A. M. G. B. (2004). *Physical Chemistry, 4th Edition* (martin batey).

Roossinck, M. J., & Bazán, E. R. (2017). Symbiosis: Viruses as Intimate Partners. *Annual Review of Virology*, *4*(1), 123–139. https://doi.org/10.1146/annurev-virology-110615-042323

Ruff, K. M., Roberts, S., Chilkoti, A., & Pappu, R. V. (2018). Advances in Understanding Stimulus-Responsive Phase Behavior of Intrinsically Disordered Protein Polymers. *Journal of Molecular Biology*, *430*(23), 4619–4635. https://doi.org/10.1016/j.jmb.2018.06.031

Ruigrok, R. W. H., Crépin, T., & Kolakofsky, D. (2011). Nucleoproteins and nucleocapsids of negative-strand RNA viruses. *Current Opinion in Microbiology*, *14*(4). https://doi.org/10.1016/j.mib.2011.07.011

Ryan, V. H., & Fawzi, N. L. (2019). Physiological, Pathological, and Targetable Membraneless Organelles in Neurons. *Trends in Neurosciences*, *42*(10), 693–708. https://doi.org/10.1016/j.tins.2019.08.005

Sitnikova, N. L., Sprik, R., Wegdam, G., & Eiser, E. (2005). Spontaneously Formed trans - Anethol/Water/Alcohol Emulsions: Mechanism of Formation and Stability. *Langmuir*, *21*(16), 7083–7089. https://doi.org/10.1021/la046816l

Solon, J., Gareil, O., Bassereau, P., & Gaudin, Y. (2005). Membrane deformations induced by the matrix protein of vesicular stomatitis virus in a minimal system. *Journal of General Virology*, *86*(12), 3357–3363. https://doi.org/10.1099/vir.0.81129-0

Somjee, R., Mitrea, D. M., & Kriwacki, R. W. (2020). Exploring relationships between the density of charged tracts within disordered regions and phase separation. *Pacific Symposium on Biocomputing*, *25*(2020). https://doi.org/10.1142/9789811215636_0019

Stender, E. G. P., Ray, S., Norrild, R. K., Larsen, J. A., Petersen, D., Farzadfard, A., Galvagnion, C., Jensen, H., & Buell, A. K. (2021). Capillary flow experiments for thermodynamic and kinetic characterization of protein liquid-liquid phase separation. *Nature Communications*, *12*(1). https://doi.org/10.1038/s41467-021-27433-y

te Velthuis, A. J. W., Grimes, J. M., & Fodor, E. (2021). Structural insights into RNA polymerases of negative-sense RNA viruses. *Nature Reviews Microbiology*, *19*(5), 303–318. https://doi.org/10.1038/s41579-020-00501-8

Thaker, S. K., Ch'ng, J., & Christofk, H. R. (2019). Viral hijacking of cellular metabolism. *BMC Biology*, *17*(1), 59. https://doi.org/10.1186/s12915-019-0678-9

Uversky, V. N. (1993). Use of fast protein size-exclusion liquid chromatography to study the unfolding of proteins which denature through the molten globule. *Biochemistry*, *32*(48), 13288–13298. https://doi.org/10.1021/bi00211a042

Uversky, V. N., Kuznetsova, I. M., Turoverov, K. K., & Zaslavsky, B. (2015). Intrinsically disordered proteins as crucial constituents of cellular aqueous two phase systems and coacervates. *FEBS Letters*, *589*(1), 15–22. https://doi.org/10.1016/j.febslet.2014.11.028

Vidy, A., Chelbi-Alix, M., & Blondel, D. (2005). Rabies Virus P Protein Interacts with STAT1 and Inhibits Interferon Signal Transduction Pathways. *Journal of Virology*, *79*(22), 14411–14420. https://doi.org/10.1128/JVI.79.22.14411-14420.2005

Vitale, S. A., & Katz, J. L. (2003). Liquid Droplet Dispersions Formed by Homogeneous Liquid−Liquid Nucleation: "The Ouzo Effect." *Langmuir*, *19*(10), 4105–4110. https://doi.org/10.1021/la026842o

WALL, F. T. (1954). Principles of Polymer Chemistry. Paul J. Flory. Cornell Univ. Press, Ithaca, New York, 1953. 688 pp. Illus. $8.50. *Science*, *119*(3095). https://doi.org/10.1126/science.119.3095.555-a

Wang, J., Choi, J.-M., Holehouse, A. S., Lee, H. O., Zhang, X., Jahnel, M., Maharana, S., Lemaitre, R., Pozniakovsky, A., Drechsel, D., Poser, I., Pappu, R. V., Alberti, S., & Hyman, A. A. (2018). A Molecular Grammar Governing the Driving Forces for Phase Separation of Prion-like RNA Binding Proteins. *Cell*, *174*(3), 688-699.e16. https://doi.org/10.1016/j.cell.2018.06.006

Weber, D. J., Juliano, J. J., & Rutala, W. A. (2015). Systemic infection from animals. In *Clinical Infectious Disease* (pp. 790–796). Cambridge University Press. https://doi.org/10.1017/CBO9781139855952.135

Weinherg, A. M. (1959). The Physical Theory of Neutron Chain Reactors. *Physics Today*, *12*(3). https://doi.org/10.1063/1.3060719

Weisskopf, V. (1937). Statistics and Nuclear Reactions. *Physical Review*, *52*(4), 295–303. https://doi.org/10.1103/PhysRev.52.295

Wichgers Schreur, P. J., & Kortekaas, J. (2016). Single-Molecule FISH Reveals Non-selective Packaging of Rift Valley Fever Virus Genome Segments. *PLOS Pathogens*, *12*(8), e1005800. https://doi.org/10.1371/journal.ppat.1005800

Xu, Y., Liu, F., Liu, J., Wang, D., Yan, Y., Ji, S., Zan, J., & Zhou, J. (2016). The co-chaperone Cdc37 regulates the rabies virus phosphoprotein stability by targeting to Hsp90AA1 machinery. *Scientific Reports*, *6*(1), 27123. https://doi.org/10.1038/srep27123

Yabukarski, F., Leyrat, C., Martinez, N., Communie, G., Ivanov, I., Ribeiro, E. A., Buisson, M., Gerard, F. C., Bourhis, J.-M., Jensen, M. R., Bernadó, P., Blackledge, M., & Jamin, M. (2016). Ensemble Structure of the Highly Flexible Complex Formed between Vesicular Stomatitis Virus Unassembled Nucleoprotein and its Phosphoprotein Chaperone. *Journal of Molecular Biology*, *428*(13), 2671–2694. https://doi.org/10.1016/j.jmb.2016.04.010

Zaccai, N. R., Sandlin, C. W., Hoopes, J. T., Curtis, J. E., Fleming, P. J., Fleming, K. G., & Krueger, S. (2016). *Deuterium Labeling Together with Contrast Variation Small-Angle Neutron Scattering Suggests How Skp Captures and Releases Unfolded Outer Membrane Proteins* (pp. 159–210). https://doi.org/10.1016/bs.mie.2015.06.041

Zhou, Y., Su, J. M., Samuel, C. E., & Ma, D. (2019). Measles Virus Forms Inclusion Bodies with Properties of Liquid Organelles. *Journal of Virology*, *93*(21). https://doi.org/10.1128/JVI.00948-19